Self-excited oscillations of flexible-channel flow with fixed upstream flux

Feng Xu, MEng.

Thesis submitted to the University of Nottingham

for the degree of Doctor of Philosophy

April 2014

Abstract

Self-excited oscillations in a collapsible-tube flow driven by fixed upstream flux have been observed by numerical and laboratory experiments. In this thesis we attempt to understand the mechanism of onset of these oscillations by focusing on a reduced physical model. We consider flow in a finite-length planar channel, where a segment of one wall is replaced by a membrane under longitudinal tension. The upstream flux and downstream pressure are prescribed and an external linear pressure distribution is applied to the membrane such that the system admits uniform Poiseuille flow as a steady solution. We describe the system using a one-dimensional model that accounts for viscous and fluid inertial effects. We perform linear stability analysis and weakly nonlinear analysis on the one-dimensional model, the resulting predictions are tested against two-dimensional Navier–Stokes numerical simulation.When the membrane has similar length to the rigid segment of channel downstream of the membrane, we find that in a narrow parameter regime we consider "mode-2" oscillations (i.e. membrane displacements with two extrema) are largely independent of the downstream segment but are driven by divergent instabilities of two non-uniform steady configurations of the membrane. When the downstream segment is much longer than the membrane, our analysis reveals how instability is promoted by a 1:1 resonant interaction between two modes, with the resulting oscillations described by a fourth-order amplitude equation. This predicts the existence of saturated sawtooth oscillations, which we reproduce in full Navier–Stokes simulations of the same system. In this case, our analysis shows some agreements with experimental observations, namely that increasing the length of the downstream tube reduces the frequency of oscillations but has little effect on the conditions for onset. We also use linear stability analysis to show that steady highly-collapsed solutions, constructed by utilizing matched asymptotic expansions, are very unstable, which allows the possibility that they are a precursor to slamming motion whereby the membrane becomes transiently constricted very close to the opposite rigid wall before rapidly recovering.

Acknowledgement

I would like to express my special appreciation and thanks to my supervisors Prof. Oliver Jensen and Prof. John Billingham for their encouragement and guidance during my PhD study. I would also like to thank Prof. Matthias Heil for kindly giving advices on using `oomph-lib`. Brilliant comments and suggestions about the thesis from Prof. Timothy Pedley and Dr. Jonathan Wattis are very appreciated.

I would also like to thank School of Mathematical Sciences for funding. The work described in Chapter 2 and 3 has been published as Xu, Billingham & Jensen (2013) and Xu, Billingham & Jensen (2014), respectively. One article is currently in preparation, describing the work of Chapter 4 (joint with Oliver Jensen).

I would also like to thank all of my friends who supported me and encouraged me to strive towards my goal.

A special thanks to my family. Words cannot express how grateful I am to my great grandmother, mother, father and brother for all of the sacrifices that you've made on my behalf.

At the end I would like express appreciation to my beloved wife Wenjuan who spent sleepless nights with and was always my support in the moments when there was no one to answer my queries.

Contents

Chapter 1

Introduction

In the human body, there are a lot of highly elastic vessels, such as arteries, veins and pulmonary airways. These vessels usually play an important role in conveying fluids, such as blood and air, which support human life. When fluid flows in the vessels, tractions (pressure and viscous stress) deform them. The deformation of vessels in turn affects the internal flow field. Thus, we arrive at the problem of fluid-structure interaction. The interaction is related to many physiological phenomena, such as Korotkoff sounds generated during blood-pressure measurement, the action of cardiac and venous valves, and wheezing during forced expiration. The study of flow in elastic tubes is not only of significant interest in biomechanical and biomedical applications, but is also an interesting fluid-mechanical problem in its own right.

In the past several decades, the study of collapsible-tube flows has been exceedingly fruitful. Numerous studies, covering analytical methods, numerical simulations and experiments, have been presented; a number of review articles are available (Pedley, 1977; Shapiro, 1977; Kamm & Pedley, 1989; Grotberg, 1994; Pedley & Luo, 1998; Grotberg, 2001; Bertram, 2003; Heil & Jensen, 2003; Grotberg & Jensen, 2004; Bertram, 2008; Grotberg, 2011; Heil & Hazel, 2011).

1.1 Biological background

The human body is permeated by tubes transporting fluids of many kinds: blood vessels, lymphatics, airways, ureters, a urethra, and so on (Bertram, 2004). Some studies for blood vessels were reviewed in Pedley (1980) and Ku (1997). The propagation of the pulse wave through the arterial system is a well-known and well-understood exam-

ple of a physiological flow. The analysis of pulse waves is facilitated by the fact that under normal conditions the arteries are subject to a positive transmural (internal minus external) pressure. In this configuration the vessels are relatively stiff, and the variation of internal fluid pressure causes only small deformations. There are, however, many examples of fluid-conveying vessels that are subject to negative transmural pressure, which induces the vessels to buckle and collapse non-axisymmerically. Buckled vessels are very flexible and even small changes in fluid pressure can induce large changes of their cross-sectional area. This leads to a strong interaction of fluid and solid mechanics, which gives rise to many intriguing phenomena, such as the propensity to develop flow limitation and large-amplitude self-excited oscillations.

Flow limitation is the Bernoulli effect manifesting itself in collapsible-tube flow. When the tube is forced to collapse by the transmural pressure, the reduction of its cross-sectional area increases the local fluid velocity. The Bernoulli effect then reduces the internal fluid pressure, leading to a further increase in tube contraction. Flow limitation can cause an increasingly strong collapse of the lung airways and possibly so-called negative effort dependence, whereby an increase in expiratory effort (at a given lung volume) beyond a certain level can lead to a reduction in expiratory flow rate. There are two other mechanisms accounting for flow limitation in the literature. One is analogous to the limitation of compressible fluids at the speed of sound in rigid-walled pipes. The flow limits when the flow velocity equals to the speed of propagation of pressure pulse waves at some point, the choke point, within the elastic tube. In this case, any lowering of downstream pressure below that required to achieve a flow velocity equal to the speed of wave propagation has no effect on the maximum flow rate, or on the distribution of pressure upstream of the choke point, since the downstream pressure disturbance produced by lowering the downstream pressure cannot propagate upstream past the choke point. The wave-speed explanation of flow limitation has been tested by experiments (Elliott & Dawson, 1977; Kamm & Shapiro, 1979). Another mechanism is responsible for flow limitation in a predominantly viscous flow in a long elastic tube which is highly collapsed over a narrow region under high external pressure (Jensen, 1998).

In the following, three physiological phenomena relating to collapsible tubes, wheezing, snoring and phonation, extensively investigated in the fluid mechanics research community, will be discussed.

1.1.1 Wheezing

Wheezes are continuous audible lung sounds, which are superimposed on the normal breath sounds. The word "continuous" means that the duration of a wheeze is longer than 250 ms. They are clinically defined as more or less musical sounds and can be characterized by their location, intensity, pitch, duration in the respiratory cycle, and relationship to the phase of respiration (Meslier *et al.*, 1995). Forced exhalation is accompanied by wheezing in even the healthy at low lung volumes (Forgacs, 1967). Wheezing is also associated with some obstructive respiratory diseases. Forgacs *et al.* (1971) pointed out that inspiratory wheezes heard with the unaided ear close to the patient's mouth are an important clinical sign. Noisy inspiration is common in chronic bronchitis and asthma, and the degree of narrowing of the central bronchi can be inferred from the loudness of that noise; silent inspiration in the presence of severe expiratory obstruction is a sign of primary emphysema (Forgacs *et al.*, 1971). Recently, medical groups proposed to use wheezes to estimate the degree of airway obstruction and to be a diagnostic criterion of obstructive airway disease partially replacing spirometry (the measurement of the volume of air that a person can move into and out of the lungs, using a spirometer)(e.g. Gavriely & Cugell, 1995; Gavriely, 1996; Pasterkamp *et al.*, 1997; Leuppi *et al.*, 2006). They suggested that the degree of airway constriction can be estimated by analysing changes in spectral curves of wheezes.

To better understand the physics of wheezing, Grotberg & Gavriely (1989) and Gavriely *et al.* (1989) modelled airways as collapsible tubes, investigating oscillations arising in collapsible tubes experimentally and theoretically. Broadly speaking, two forms of oscillations in collapsible tubes, milking and flutter, are common in experimental studies. In the milking a collapse point is created and moves upstream when it opens; in the flutter the point of collapse does not move upstream. Gavriely *et al.* (1989) compared their experimental results with predictions from the fluid-dynamic flutter theory and the vortex-induced wall vibrations mechanism, and concluded that viscous flutter in flow-limited collapsible tubes is the more probable mechanism for the generation of oscillations in the collapsible tube model and is a possible mechanism for the generation of respiratory wheezes. Doherty *et al.* (1998) even reported a clinical example to show evidence in support of the dynamic flutter theory of wheeze production. They performed spectral analysis for an unusual low pitched sound from a case of relapsing polychondritis (an uncommon, chronic disorder that is characterized by recurrent episodes of inflammation of the cartilage of various tissues of the body) pre-

senting as tracheomalacia (a condition in which degeneration of trachea tissue occurs), and found that it has the characteristics of sounds produced by flutter in flow-limited collapsible tubes. The generation of a wheeze has links to wall vibration of airways and to turbulent flow in airways, both of which are induced by stenosis (Sera *et al.*, 2003). Before wheezes can be used as a clinical diagnostic index, however, flow-field patterns around stenosis must be clarified and dependence of possible mechanisms of wheeze generation on stenosis models, must be determined. In previous studies, the geometry of the stenosis models were idealised, namely, either cylindrical and symmetrical or asymmetrical with uniform distensiblility. More recently, Sera *et al.* (2003) experimentally examined a more realistic tracheostenosis model by including spatial variation of wall distensibility. Using this model, they explored the mechamism of wheeze production by focusing on the turbulence intensity. They found the turbulence intensity in expiratory flow is about twice that in inspiratory flow, and larger vortices existed in post-stenosis in expiratory flow, and concluded that this might contribute to wheeze generation.

1.1.2 Snoring

Snores are common breath sounds produced in adults during sleep. They are less commonly encountered in children, except when upper airway narrowing is present. The clinical significance of snores is not completely clear. In the majority of snorers, the soft palate (see figure 1.1) is the main vibrating object. With the mouth closed, nasal inhalation causes the soft palate briefly to obstruct the airway in the naso-pharyngeal space. With the mouth open and inflow occuring over both the upper and lower surfaces of the soft palate (from the nose and mouth, respectively), the soft palate obstructs both airways in turn as it moves between the tongue and the posterior pharyngeal wall. In addition to palatal snoring, snoring may result from collapse of the pharyngeal airway itself.

To understand the mechanism of snoring, Gavriely & Jensen (1993) established a simple theoretical model of the upper airway, consisting of a movable wall in a channel segment that connects to the airway opening via a conduit with a resistance. They suggested that snoring may be modelled as a series of dynamic closure events of the upper airways. Their theoretical prediction of the time course of wall motion during collapse compared well with the rate of appearance of repetitive sound structures during snoring. Huang *et al.* (1995) devised experimental models of palatal and pharyngeal

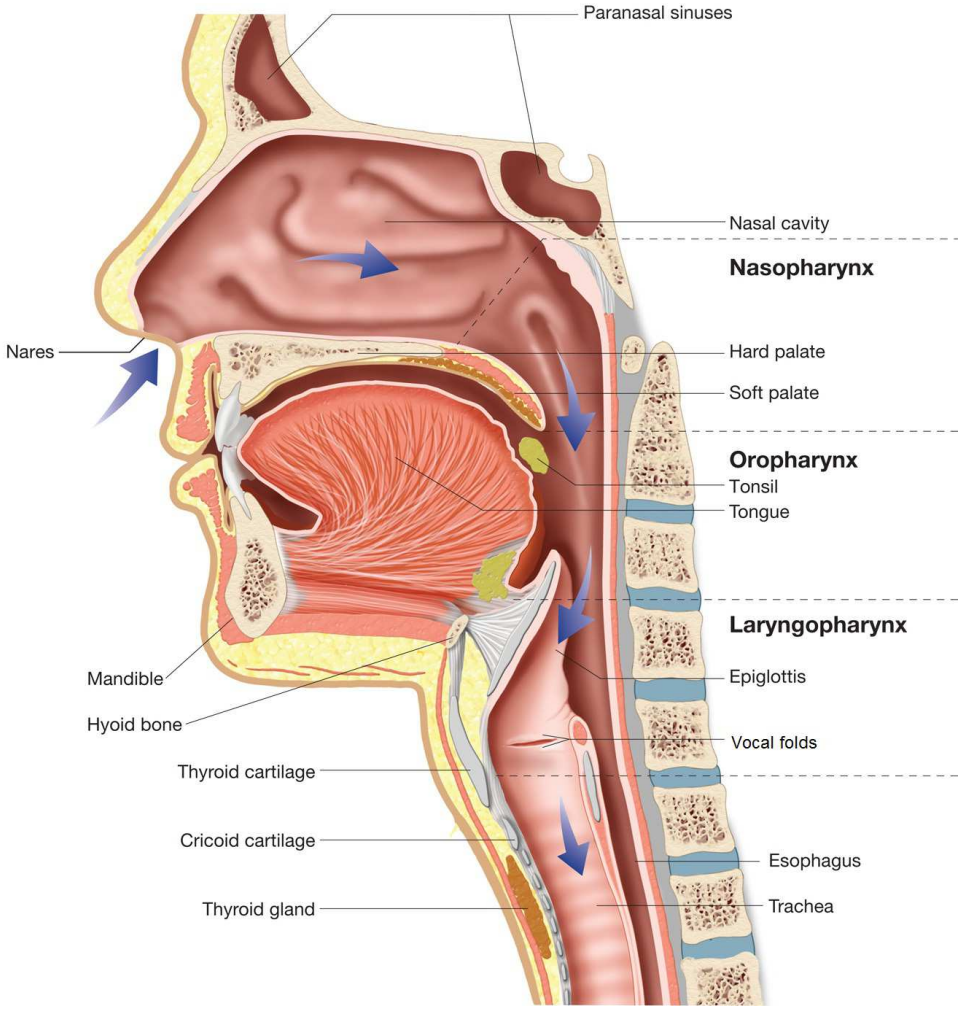

Figure 1.1: Sagittal section of upper respiratory system illustrating the internal anatomy of the nasal cavity, pharynx, larynx, and trachea, reproduced from http://biology-forums.com/index.php?action=gallery;sa=view;id=8486.

snoring, which simulated the movement of the soft palate in palatal snoring and the rhythmic collapse and opening of the pharynx observed during pharyngeal snoring, respectively. Using these simplified models they studied the biomechanics of snoring, and supposed that the instabilities in the structure of the pharynx may be due to flutter in palatal snoring and static divergence in pharyngeal snoring. Flutter and static divergence are two distinct modes of instability within the framework of linear analysis on the stability of flow over flexible structures. Flutter instability drives small disturbances on a steady state into a cycle with increasing amplitude; static divergence instability pushes small disturbances away from the steady state in an accelerating manner. Focusing on palatal snoring, Huang (1995) modelled the palate as an aerofoil with a control surface at its trailing edge, then explored the mechanism of palatal snoring employing well-understood aerodynamics of the aerofoil. Some human snore samples were compared with results from the ideal model experiments, and similarity was seen. By analysing the induced sound, they proposed that the antiphase relation of the pressure variations from the oral and nasal airways is a good test of whether snoring is caused by the soft palate vibration.

Considering local differences in anatomical and physiological properties between pharyngeal regions, Fodil *et al.* (1997) presented a two-element model, which consists of a series of two individualised segments, each having its own compliance. They studied the steady state solutions of the model and found the model has the capability to demonstrate rich mechanical behaviours. Motivated by the fact that snoring and obstructive apnoea only occur during sleep, Huang & Ffowcs Williams (1999) investigated a 'piston' model in which the neuromuscular physiology is coupled to the mechanics of airways. Theoretical results on the model exhibit three kinds of behaviour: unimpeded breathing, snoring, and obstructive sleep apnoea. They suggested that the increased latency of the reflex muscle activation in sleep, as well as the reduced strength of the reflex, have important clinical consequences.

Aittokallio *et al.* (2001) described a spatially continuous model by including spatial variation in the cross-sectional area and the velocity in the upper airway. By introducing three significant components of the respiratory system (the respiratory pump drive, the stiffness of the pharyngeal soft tissues, and the overall support of the muscles surrounding the upper airway), their model has the capability to predict the nasal flow velocity profile and to reproduce the characteristic changes in flow profile that are clinically observed in snorers and non-snorers during sleep. In addition to theoretical and experimental analysis, fully numerical simulation has been used to investigate the snor-

ing mechanism. Liu *et al.* (2007) developed a three-dimensional finite element model of the human head and neck, which predicted noise levels of snoring agreeing with the measured results by Rogelio Perez-Padilla *et al.* (1993) and Wilson *et al.* (1999). Recently, Aittokallio *et al.* (2009) reviewed mathematical modelling in understanding sleep-disordered breathing. They pointed out that combining experimental measurements with mathematical modelling has the potential to provide mechanistic insights into the individual factors underlying the disease progression, which may finally enable tailored treatment alternatives for each patient.

1.1.3 Phonation

Vocalisation is fundamental to human communication and thus to quality of life; this is therefore the most important example in the body of flow-induced oscillation. The human vocal folds are a pair of muscular folds located in the central section of the larynx known as the glottis (see figure 1.2). The position and shape of the folds can be actively controlled; for instance, during breathing the glottis tends to be fully open, but it can close completely when holding one's breath. When the folds are brought close together and the subglottal (upstream) pressure is increased beyond the so-called phonation-threshold pressure, air driven through the narrow gap can excite flow-induced oscillations that provide the main source of sound during speech and singing. The frequency of oscillation can be actively controlled by adjusting the folds' position, shape and internal tension. Stroboscopic observations show the existence of several distinct types of oscillations, often associated with different vocal registers, such as the modal register used in normal speech and characterized by large-amplitude, low-frequency oscillations (approximately 100/200 Hz for males/females), during which the folds collide, or the falsetto register in which the folds are highly stretched and perform small-amplitude, high-frequency oscillations without contact.

In early research, the two-mass model of Ishizaka & Flanagan (1972) was widely used. They considered that in the real larynx the vocal folds operate as an aerodynamic oscillator and their motion is a self-determined function of physical parameters, such as subglottal pressure, vocal-fold tension, and vocal-tract configuration. To reflect these self-oscillating properties, Ishizaka & Flanagan (1972) approximated the vocal folds as a self-oscillating sound source composed of two stiffness-coupled masses, on which the pressure acts as predicted by Bernoulli's theory. Results show that the two-mass model demonstrates principal features of vocal folds' behaviour in the human. Due

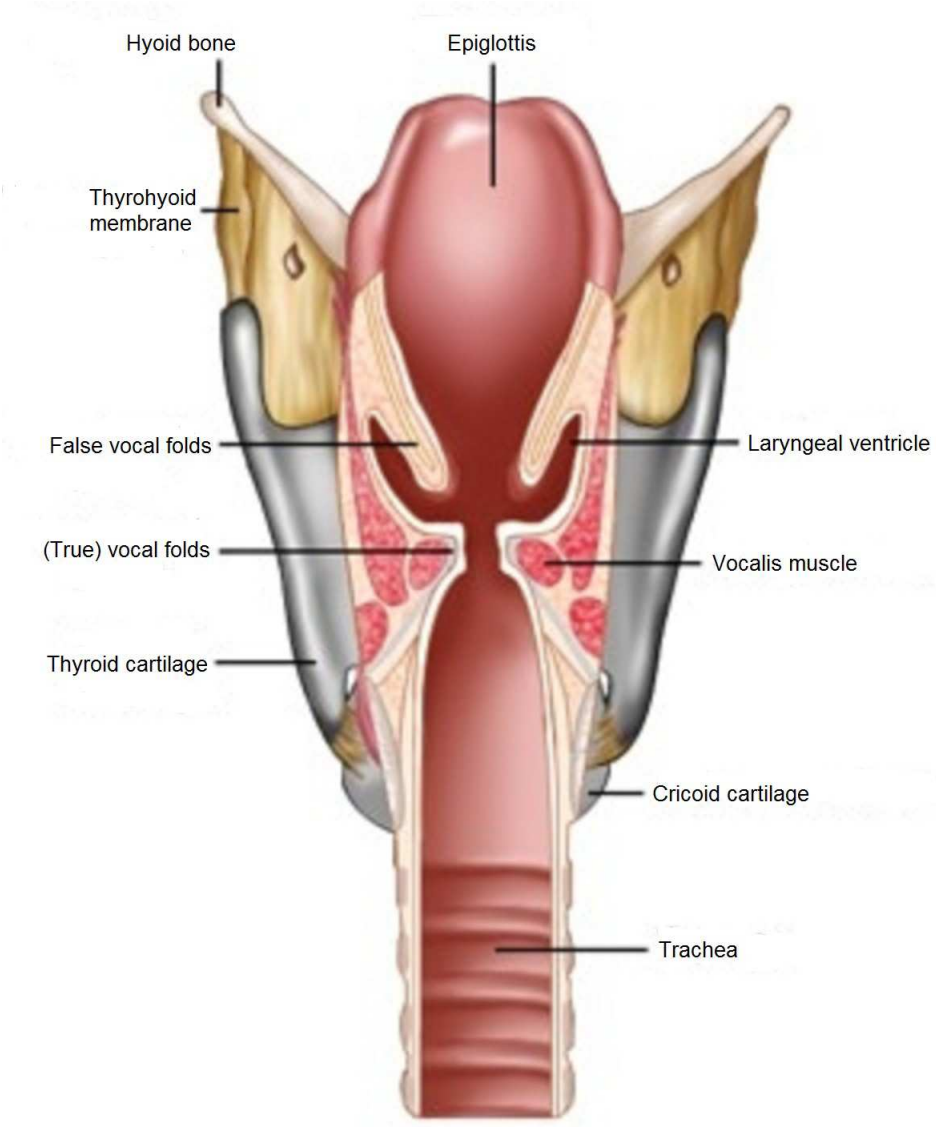

Figure 1.2: Coronal section of the larynx, showing the false and true vocal folds, reproduced from http://www.gbmc.org/home_voicecenter.cfm?id=1552.

to its simplicity, the model has been improved by many subsequent investigations. For example, Titze (1973, 1974) increased the number of masses used to represent the vocal folds, Pelorson *et al.* (1994) modified the geometry of the masses and used additional flow theory to estimate the point of flow separation within the glottis, and Story & Titze (1995) incorporated the contribution of the vocal fold body. However, the model needs some inputs (e.g. lumped parameter values and orifice coefficients) from detailed experimental data or more sophisticated models.

Numerical simulation (especially finite element simulation) has the capability to investigate in detail flow and structure behaviour, making it superior to multi-mass models. Based on basic laws of continuum mechanics, Alipour *et al.* (2000) developed a finite element model to obtain the oscillatory characteristics of the vocal folds. The model is capable of accommodating inhomogeneous, anisotropic material properties and the irregular geometry of the boundaries. de Oliveira Rosa *et al.* (2003) presented a three-dimensional finite element model to simulate the larynx during vocalization. The model considers the whole larynx (including false vocal folds and laryngeal ventricles, see figure 1.2) in three dimensions and not just the true vocal folds. They incorporated a contact-impact algorithm to deal with the physics of the collision between both true vocal folds. The simulation results showed that the simulated larynx can reproduce the vertical and horizontal phase difference in the tissue movements and that the false vocal folds affect the pressure distribution over the larynx surfaces. Hunter *et al.* (2004) employed a three-dimensional biomechanical model to simulate dynamic vocal fold abduction (the movement which separates a limb or other part from the axis, or middle line, of the body in functional anatomy) and adduction (the action by which the parts of the body are drawn towards its axis). The model was made of 1721 nearly incompressible finite elements. The results showed that the system mechanics seems to favour abduction over adduction in both peak speed and response time, even when all intrinsic muscle properties were kept identical. Using numerical simulation together with experiments on synthetic vocal fold models, Thomson *et al.* (2005) explored the aerodynamic transfer of energy from glottal airflow to vocal fold tissue during phonation. Their results confirmed the hypothesis that a cyclic variation of the orifice profile from a convergent to a divergent shape leads to a temporal asymmetry in the average wall pressure, which is the key factor for the achievement of self-sustained vocal fold oscillations.

More recently, two review articles (Alipour *et al.*, 2011; Kniesburges *et al.*, 2011) extensively surveyed mathematical models, numerical methods and experimental tech-

niques used in study of phonation process.

1.2 Self-excited oscillations in a collapsible-tube flow

1.2.1 Physical models

Oscillations in collapsible tubes can be reproduced experimentally by using a Starling resistor. In a pressure chamber, a finite-length thin-walled elastic tube (typically made of latex rubber) is mounted on two rigid tubes. In the tube, fluid (typically air or water) is driven, either by applying a controlled pressure drop between two ends of the rigid tubes or by controlling the flow rate. In terms of macroscopic flow variables (flow rate and pressure variations) and their dependence on the system parameters, early collapsible tube experiments, reviewed in Bertram (2003), identified a large number of different types of oscillations, ranging from high- to low-frequency oscillations (see figure 1.3). However, the mechanisms responsible for the onset of some of them remain poorly understood.

In a Starling Resistor, a fully three-dimensional fluid-structure problem has to be considered. This complication makes a rational theoretical analysis very difficult. In order to reduce this difficulty, Pedley (1992) introduced a two-dimensional analogue of a Starling Resistor. It comprises a two-dimensional channel, one wall of which has a segment replaced by a membrane under longitudinal tension. Viscous flow is driven along the channel by an imposed pressure drop or flow rate. The external pressure and the internal flow determine the deformation of the membrane. Although two-dimensional flow is almost impossible to produce experimentally, this system has attracted considerable theoretical attention due to its relative simplicity. In fact, it still admits self-excited oscillations and some other phenomena existing in the Starling Resistor.

1.2.2 Theoretical models

In order to describe behaviours of collapsible tubes analytically or numerically, four classes of theoretical model have been established: lumped-parameter models, one-dimensional models, two-dimensional models and three-dimensional models.

In the lumped-parameter model the system's behaviour is governed by a set of ordinary differential equations describing the temporal evolution of a small number of

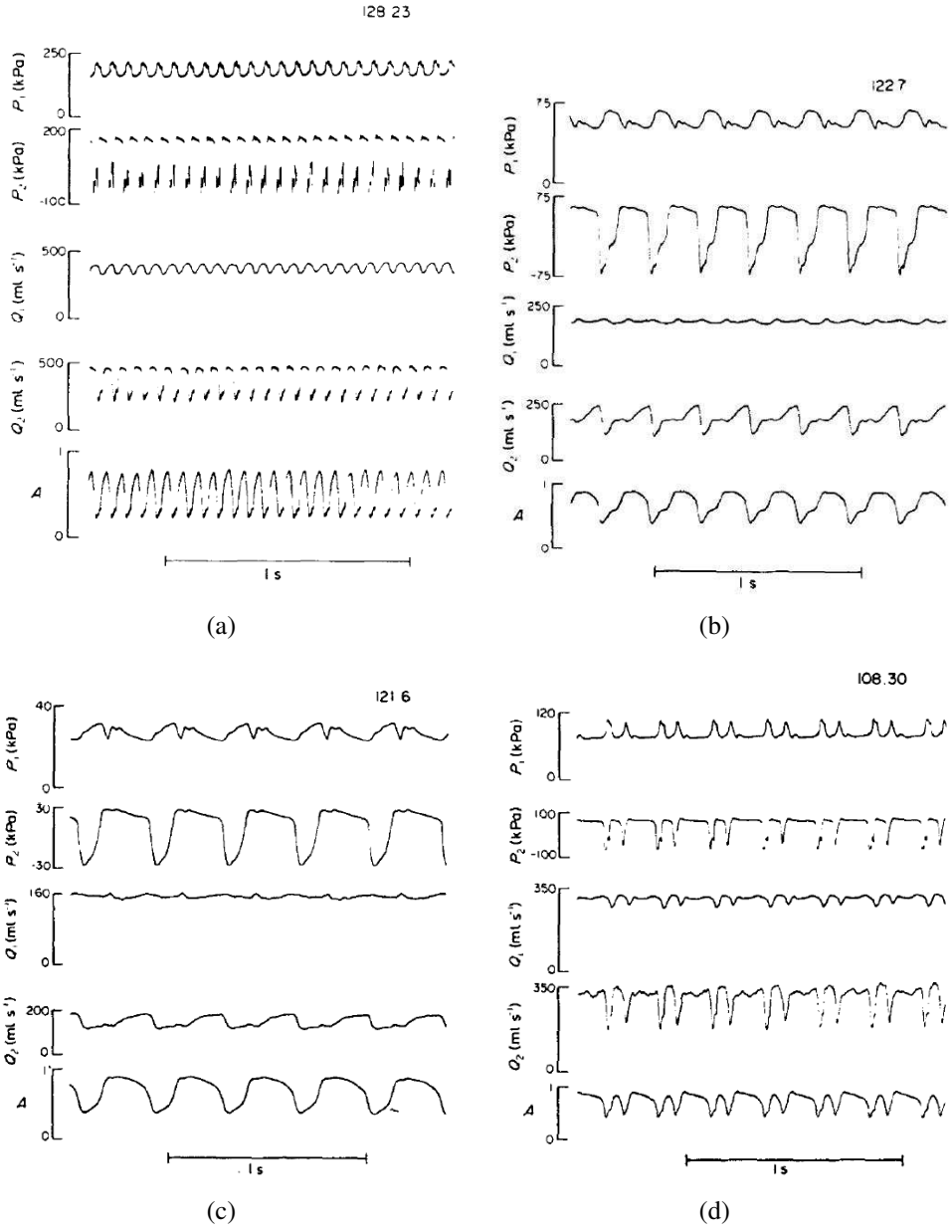

Figure 1.3: The dimensionless time-varying pressure and flow-rate at each end of the tube (P_1, P_2, Q_1, Q_2) and the dimensionless tube cross-sectional area A at the narrowest point, 'throat', recorded during self-excited oscillations in a flexible-tube flow, reproduced from Bertram (1986). (a) Oscillation at 16.08 Hz, with upstream pressure $p_u =$ 201 kPa, external pressure $p_e = 186.5$ kPa and mean pressure difference $p_e - \bar{p}_2 = 100$ kPa (where p_2 is the dimensional downstream end pressure). (b) Oscillation at 4.17 Hz, with $p_u = 64$ kPa, $p_e = 79.7$ kPa and $p_e - \bar{p}_2 = 60$ kPa. (c) Oscillation at 2.72 Hz, with $p_u = 33$ kPa, $p_e = 51.8$ kPa and $p_e - \bar{p}_2 = 40$ kPa. (d) 'Two out of three beats' oscillation at 4.09 Hz, with $p_u = 99$ kPa, $p_e = 101.4$ kPa and $p_e - \bar{p}_2 = 50$ kPa.

scalar variables (such as the cross-sectional area, the transmural pressure and the fluid velocity at the point of strongest collapse, etc.). Conrad (1969) studied the unsteady pressure-flow relations in a short collapsible tube by drawing an analogy with Van der Pol's equation. Bertram & Pedley (1982) presented a simple, third-order model based on fluid-mechanical principles to describe unsteady flow in a short segment of collapsible tube held between two rigid segments and contained in a pressurised chamber. They found that the energy loss in the seperated-flow region downstream of the point strongest collapse played an important role in the development of self-excited oscillations. In particular, if this energy loss was completely neglected (corresponding to attached, inviscid flow with completed pressure recovery, that is, the pressure downstream of the collapsed point is the same as the pressure upstream of the collapsed point), the tube was found always to choke if the flux was increased sufficiently (i.e. the tube completely closed at some point along its length in finite time). In contrast, if the enegy loss associated with flow separation was made as large as possible (corresponding to the formation of a parallel-sided jet beyond the collapsed point in the tube, along which there is no pressure recovery, that is, the pressure downstream of the collapsed point is the same as the pressure at the collapsed point), Bertram & Pedley (1982) found that steady flow was always possible and no oscillations were predicted. They found that self-excited oscillations arose only if some energy loss and some pressure recovery are allowed. Although the lumped-parameter models successfully capture many important flow features, they cannot incorporate phenomena such as wave propagation, due to the lack of the inclusion of spatial dimensions.

In the one-dimensional model, a long-wavelength approximation is employed to simplify the Navier–Stokes equations by reducing the spatial dimensions. For an incompressible fluid in a horizontal tube, the typical equations used in one-dimensional models, the conservation-of-mass equation and the momentum equation are

$$\frac{\partial A}{\partial t} + \frac{\partial (uA)}{\partial x} = 0, \tag{1.1a}$$

$$\frac{\partial u}{\partial t} + u\frac{\partial u}{\partial x} = -\frac{1}{\rho}\frac{\partial p}{\partial x} - Fu. \tag{1.1b}$$

Here $A = A(x,t)$ is the cross-sectional area of the collapsible tube, $u = u(x,t)$ is the cross-sectionally averaged axial fluid velocity, ρ the fluid density, $p = p(x,t)$ is the fluid pressure and $F = F(A,u,t) > 0$ is a friction term. By representing the relation between the transmural pressure ($p_{tm} = p - p_{ext}$, where p_{ext} is the external pressure

exerted on the collapsible tube) at any point and the cross-sectional area A at that point as a 'tube law', the elastic properties of the tube are coupled into the model. In the standard tube law, the transmural pressure p_{tm} is taken to be a single-valued function of the cross-sectional area A. The function has the general form

$$p_{tm}(x,t) = \mathscr{P}(A(x,t),x). \tag{1.2}$$

Using (1.2), the local problem (assuming that the flow domain is unbounded in the streamwise direction) has been fully studied (e.g. the detailed analysis of linear and nonlinear wave propagation in Kamm & Shapiro (1979)). For the global problem (where the tube is of finite length), the constitutive equation for the tube wall with a large axial tension T_0 and negligible wall inertia, needs to be extended by including a term representing longitudinal tension and curvature in the tube wall as

$$p_{tm}(x,t) = \mathscr{P}(A(x,t),x) - T_0\frac{\partial^2 A}{\partial x^2}, \tag{1.3}$$

which allows the application of boundary conditions at two ends (e.g. McClurken *et al.*, 1981; Cancelli & Pedley, 1985). A rational derivation of the tube law from shell theory, which gives formal justification for (1.3) for small amplitude long-wavelength deformations of a thin-walled elliptical tube at least, has been presented by Whittaker *et al.* (2010*c*). To represent the separated-flow effect found in Bertram & Pedley (1982) (mentioned above), Cancelli & Pedley (1985) slightly modified (1.1b) as

$$\frac{\partial u}{\partial t} + \chi u\frac{\partial u}{\partial x} = -\frac{1}{\rho}\frac{\partial p}{\partial x}, \tag{1.4}$$

where $\chi = 1$ for upstream and $0 < \chi < 1$ for downstream of the separation point, and χ is an indicator of the magnitude of energy loss and pressure recovery: If $\chi = 1$ there is no energy loss (no separation); if $\chi = 0$ there is no pressure recovery. The small viscous losses represented by F in (1.1b) were found to be of minor importance and were therefore neglected. In the Starling resistor, the abrupt change in cross-sectional shape and area between the throat (the most collapsed point) of the collapsible tube and the downstream rigid pipe can cause flow separation. The sudden onset of separation during collapse is believed to be largely responsible for bringing about reopening, thereby allowing relaxation oscillation (Cancelli & Pedley, 1985). However, Bertram *et al.* (1989) found the unphysiologically sudden change from compliant to rigid tubes

is not a pre-condition for self-excited oscillations in a variety of frequency bands to occur. More recently, following the the ideas of Cancelli & Pedley (1985), Anderson *et al.* (2013) presented a numerical implementation of the one-dimensional model in a segregated approach by treating the cross-sectional area function $A(x,t)$ as a known parameter, which targeted the simulation of obstructive sleep apnea particularly with a completely closing geometry. The one-dimensional models indeed give some insights into the physical mechanisms of the generation of the self-excited oscillations in the Starling resistor. However, without the help of two- or three-dimensional flow field analysis, these mechanisms are still not very clear.

The two-dimensional model in essence is a channel problem with the flow governed by the two-dimensional Navier–Stokes equations and the deformable wall modelled as a membrane (e.g. Matsuzaki & Matsumoto, 1989; Rast, 1994; Luo & Pedley, 1995, 1996, 1998, 2000) or an elastic beam (e.g. Jensen & Heil, 2003; Cai & Luo, 2003; Luo *et al.*, 2008). The fluid-membrane model used in early studies (e.g. Luo & Pedley, 1995, 1996, 1998, 2000) involves several ad hoc assumptions. First, the direction of the wall movement has to be assumed because the membrane equation alone cannot determine the movement of the material points of the elastic wall (Luo & Pedley, 1996). Secondly, the membrane model ignores the axial stiffness and hence the longitudinal stretch of the elastic wall is only balanced by a uniform tension and the transmural pressure. Thirdly, the bending stiffness of the wall is ignored. To avoid these ad hoc assumptions, the fluid-beam model was proposed to study steady (Cai & Luo, 2003) and then unsteady flows (Luo *et al.*, 2008). In terms of steady behaviour, the beam model agrees well with the membrane (constant-tension) model as long as the additional stretch-induced tension is small compared to the initial constant tension. Some numerical simulations made by Luo *et al.* (2008) are shown in figure 1.4. The two-dimensional channel model is a rational and (at least in principle) physically realisable system which can be interpreted as an approximation to the flow in a strongly collapsed three-dimensional tube. However, as Heil & Jensen (2003) suggested, the two-dimensional model excludes many potentially important three-dimensional effects: (i) when the tube is moderately collapsed the flow field presents strong three-dimensionality; (ii) the flow separation in two-dimensional flows is significantly different from that in there-dimensional flows; (iii) as the tube changes from an axisymmetric to a non-axisymmetrically buckled state its wall stiffness varies drastically.

The first rigorous three-dimensional computational model of flow in collapsible

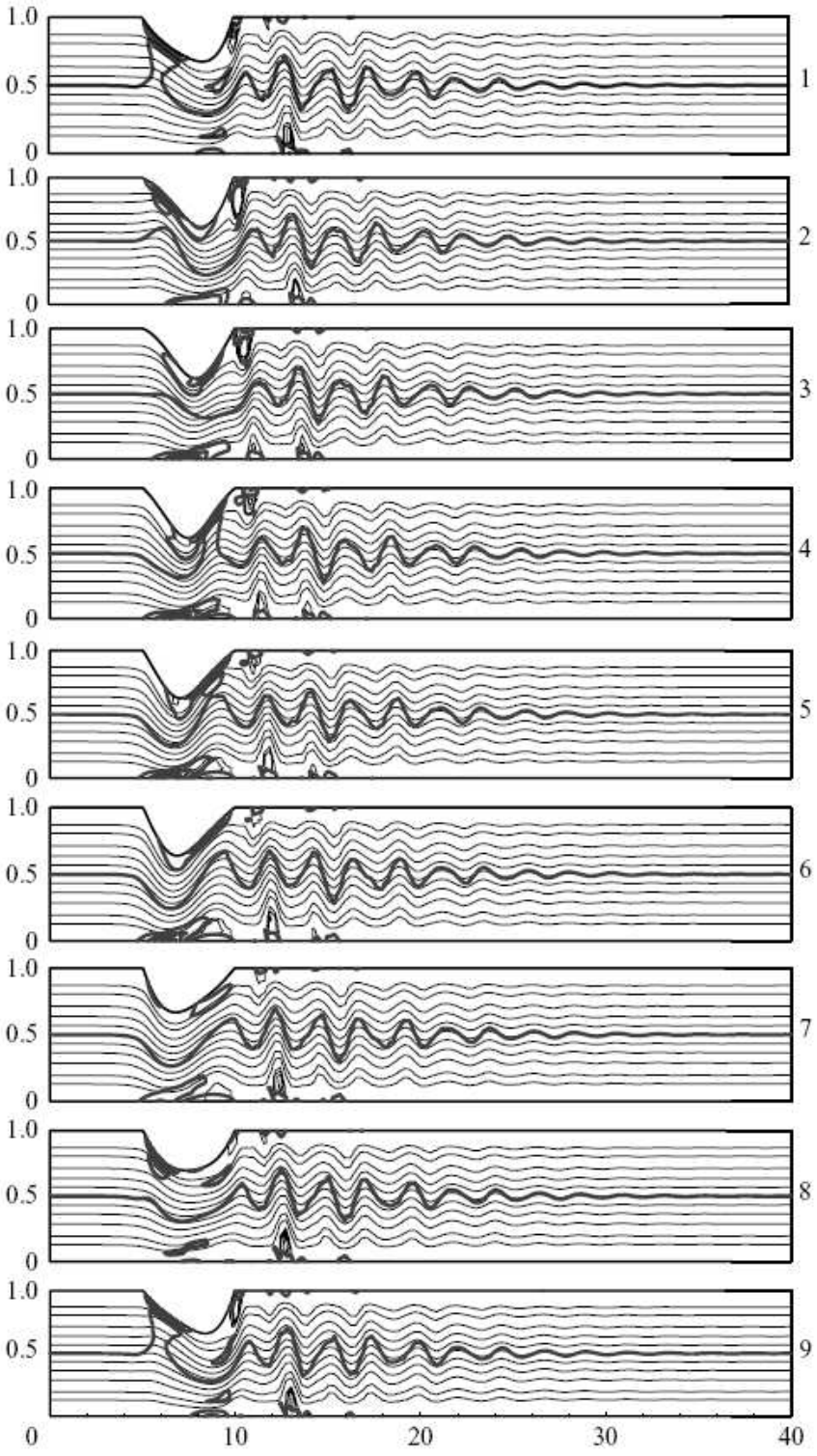

Figure 1.4: Wall shape, instantaneous streamlines (thin lines) and vorticity contours (thick lines) during self-excited oscillations of a collapsible channel using a fluid-beam model, reproduced from Luo *et al.* (2008).

tubes was given in Heil (1995). The key contribution of Heil (1995) is that a large displacement, geometrically nonlinear shell theory was proposed to describe the deformation of the collapsible tube which was modelled as a thin-walled elastic shell. By using nonlinear shell theory, firstly steady viscous (Stokes) flow (Heil, 1997, 1998) and, later, finite-Reynolds-number flow (Hazel & Heil, 2003), in three-dimensional collapsible tubes were studied. Then unsteady cases were considered: Heil & Waters (2008) presented a combination of theoretical and computational analysis of three-dimensional unsteady finite-Reynolds-number flows in collapsible tubes whose walls perform prescribed high-frequency oscillations; Heil & Boyle (2010) explored the onset of self-excited oscillations and the subsequent large-amplitude oscillations in three-dimensional collapsible tubes with full coupling between the fluid and solid mechanics.

In all these models, self-excited oscillations are found at least numerically, e.g. in the lumped-parameter model of Bertram & Pedley (1982), the one-dimensional model of Cancelli & Pedley (1985); Jensen (1992), the two-dimensional model of Luo & Pedley (1996, 1998, 2000); Jensen & Heil (2003), and the three-dimensional model of Heil & Boyle (2010); Whittaker *et al.* (2010*b*).

1.2.3 Sloshing mechanism

However, no simple and satisfactory theoretical analysis that is compatible with existing numerical or experimental results was presented until the sloshing mechanism was described by Jensen & Heil (2003). By combining rational asymptotic analysis with direct numerical simulation, Jensen & Heil (2003) identified a simple and clear mechanism that not only is responsible for the initial instability but also controls the large-amplitude oscillations that develop subsequently. This and some following studies (e.g. Heil & Waters, 2006, 2008; Whittaker *et al.*, 2010*d*,*a*) show that the mechanism operates in two and three dimensions.

The mechanism is as follows. When viscous effects are weak, the channel or tube supports a family of inviscid normal modes, in which transverse wall deformations generate predominantly axial oscillations of the fluid in the entire tube. If the amplitude of the resulting sloshing flows is greater in the rigid upstream section than in its downstream counterpart, then there can be a net influx of kinetic energy into the system in the presence of a mean flow. If this influx exceeds any additional losses, such as viscous dissipation, oscillations can grow by extracting energy from the mean flow. For the two-dimensional model, Jensen & Heil (2003) presented predictions for

the frequency and growth rates of instabilities arising through this mechanism, in the limit of large wall tension. Assuming the flow is driven by a fixed pressure drop, they showed that the required upstream/downstream asymmetry of the sloshing flow can be generated by making the rigid downstream part longer than its upstream counterpart. The theoretically predicted critical Reynolds number at which oscillations grow is in excellent agreement with results from direct numerical simulation for Navier–Stokes equations, even in cases in which the tension is relatively small and oscillations are of modest frequency (Jensen & Heil, 2003).

In three dimensions, by using asymptotic analysis of high-frequency oscillations of fluid-conveying elastic tubes, Heil & Waters (2006) showed that, for sufficiently small amplitudes, the three-dimensional unsteady flow induced by the wall motion is independent of the steady through-flow. Furthermore, the average axial velocities that are generated by the wall motion are much smaller than the corresponding transverse velocities, suggesting that the dominant flow occurs in the tube's cross-sections. This is very different from the two-dimensional case investigated by Jensen & Heil (2003), where wall oscillations drive axial sloshing flows which play an important role in the onset of the self-excited oscillations. Instead, by analysing the system's energy budget under prescribed high-frequency wall oscillations, Heil & Waters (2008) showed that efficient extraction of energy from the mean flow via the sloshing mechanism requires the tube to perform oscillations about a non-axisymmetric mean configuration. Moreover, by using numerical simulations of fully-coupled three-dimensional fluid-structure interaction, Heil & Boyle (2010) showed self-excited oscillations readily arise from steady equilibrium configurations in which the tube is buckled non-axisymmetrically, and that short tubes tend to approach an approximately axisymmetric equilibrium configuration in which the oscillations decay whereas sufficiently long tubes develop sustained large-amplitude limit-cycle oscillations. These findings are consistent with experimental results showing that self-excited oscillations readily develop from the steady-state configurations in which the tube is strongly buckled (Bertram *et al.*, 2008).

In a series of papers, Whittaker *et al.* (2010*d*,*c*,*b*,*a*, 2011) performed asymptotic analysis of self-excited oscillations based on three-dimensional theoretical models in which the Navier–Stokes equations are coupled to large displacement elasticity theory. First, they analysed the fluid (Whittaker *et al.*, 2010*d*,*a*) and solid (Whittaker *et al.*, 2010*c*) mechanics of the problem in isolation. Then, combining these results, they studied the development of small-amplitude long-wavelength high-frequency os-

cillations in an elastic tube of initially elliptical cross section (Whittaker *et al.*, 2010*b*). Their results provided the first asymptotic predictions for the onset of self-excited oscillations in three-dimensional collapsible tube flows. They suggested that, at least in the parameter regime that they considered, self-excited oscillations in three-dimensional systems can arise through the sloshing mechanism.

1.2.4 Pressure- vs. flux-driven system

In the laboratory, flow in a Starling resistor can be driven by either a given pressure drop or a given inlet volume flux. Therefore, two kinds of boundary conditions, fixed pressure-drop or fixed flux, can be imposed on a collapsible tube flow. In the frame of collapsible channel flows, it is found these two systems (pressure- and flux-driven) can demonstrate significantly distinct stability behaviour.

Using a fluid-membrane model with fixed inlet flow, Luo & Pedley (1996) described a kind of low-frequency self-excited oscillation numerically. Here, the primary instability is mode-2 (the channel width perturbation has two spatial extrema). The oscillation cannot be explained by the sloshing mechanism proposed by Jensen & Heil (2003), in which a pressure-driven model was used. The asymptotic analysis of Jensen & Heil (2003) predicted that the primary instability is mode-1 (with a single spatial maximum in the width perturbations), which can lead to self-excited oscillations. Furthermore, combining numerical simulation with linear stability analysis, Luo *et al.* (2008) found a cascade structure of instabilities for a fluid-beam model with inlet flow. They discovered that, under small perturbations to steady solutions for the same Reynolds number, the system loses stability by passing through a succession of unstable zones, with mode number increasing as the wall stiffness, C_λ, is decreased (see figure 1.5). The cascade structure was also reported in earlier one-dimensional models (Jensen, 1990, 1992). The cascade phenomenon for a flow-driven system was reproduced by Liu *et al.* (2009) using the commercial package ADINA. Liu *et al.* (2009) also confirmed that the lowest unstable mode number is primarily determined by the nature of the inlet boundary conditions; it is mode-1 if the system is pressure-driven, and mode-2 if it is flow-driven. However, they did not show whether the cascade structure still exists if the system switches from being flow-driven to pressure-driven. More recently, Liu *et al.* (2012) found that the stability structure for the pressure-driven system is not a cascade as in the flow-driven case, and the mode-2 instability is no longer the primary mode of self-excited oscillation. Instead, mode-1 instability becomes the

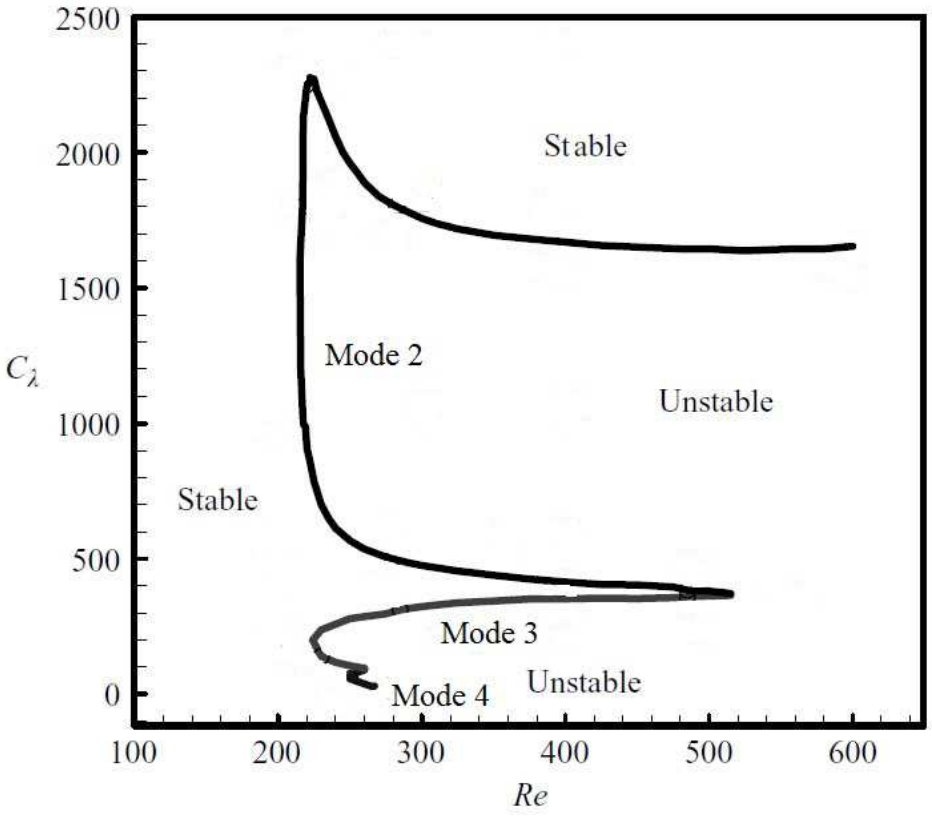

Figure 1.5: Neutral stability curve in the (C_λ, Re)-space, reproduced from Luo *et al.* (2008), where C_λ is dimensionless extensional stiffness and Re is Reynolds number. The system is stable on the left of the branches and the top of Mode 2, and on the right of branches (below Mode 2), it is unstable.

dominant unstable mode. The mode-2 neutral curve is found to be completely enclosed by the mode-1 neutral curve in the pressure drop and wall stiffness space; hence no purely mode-2 unstable solutions exist in the parameter space investigated.

1.2.5 Local vs. global modes

Flow instabilities in collapsible channel or tube can be described in two different ways: models of local instabilities in unbounded domains without boundary conditions; and models of global instabilities in bounded or non-uniform domains confined by boundary conditions. Local instabilities can manifest themselves in different ways. Absolute instabilities occur if perturbations grow in time at every fixed point in the unbounded domain. Convective instabilities are characterized by the fact that, even though the overall norm of the perturbation grows in time, perturbations ultimately decay locally at every fixed point in the unbounded domain; in other words, the growing perturbation is transported, or convected, towards infinity. Related to collapsible-channel (tube) flows, there are two categories of local modes: hydrodynamic modes, which may be perturbed by a flexible wall; and 'surface' or 'wall' modes, which only exist in the presence of flexible walls. Among the former group, two modes are worth highlighting: the Tollmien–Schlichting (TS) mode, which could not exist without viscosity; and the 'Womersley' mode in a rigid channel, corresponding to an axially uniform oscillatory flow. For a channel having one wall rigid and the other a massless membrane, the wall modes are either 'static divergence' (SD) or 'travelling-wave flutter' (TWF) (following Carpenter & Garrad (1985, 1986)): while SD is stable (in the absence of wall damping), TWF is long-wave unstable at all non-zero Reynolds numbers (Stewart *et al.*, 2010*b*).

It is instructive to interpret global instabilities in terms of the underlying local modes of instabilities in homogeneous channels or tubes. Motivated by the method of Doaré & de Langre (2006), Stewart *et al.* (2009) decomposed the global mode (mode 1) of instabilities into four wall modes in the compliant segment (i.e. upstream- and downstream-propagating SD and TWF) and showed that global growth arises through wave reflections at the boundaries between the flexible and compliant segments even when local modes are convectively stable, initially using a one-dimensional analogue of the Starling resistor. For the two-dimensional Starling resistor analogue, Stewart *et al.* (2010*a*) solved an Orr–Sommerfeld-like equation to identify the full spectra of local modes in both the rigid and compliant channel segments, without making any

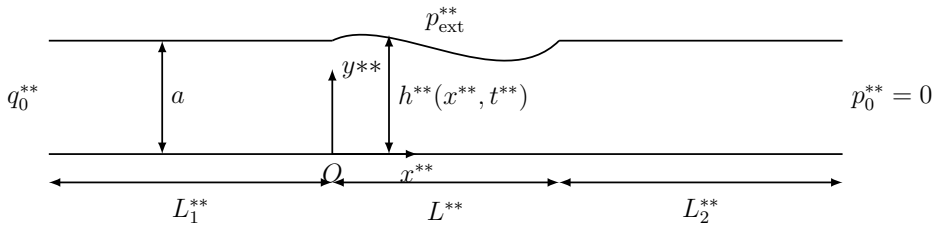

Figure 1.6: The flow domain, showing variables and parameters. The membrane occupies $0 < x^{**} < L^{**}$; the channel is rigid otherwise. Fixed upstream volume flux and zero downstream pressure are given at inlet and outlet of the channel, respectively.

long-wavelength or high-frequency approximations. Stewart *et al.* (2010*a*) expressed the flow in the rigid segments of the channel as a linear combination of infinitely many hydrodynamic modes, which include one Wormersley mode and one TS mode, expressed the flow in the compliant segment of the channel as a linear combination of four wall modes (two TWF and two SD) and infinitely many hydrodynamic modes, and then matched truncated mode expansions across junctions using a technique developed by Manuilovich (2004). Stewart *et al.* (2010*a*) found that at high membrane tension the sloshing mechanism (Jensen & Heil, 2003) at the global level can be explained as a consequence of wave reflections of SD and TWF modes at the junctions with the rigid channel segments (Stewart *et al.*, 2009) at the local level. However, an analysis of the system's energy budget by Stewart *et al.* (2010*a*) suggests that at low membrane tension, the dominant source of energy responsible for the growth of the oscillations switches from the influx of kinetic energy (the signature of the sloshing mechanism) to a reduction in the total viscous dissipation in the flow, indicating that the oscillations are governed by a different mechanism. At low tensions, Stewart *et al.* (2010*a*) also found wave-like flow features in the downstream rigid section via the excitation of hydrodynamic modes. For the three-dimensional model of Starling resistor, the approach that constructs global modes by local modes have not been considered. However, many local modes of instabilities of fluid flow in a flexible three-dimensional tube have been found, reviewed by Kumaran (2003), such as 'viscous modes' (Kumaran, 1995) and 'wall modes' (Kumaran, 1998), which may form the base of the construction in the three-dimensional case.

1.3 Formulation of a one-dimensional model

In this thesis, theoretical analysis is focused on a one-dimensional model of flexible-channel flow, which was previously presented by Stewart *et al.* (2009). The only difference is that here the flow is subject to a fixed upstream volume flux rather than a fixed upstream pressure.

1.3.1 Navier–Stokes equations

We consider a planar channel through which a fluid is driven by a prescribed upstream volume flux. One wall of the channel contains a segment of thin elastic membrane under constant longitudinal tension T_0 and subject to an external pressure $p^{**}_{\rm ext}$. The channel walls elsewhere are rigid, and the membrane is assumed massless and free of any internal dissipation in the one-dimensional model. When the membrane is flat, the channel has uniform width a and the membrane has length L^{**}. The lengths of the rigid segments of the channel upstream and downstream of the membrane are L^{**}_1 and L^{**}_2, respectively.

We introduce Cartesian coordinates (x^{**},y^{**}) (see figure 1.6) so that the channel walls lie at $y^{**}=0$ and $y^{**}=a$ (where the channel walls are rigid, that is for $-L^{**}_1 \le x^{**} < 0$ and $L^{**} < x^{**} \le L^{**}+L^{**}_2$), or $y^{**}=0$ and $y^{**}=h^{**}(x^{**},t^{**})$ (where the channel wall is flexible, for $0 \le x^{**} \le L^{**}$). Here $h^{**}(0,t^{**}) = h^{**}(L^{**},t^{**}) = a$ for all time t^{**}. The velocity $\mathbf{u}^{**}=(u^{**},v^{**})$ of fluid of density ρ and dynamic viscosity μ is governed by the Navier-Stokes equations

$$\nabla^{**}\cdot\mathbf{u}^{**} = 0, \tag{1.5a}$$

$$\rho\frac{\mathrm{D}\mathbf{u}^{**}}{\mathrm{D}t^{**}} = -\nabla^{**}p^{**} + \mu(\nabla^{**})^2\mathbf{u}^{**}, \tag{1.5b}$$

where p^{**} is the fluid pressure and $\nabla^{**} = (\partial/\partial x^{**}, \partial/\partial y^{**})$. Given fixed upstream flux $q^{**}_0 = \int_0^a u^{**}(x^{**}=-L^{**}_1)\mathrm{d}y^{**}$, we introduce a velocity scale $U_0 = q^{**}_0/a$. We nondimensionlize as

$$\begin{aligned}&(x^*,y^*,h^*,L^*_1,L^*,L^*_2) = (x^{**},y^{**},h^{**},L^{**}_1,L^{**},L^{**}_2)/a, \quad t^* = t^{**}U_0/a,\\ &\mathbf{u}^* \equiv (u^*,v^*) = (u^{**},v^{**})/U_0, \quad (p^*,p^*_{\rm ext}) = (p^{**},p^{**}_{\rm ext})/\rho U_0^2,\end{aligned} \tag{1.6}$$

see figure 1.7. In this case the dimensionless fixed upstream flux $q^*_0 = \int_0^1 u^*(x^* =$

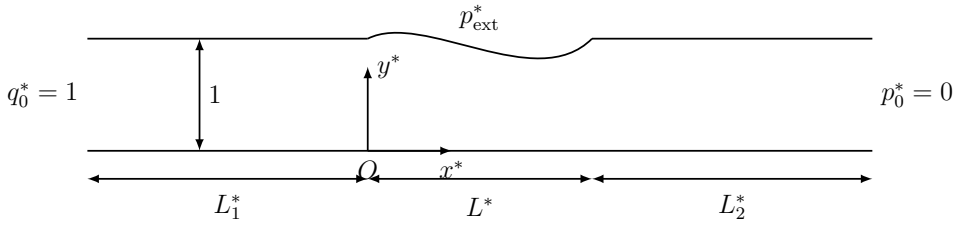

Figure 1.7: The flow domain, showing dimensionless variables and parameters.

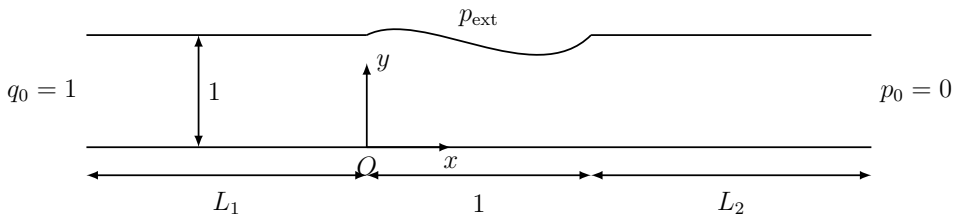

Figure 1.8: The flow domain, showing rescaled variables and parameters.

$-L_1^*)\mathrm{d}y^* = 1$. With the Reynolds number defined as $Re = \rho a U_0/\mu$, the dimensionless Navier-Stokes equations are

$$\nabla^* \cdot \mathbf{u}^* = 0, \tag{1.7a}$$

$$\frac{\mathrm{D}\mathbf{u}^*}{\mathrm{D}t^*} = -\nabla^* p^* + \frac{1}{Re}(\nabla^*)^2 \mathbf{u}^*, \tag{1.7b}$$

where $\nabla^* = (\partial/\partial x^*, \partial/\partial y^*)$.

1.3.2 Boundary-layer equations

To facilitate theoretical analysis, we assume that the membrane shape is only determined by the normal stress balance, given by

$$p^* = p^*_{\text{ext}}(x^*) - T^* h^*_{x^*x^*}(1 + (h^*_x)^2)^{-3/2}, \tag{1.8}$$

on $y^* = h^*(x^*, t^*)$, $0 \le x^* \le L^*$, where $T^* = T_0/(\rho U_0^2 a)$ and $p^*_{\text{ext}}(x^*)$ is the nondimensionless external pressure distribution. Here, for simplicity, we only include the effects of constant longitudinal tension T^*, and neglect the effects of bending stiffness, wall damping and wall inertia.

Suppose now that all three segments of the channel are long compared to the chan-

nel width, we make a long-wavelength rescaling by writing

$$x^* = xL^*, \quad v^* = \frac{v}{L^*}, \quad t^* = tL^*, \quad Re = \frac{L^*}{\mathscr{R}},$$
$$T^* = T(L^*)^2, \quad L_1^* = L_1 L^*, \quad L_2^* = L_2 L^*, \tag{1.9}$$

and denoting

$$(y^*, h^*) = (y, h), \quad u^* = u, \quad (p^*, p_{\text{ext}}^*) = (p, p_{\text{ext}}), \quad q_0^* = q_0. \tag{1.10}$$

See figure 1.8 for rescaled configuration. Then (1.7) is transformed to

$$\nabla \cdot \mathbf{u} = 0, \tag{1.11a}$$
$$u_t + (\mathbf{u} \cdot \nabla)u = -p_x + \mathscr{R}(u_{yy} + (L^*)^{-2} u_{xx}), \tag{1.11b}$$
$$(L^*)^{-2}[v_t + (\mathbf{u} \cdot \nabla)v] = -p_y + (L^*)^{-2}\mathscr{R}(v_{yy} + (L^*)^{-2} v_{xx}), \tag{1.11c}$$

where $\mathbf{u} \equiv (u, v)$ and $\nabla = (\partial/\partial x, \partial/\partial y)$, which reduces with error $O((L^*)^{-2})$ to the unsteady boundary-layer equations,

$$u_x + v_y = 0, \tag{1.12a}$$
$$u_t + uu_x + vu_y = -p_x + \mathscr{R} u_{yy}, \tag{1.12b}$$
$$p_y = 0. \tag{1.12c}$$

Along the rigid parts of the channel walls we impose $(u, v) = (0, 0)$, while along $y = h(x,t), 0 < x < 1$ the non-slip and kinematic conditions are

$$u = 0, \quad v = h_t. \tag{1.13}$$

The membrane is assumed to move in the vertical direction only. The normal-stress condition reduces, with error $O((L^*)^{-2})$, from (1.8) to

$$p = p_{\text{ext}}(x) - T h_{xx}, \qquad (y = h(x,t), 0 \le x \le 1). \tag{1.14}$$

1.3.3 Integrated equations

Integrating (1.12) across the width of the channel, we obtain the mass and momentum integral equations

$$h_t + q_x = 0, \tag{1.15a}$$

$$q_t + \left(\int_0^h u^2 \mathrm{d}y \right)_x = -hp_x + \mathscr{R}[u_y]_0^h. \tag{1.15b}$$

where $q(x,t) \equiv \int_0^{h(x,t)} u(x,y,t)\mathrm{d}y$ is the volume flux. To close this system of equations we employ a von Kármán–Polhausen approximation, and assume that the axial velocity component takes the self-similar form

$$u = \frac{q}{h} f\left(\frac{y}{h}\right), \tag{1.16a}$$

where the function f satisfies

$$\int_0^1 f(y)\mathrm{d}y = 1, \quad f(0) = f(1) = 0. \tag{1.16b}$$

Let

$$\alpha = \int_0^1 [f(y)]^2 \mathrm{d}y, \quad \beta = f'(0) - f'(1) > 0, \tag{1.17}$$

then (1.15b) becomes

$$q_t + \alpha \left(\frac{q^2}{h} \right)_x = -hp_x - \frac{\mathscr{R}\beta q}{h^2}. \tag{1.18}$$

For Poiseuille flow, we have $f(y) = 6y(1-y)$, $\alpha = 6/5$ and $\beta = 12$. For a flow that is not fully developed, α will be closer to 1 and $\beta \gg 12$. Since β and $\mathscr{R}$ always appear in the combination $\mathscr{R}\beta$, any variation in the magnitude of β can be accommodated by a change in $\mathscr{R}$. Thus it is sufficient to use the Poiseuille value $\beta = 12$. However α is an independent parameter approximately between 1 and $6/5$. We retain $\alpha = 6/5$ in most part of the thesis and analyse the effect of the variation of α between 1 and $6/5$

in §2.2.2. Therefore, (1.15) becomes

$$h_t + q_x = 0, \tag{1.19a}$$

$$q_t + \frac{6}{5}\left(\frac{q^2}{h}\right)_x = -hp_x - \frac{12\mathscr{R}q}{h^2}. \tag{1.19b}$$

According to equation (1.19a), $q_x = 0$ in the rigid segment of the channel upstream of the membrane ($-L_1 \le x \le 0$) and the rigid downstream segment ($1 \le x \le 1+L_2$) due to $h = 1$ there. Furthermore, with the prescribed volume flux $q_0 = 1$ at $x = -L_1$, it can be found that $q = 1$ in the entire rigid upstream segment ($-L_1 \le x \le 0$). From (1.19b) we have

$$p_x = -12\mathscr{R}, \tag{1.20}$$

in the rigid upstream segment, and

$$p_x = -12\mathscr{R}q - q_t, \tag{1.21}$$

in the rigid downstream segment. Integrating (1.20) from $x = -L_1$ to $x = 0$ and (1.21) from $x = 1$ to $x = 1+L_2$, we obtain

$$p = p(-L_1, t) - 12\mathscr{R}L_1, \qquad (x = 0), \tag{1.22}$$

and

$$p = \Big(12\mathscr{R}q + q_t\Big)L_2, \qquad (x = 1). \tag{1.23}$$

Applying the normal-stress condition (1.14) at $x = 1$, we obtain

$$\Big(12\mathscr{R}q + q_t\Big)L_2 = p_{\text{ext}}(x) - Th_{xx}. \tag{1.24}$$

In order that the system admit $h = 1$ and $q = 1$ for $-L_1 \le x \le 1+L_2$, we assume that

$$p_{\text{ext}}(x) = 12\mathscr{R}(L_2 + 1 - x), \tag{1.25}$$

for $0 \le x \le 1$. With the normal-stress condition (1.14) and the prescribed external pressure (1.25), the simplified model for flow in the compliant segment of the channel

is derived from the integral equations (1.19), which can be expressed as

$$h_t + q_x = 0, \tag{1.26a}$$

$$q_t + \frac{6}{5}\left(\frac{q^2}{h}\right)_x = Thh_{xxx} + 12\mathscr{R}\left(h - \frac{q}{h^2}\right), \tag{1.26b}$$

for $0 \leq x \leq 1$, with boundary conditions

$$h = 1, \qquad (x = 0), \tag{1.27a}$$

$$q = 1, \qquad (x = 0), \tag{1.27b}$$

$$h = 1, \qquad (x = 1), \tag{1.27c}$$

$$Th_{xx} = -(12\mathscr{R}(q-1) + q_t)L_2, \qquad (x = 1). \tag{1.27d}$$

If q, h and p_{ext} are given, the pressure can be expressed as

$$p(x,t) = \begin{cases} (12\mathscr{R}q + q_t)(1 + L_2 - x), & (1 \leq x \leq 1 + L_2), \\ 12\mathscr{R}(L_2 + 1 - x) - Th_{xx}, & (0 \leq x \leq 1), \\ p(0,t) - 12\mathscr{R}x, & (-L_1 \leq x \leq 0), \end{cases} \tag{1.28}$$

Thus, the pressure difference across the membrane is

$$\Delta p \equiv p(0,t) - p(1,t) = 12\mathscr{R} - T(h_{xx}(0,t) - h_{xx}(1,t)). \tag{1.29}$$

1.3.4 Energy Budget

The kinetic energy of the flow in the collapsible segment of the channel (scaled on $\rho U_0^2 a$) takes the form

$$K(x,t) = \int_0^{h(x,t)} \tfrac{1}{2}u(x,y,t)^2 \mathrm{d}y = \frac{3}{5}\frac{q^2}{h}, \tag{1.30}$$

again assuming a parabolic velocity profile. By multiplying both sides of the momentum equation in (1.19) by $6q/5h$, we derive the corresponding energy equation for flow in the channel, which takes the form (Stewart *et al.*, 2009)

$$\frac{3}{5}\left(\frac{q^2}{h}\right)_t + \frac{18}{25}\left(\frac{q^3}{h^2}\right)_x + \frac{3}{25}\left(\frac{q^2 q_x}{h^2}\right) = -\frac{6}{5}qp_x - \frac{72\mathscr{R}}{5}\frac{q^2}{h^3}. \tag{1.31}$$

In particular, for the flow in the rigid sections of the channel, the energy equation takes simpler form because $h = 1$ and $q = 1$ or $q(t)$.

Integrating along the channel, that is from $x = -L_1$ to $x = 1 + L_2$, we can sum the contributions from each region and split the energy equation into five components.

$$\mathscr{K} + \mathscr{E} = \mathscr{F} + \mathscr{P} - \mathscr{D}, \tag{1.32}$$

where

$$\mathscr{K} = \frac{3}{5}\frac{\partial}{\partial t}\left(\int_0^1 \frac{q^2}{h}\mathrm{d}x + L_1 + q(1,t)^2 L_2\right), \tag{1.33a}$$

$$\mathscr{F} = \frac{18}{25}(1 - q(1,t)^3), \tag{1.33b}$$

$$\mathscr{P} = \frac{6}{5}\left(p(0,t) + 12\mathscr{R}L_1\right), \tag{1.33c}$$

$$\mathscr{E} = \frac{6}{5}\int_0^1 h_t p \mathrm{d}x, \tag{1.33d}$$

$$\mathscr{D} = \frac{72\mathscr{R}}{5}\left(\int_0^1 \frac{q^2}{h^3}\mathrm{d}x + L_1 + q(1,t)^2 L_2\right) + \frac{3}{25}\int_0^1 \frac{q^2 q_x}{h^2}\mathrm{d}x. \tag{1.33e}$$

Here $\mathscr{K}$ represents rate of exchange of kinetic energy, $\mathscr{F}$ net kinetic energy flux, $\mathscr{P}$ rate at which upstream pressure does work on fluid, $\mathscr{E}$ rate at which fluid does work on membrane and $\mathscr{D}$ viscous dissipation plus a non-conservative term which arises from the von Kármán–Polhausen approximation. We notice that terms involving L_1 in $\mathscr{P}$ and $\mathscr{D}$ can cancel out and that in $\mathscr{K}$ can vanish. Therefore, in the following we neglect the contributions from the upstream section of the channel in the energy budget equation (1.32).

1.4 Formulation of a two-dimensional model

1.4.1 Fluid equations

In this thesis we also perform numerical simulations of the corresponding two-dimensional fluid-structure interaction problem. In the two-dimensional flexible-channel problem, the fluid governing equations are the dimensionless Navier-Stokes equations (1.7) and the geometry configuration is shown in figure 1.7. At the inlet of the channel $x^* = -L_1^*$, unit-flux Poiseuille flow $\mathbf{u}^* = (6y^*(1-y^*), 0)$ is prescribed. At the outlet $x^* = L^* + L_2^*$,

we impose zero normal stress. The external pressure distribution consistent with (1.25) is $p^*_{\text{ext}} = 12(L^* + L^*_2 - x^*)/Re$ in $0 \le x^* \le L^*$ such that the system admits steady unit-flux Poiseuille flow along the channel. In this case there is no pressure difference across the membrane and $h^* = 1$.

1.4.2 Wall equations

We model the membrane as a thin-walled elastic Kirchhoff–Love beam of wall thickness h_0^{**} and density ρ_w, which is subject to an axial (second Piola–Kirchhoff) pre-stress $\sigma_0^{**} = T_0/h_0^{**}$ (where T_0 is the initial longitudinal tension) in the undeformed position. Using the Lagrangian coordinate $\zeta^{**} \in [0, L^{**}]$, the position vector to material points on the undeformed wall is given by $\mathbf{r}_w^{**}(\zeta^{**}) = (\zeta^{**}, a)^T$. The displacement field $\mathbf{d}^{**} = (d^{(x)**}, d^{(y)**})^T$ displaces material points to their new position $\mathbf{R}_w^{**}(\zeta^{**}, t^{**}) = \mathbf{r}_w^{**}(\zeta^{**}) + \mathbf{d}^{**}(\zeta^{**}, t^{**})$. Because the beam is thin, the axial component of the second Piola–Kirchoff stress tensor σ^{**} is dominant during wall deformation. The Kirchhoff–Love assumption results in only the geometrically nonlinear axial extensional stain, $\gamma = d^{(x)**}_{\zeta^{**}} + ((d^{(x)**}_{\zeta^{**}})^2 + (d^{(y)**}_{\zeta^{**}})^2)/2$, being non-zero, where a subscript denotes a partial derivative. The assumption of small strains enables us to apply the incrementally linear constitutive relation $\sigma^{**} = \sigma_0^{**} + E\gamma$, where E is the incremental Young's modulus. The wall deformation is governed by the principle of virtual displacements (Heil & Hazel, 2006)

$$\int_0^{L^{**}} \left[\sigma^{**}\delta\gamma + \frac{E}{12}(h_0^{**})^2 \kappa^{**}\delta\kappa^{**} - \left(\frac{1}{h_0^{**}} \sqrt{\frac{A_2}{A_1}} \mathbf{f}^{**} - \rho_w \frac{\partial^2 \mathbf{R}_w^{**}}{\partial t^{**2}} \right) \cdot \delta \mathbf{R}_w^{**} \right] \sqrt{A_1} \mathrm{d}\zeta^{**} = 0 \tag{1.34}$$

where the traction on the wall (including fluid load and prescribed external pressure) is

$$\mathbf{f}^{**} = \rho U_0^2 (-p^*_{\text{ext}} + p^*)\mathbf{N} - \mu \left(\nabla \mathbf{u}^{**} + (\nabla \mathbf{u}^{**})^T \right) \cdot \mathbf{N}, \tag{1.35}$$

the wall curvature is

$$\kappa^{**} = \left(d^{(y)**}_{\zeta^{**}\zeta^{**}} \left(1 + d^{(x)**}_{\zeta^{**}} \right) - d^{(x)**}_{\zeta^{**}\zeta^{**}} d^{(y)**}_{\zeta^{**}} \right) / \Delta, \tag{1.36}$$

and

$$A_1 \equiv \frac{\partial \mathbf{r}_w^{**}}{\partial \zeta^{**}} \cdot \frac{\partial \mathbf{r}_w^{**}}{\partial \zeta^{**}} = 1, \quad A_2 \equiv \frac{\partial \mathbf{R}_w^{**}}{\partial \zeta^{**}} \cdot \frac{\partial \mathbf{R}_w^{**}}{\partial \zeta^{**}} = \Delta, \tag{1.37}$$

with the outer normal on the wall

$$\mathbf{N} = (-d_{\zeta^{**}}^{(y)^{**}}, 1 + d_{\zeta^{**}}^{(x)^{**}})^T / \Delta, \tag{1.38}$$

and

$$\Delta \equiv \sqrt{\left(1 + d_{\zeta^{**}}^{(x)^{**}}\right)^2 + \left(d_{\zeta^{**}}^{(y)^{**}}\right)^2}. \tag{1.39}$$

The first two terms in (1.34) represent the variation in the wall strain energy due to its extension and bending, respectively. The last two terms represent the virtual work done by the fluid traction $\mathbf{f}^{**}$ acting on the deformed wall and the wall inertia. Apart from the dynamical condition (1.35), fluid and solid interact via the no-slip and kinematic conditions

$$\mathbf{u}^{**} = \frac{\partial \mathbf{R}_w^{**}}{\partial t^{**}} \tag{1.40}$$

on the wall.

We nondimensionlize variables in the wall problem as

$$\begin{aligned} &(h_0^*, \zeta^*, \mathbf{r}_w^*, \mathbf{d}^*, \mathbf{R}_w^*) = (h_0^{**}, \zeta^{**}, \mathbf{r}_w^{**}, \mathbf{d}^{**}, \mathbf{R}_w^{**})/a, \quad \kappa^* = a\kappa^{**} \\ &(\sigma_0^*, \sigma^*, \mathbf{f}^*) = (\sigma_0^{**}, \sigma^{**}, \mathbf{f}^{**})/\rho U_0^2, \end{aligned} \tag{1.41}$$

with other quantities defined in (1.6). Thus the dimensionless form of (1.34), (1.35) and (1.40) are

$$\begin{aligned} \int_0^{L^*} \Bigg[&\left(\sigma_0^* + \frac{E}{\rho U_0^2}\gamma\right)\delta\gamma + \frac{1}{12}\frac{E}{\rho U_0^2}(h_0^*)^2 \kappa^* \delta\kappa^* \\ &- \left(\frac{\Delta}{h_0^*}\mathbf{f}^* - \frac{\rho_w}{\rho}\frac{\partial^2 \mathbf{R}_w^*}{\partial (t^*)^2}\right) \cdot \delta \mathbf{R}_w^* \Bigg] \mathrm{d}\zeta^* = 0, \end{aligned} \tag{1.42}$$

$$\mathbf{f}^* = (-p_{\mathrm{ext}}^* + p^*)\mathbf{N} - \frac{1}{Re}\left(\nabla \mathbf{u}^* + (\nabla \mathbf{u}^*)^T\right) \cdot \mathbf{N}, \tag{1.43}$$

$$\mathbf{u}^* = \frac{\partial \mathbf{R}_w^*}{\partial t^*}, \qquad \text{on the wall.} \tag{1.44}$$

Equation (1.42) shows that assuming $\sigma_0^* \sim E/(\rho U_0^2)$ the additional stress due to wall stretch ($\sim O(1/(L^*)^2)$) is small compared to pre-stress σ_0^* when $L^* \gg 1$; the variation of strain energy from bending is small compared to that from pre-stress when $h_0^* \ll L^*$ (except possibly in boundary layers, e.g. at the ends of the membrane); wall inertia is small compared to fluid load when $\rho_w h_0^* \ll \rho$. We ignore wall inertia in our two-dimensional numerical simulations. Equation (1.43) shows that at high Re, the load on the wall is dominated by the normal traction $(-p_{\text{ext}}^* + p^*)\mathbf{N}$. For wall deformations of small amplitude and long wavelength, material points on the wall will therefore move predominately in the vertical direction so that $\zeta^* \approx x^*$, $d^{(x)*} \approx 0$ and $d^{(y)*} \approx h^* - 1$. Then we have $\mathbf{R}_w^* = (x^*, h^*)^T$, $\gamma = (h_{x^*}^*)^2/2$ and $\mathbf{N} = (-h_{x^*}^*, 1)^T/\Delta$. From equation (1.44) we get $u^* = 0$ and $v^* = h_{t^*}^*$. Furthermore, if we neglect the additional wall stress, wall bending, wall inertia and the viscous stress in the fluid load, then equation (1.42) can be simplified to

$$\int_0^{L^*} \left[\sigma_0^* \delta\gamma - \left(\frac{1}{h_0^*}\right)(-p_{\text{ext}}^* + p^*)\mathbf{N} \cdot \delta\mathbf{R}_w^* \Delta \right] \mathrm{d}x^* = 0 \tag{1.45}$$

Substituting $\mathbf{R}_w^*$, γ and $\mathbf{N}$ into (1.45), we have

$$\int_0^{L^*} \left[\frac{T_0}{\rho U_0^2 a} h_{x^*}^* (\delta h^*)_{x^*} - (-p_{\text{ext}}^* + p^*)\delta h^* \right] \mathrm{d}x^* = 0. \tag{1.46}$$

Integrating by parts for the first term in (1.46), we obtain

$$\int_0^{L^*} \left[-\frac{T_0}{\rho U_0^2 a} h_{x^* x^*}^* - (-p_{\text{ext}}^* + p^*) \right] \delta h^* \mathrm{d}x^* = 0, \tag{1.47}$$

where we use the fact $\delta h^* = 0$ at $x^* = 0, L^*$. Finally, using same notation of T^* in (1.8), we recover a normal-stress condition for the fluid

$$p^* = p_{\text{ext}}^* - T^* h_{x^* x^*}^*, \tag{1.48}$$

which is consistent with (1.14).

1.4.3 Dimensionless wall equations

In the numerical simulation, all stress and tractions are non-dimensionalized on the beam's elastic modulus E, that is,

$$(\bar{\bar{\sigma}}_0, \bar{\bar{\sigma}}, \bar{\bar{\mathbf{f}}}) = (\sigma_0^{**}, \sigma^{**}, \mathbf{f}^{**})/E, \tag{1.49}$$

with other quantities defined in (1.6) and (1.41). Therefore, the dimensionless wall problem (1.42) and the dynamical condition (1.43) become

$$\int_0^{L^*} \left[(\bar{\bar{\sigma}}_0 + \gamma)\,\delta\gamma + \frac{(h_0^*)^2 \kappa^* \delta\kappa^*}{12} - \frac{\bar{\bar{\mathbf{f}}} \cdot \delta \mathbf{R}_w^* \Delta}{h_0^*} \right] \mathrm{d}\zeta^* = 0, \tag{1.50}$$

and

$$\bar{\bar{\mathbf{f}}} = \frac{\rho U_0^2}{E} \left((-p_{\mathrm{ext}}^* + p^*)\mathbf{I} - \frac{1}{Re} \left(\nabla \mathbf{u}^* + (\nabla \mathbf{u}^*)^T \right) \right) \cdot \mathbf{N}, \tag{1.51}$$

Here we ignore wall inertia in the numerical simulation.

We define $Q = \mu U_0/(Ea)$, here $\mu U_0/a$ is another fluid pressure scale. Therefore the parameter Q indicates the strength of the fluid-structure interaction. Then the fluid-structure interaction problem is characterised by seven dimensionless parameters

$$L_1^*, \quad L^*, \quad L_2^*, \quad h_0^*, \quad Q(\equiv \mu U_0/(Ea)), \quad Re(\equiv \rho a U_0/\mu), \quad T^*(\equiv T_0/(\rho U_0^2 a)). \tag{1.52}$$

The pre-stress required in (1.50) and the ratio of the inertial pressure to the incremental Young's modulus required in (1.51) are given by $\bar{\bar{\sigma}}_0 = ReQT^*/h_0^*$ and $\rho U_0^2/E = ReQ$, respectively.

1.5 Structure of the thesis

In this thesis we study the mechanism of onset of self-excited oscillations in flexible-channel flow with fixed upstream flux. Results are presented as follows.

In Chapter 2 we postulate that, in the one-dimensional fluid-membrane model described in §1.3, the collapsible part of the channel, the membrane, has similar length to the rigid segment of channel downstream of the membrane. Given the simplicity of this model, due to a number of assumptions, we are able to carefully examine the

stability of the uniform state of the model, investigating finite-amplitude evolution of solutions of the model. We unfold a degenerate bifurcation with two zero eigenvalues, a Takens–Bogdanov bifurcation, and construct amplitude equations describing the evolution of the system in the neighbourhood of this bifurcation point. In the framework of this model, we find that "mode-2" oscillations (i.e. membrane displacements with two extrema) can be driven by divergent instabilities of two non-uniform steady configurations of the membrane.

In Chapter 3 we consider the case in which the downstream rigid segment is much longer than the membrane. In this case the longer downstream segment influences the resulting oscillations of the system. Using a similar approach to that employed in Chapter 2, we perform a three-parameter unfolding of a degenerate bifurcation point having four zero eigenvalues and construct a fourth-order set of amplitude equations. Our analysis shows that the amplitude equations can describe oscillations invoked by instabilities promoted by a 1:1 resonant interaction between two modes. The amplitude equations also predict the existence of saturated sawtooth oscillations, which we reproduce in full Navier–Stokes simulations of the two-dimensional channel system.

In Chapter 4 we study the highly-collapsed solutions of the simplified one-dimensional model. We conjecture that these solutions are related to the emergence of large-amplitude slamming oscillations that have been found not only in our simplified one-dimensional model (§2.4) but also in a two-dimensional model (Stewart *et al.*, 2010*a*). Motivated by the work of Jensen (1998), we construct the leading-order approximation of the highly-collapsed solution using the method of matched asymptotic expansions. The linear stability analysis of the steady highly-collapsed solution reveals that they are very unstable, which allows the possibility that they are a precursor to slamming.

Finally, in Chapter 5 we summarise all results of this thesis and suggest some directions for future studies.

Chapter 2

Divergence-driven oscillations

In this chapter we study the one-dimensional model of flow in a flexible channel described in §1.3, with the rigid segment of the channel downstream of the flexible segment of the channel being of a length comparable to, or shorter than, the flexible segment itself. In the model an external linear pressure distribution is applied to the flexible channel wall such that the uniform Poiseuille flow is a steady solution of the model. We first consider the linear stability of the uniform state. Then we perform weakly nonlinear analysis in the nearly inviscid limit. We also numerically solve the partial differential equations governing the model. Finally we compare results from stability analysis with numerical simulations and explain our findings.

2.1 Model

The model we consider in this chapter is described by (1.26, 1.27). An equivalent model system (with pressure imposed upstream instead of flux) was tested against full Navier–Stokes simulations in Stewart *et al.* (2010*a*). While quantitative accuracy can be guaranteed only for sufficiently large $\mathscr{R}$, and for T neither too large (avoiding high-frequency motions) nor too small (avoiding large membrane gradients), the predictions for $\mathscr{R} = O(1)$ were shown to capture many important features of large-amplitude oscillations computed by two-dimensional Navier–Stokes simulations. We therefore pursue our analysis of (1.26, 1.27), remaining conscious of the model's potential limitations for small $\mathscr{R}$. In §2.2.2 below, we will vary the coefficient of the $(q^2/h)_x$ term in (1.26b) between 1 and 6/5, to assess the sensitivity of the model's predictions to the velocity profile assumption as mentioned in §1.3.3.

In the numerical results reported below, we set $L_2 = 1$ (unless specified otherwise) and then seek solutions of (1.26, 1.27) as functions of $\mathscr{R}$ and T. The effects of taking $L_2 \gg 1$ will be reported in next chapter. We first examine the linear stability of the uniform state $h = 1$, $q = 1$.

2.2 Linear stability of the uniform state

Setting $h = 1 + \mathrm{Re}(H(x)\mathrm{e}^{\sigma t})$, $q = 1 + \mathrm{Re}(Q(x)\mathrm{e}^{\sigma t})$, where H, Q and σ are complex, $|H(x)| \ll 1$, $|Q(x)| \ll 1$ and $\mathrm{Re}(\sigma)$ is a growth rate, we obtain from (1.26, 1.27) the linear eigenvalue problem

$$Q' = -\sigma H, \quad TH''' + \frac{6}{5}H' + 36\mathscr{R}H - \frac{12}{5}Q' - 12\mathscr{R}Q = \sigma Q, \tag{2.1a}$$

with boundary conditions

$$H(0) = 0, \quad Q(0) = 0, \tag{2.2a}$$

$$H(1) = 0, \quad TH''(1) + 12\mathscr{R}L_2Q(1) = -\sigma L_2 Q(1). \tag{2.2b}$$

We use a Chebyshev approximation to solve the eigenvalue problem (2.1, 2.2). Transforming the x-domain to $[-1,1]$, we expand $Q(x)$ and $H(x)$ in Chebyshev series with a vector of coefficients $\mathbf{a}$, substitute into (2.1, 2.2) and require the resulting system to be satisfied at Gauss–Lobatto collocation points. This yields a generalized matrix eigenvalue problem of form $\mathbf{Aa} = \sigma\mathbf{Ba}$, where $\mathbf{A}$ and $\mathbf{B}$ are square matrices. We denote the resulting eigenmodes as 'mode n' when $|H(x)|$ has n humps. We use this method to identify neutral curves (on which $\mathrm{Re}(\sigma) = 0$) in the $(T, \mathscr{R})$-plane, with the corresponding eigenmodes.

When $\mathscr{R} = 0$, the linearised equations (2.1, 2.2) admit simple solutions for which $\sigma = 0$, representing static inviscid eigenmodes. In this case $Q(x) = 0$ and H satisfies

$$TH'''(x) + \frac{6}{5}H'(x) = 0, \quad H(0) = 0, \quad H(1) = 0, \quad H''(1) = 0. \tag{2.3}$$

This eigenvalue problem has solutions

$$H(x) = \sin n\pi x, \quad T = T_{n0} = \frac{6}{5n^2\pi^2}, \quad (n = 1, 2, 3, \cdots). \tag{2.4}$$

Thus $T_{10} \approx 0.121585$, $T_{20} \approx 0.0303964$, etc. These asymptotes are analogous to the bifurcation points identified by Guneratne & Pedley (2006) in their study of the same system using interactive boundary layer theory; the present model has bifurcation points (2.4) for $T = O(1)$, whereas in Guneratne & Pedley's model they appear (in our notation) for $T = O(\mathscr{R}^{1/3})$, reflecting the failure of the present model to capture the structure of viscous boundary layers in steady flow. In compensation, however, the present model provides a much more tractable guide to possible unsteady behaviour.

2.2.1 Numerical results

Figure 2.1(a) maps out in (T, $\mathscr{R}$)-space two neutral curves, on each of which there exists a static eigenmode with $\sigma = 0$, and one neutral curve on which there exists an oscillatory eigenmode with $\mathrm{Re}(\sigma) = 0$. We label the static neutral curves for mode n as TC_n (we show below that the corresponding bifurcations are transcritical) and similarly label the oscillatory neutral curve as Hopf_n. We anticipate that additional neutral curves exist for smaller T. The curves TC_n asymptote to $T = T_{n0}$ as $\mathscr{R} \to 0$ (see (2.4)). For $T > T_{10}$, the uniform state is linearly stable for all $\mathscr{R}$. As T decreases across TC_1, mode 1 becomes unstable (with a real eigenvalue passing through zero). The neutrally stable eigenmode changes smoothly from mode 1 to mode 2 along the curve marked TC_1–TC_2 (i.e. the number of humps in $|H|$ increases from 1 to 2; the transition is indicated with a circle). As T decreases across TC_2, the static mode 2 eigenmode becomes stable, but the uniform state then becomes unstable to an oscillatory mode 2 eigenmode via a Hopf bifurcation as T decreases across Hopf_2. The frequency of the neutrally stable eigenmode falls to zero as $\mathscr{R} \to 0$, and the Hopf_2 curve approaches the limit $T \to T_{20}$ as $\mathscr{R} \to 0$. The mode 3 and 4 disturbances for smaller T are broadly similar although the Hopf_3 curve does not extend to zero $\mathscr{R}$. We found no evidence of a Hopf_1 neutral curve, consistent with previous studies of flux-driven systems (Liu *et al.*, 2012). It is notable that the neutrally stable oscillations change type continuously along the Hopf neutral curve (from modes 2 to 3 to 4); in contrast, studies of the linear stability of non-uniform states reveal the overlapping of distinct neutral curves (Jensen, 1990; Luo *et al.*, 2008).

Figures 2.1(b) and 2.2 show in greater detail the neutral curves in the neighbourhood of (T_{20}, 0) (together with asymptotic approximations, derived below) and the corresponding eigenvalue path. As seen in Figure 2.2, for $\mathscr{R} = 10^{-3}$ and $T = 0.031$, there exist two real eigenvalues, one positive and one negative. As T decreases to

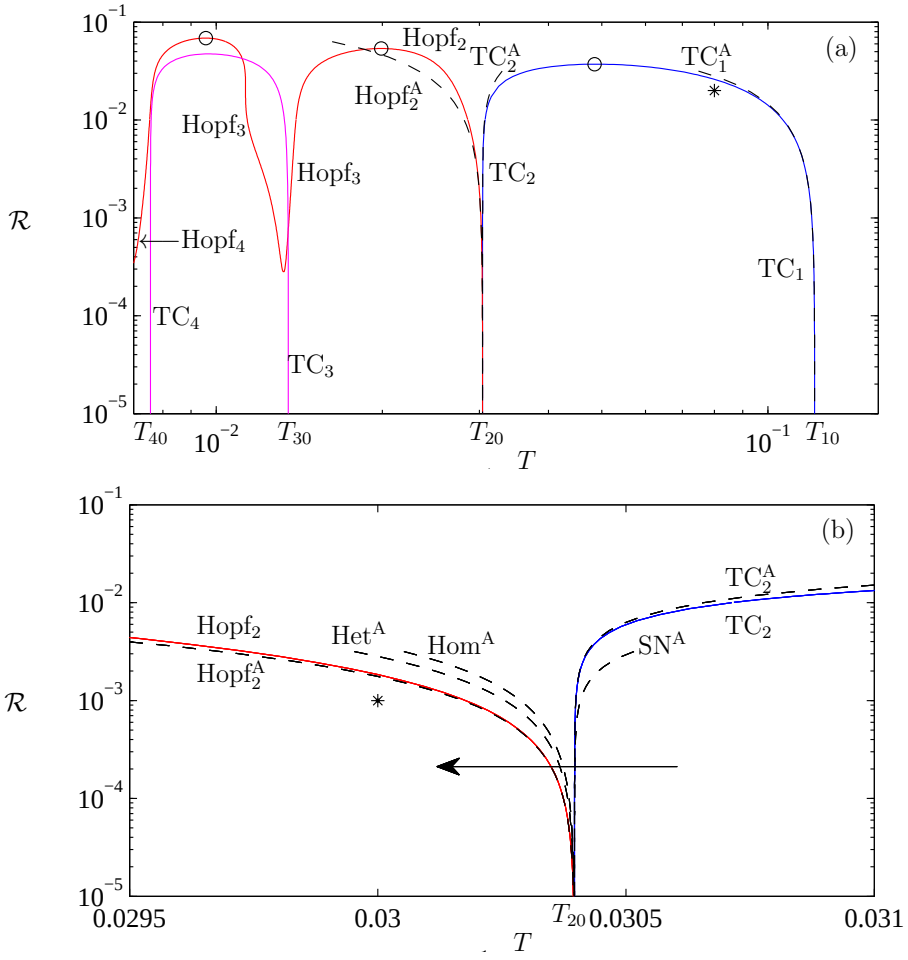

Figure 2.1: (a) Neutral curves in $(T, \mathscr{R})$-space (solid), showing transcritical (TC) and Hopf bifurcations for modes 1-4. Dashed lines show asymptotic approximations for $\mathscr{R} \ll 1$: (2.7) (labelled $\mathrm{TC}_1^{\mathrm{A}}$), (2.9) (labelled $\mathrm{TC}_2^{\mathrm{A}}$) and (2.12) (labelled $\mathrm{Hopf}_2^{\mathrm{A}}$). The uniform state is linearly stable for $(T, \mathscr{R})$ above the neutral curves. Circles on the neutral curves mark the points at which neutral oscillations change smoothly between modes 1, 2, 3 and 4. (b) Neutral curves in the neighbourhood of $(T_{20}, 0)$, showing in addition the heteroclinic bifurcation (2.22) (labelled $\mathrm{Het}^{\mathrm{A}}$), the homoclinic bifurcation (2.23) (labelled $\mathrm{Hom}^{\mathrm{A}}$) and the saddle-node bifurcation (2.18) (labelled SN^{A}). The arrow shows the path mapped out in Figure 2.2 below. Figures 2.5 and 2.7 below show PDE simulations conducted at the points marked with asterisks in (b) and (a) respectively.

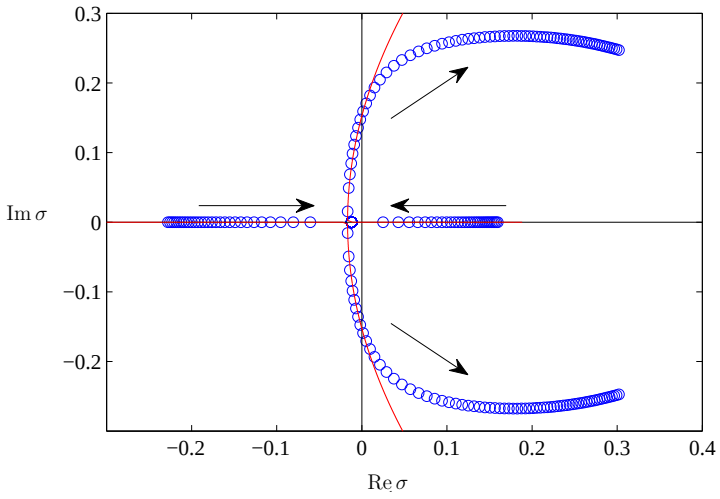

Figure 2.2: The eigenvalue path as T varies from 0.031 to 0.029 for $\mathscr{R} = 10^{-3}$. The numerical results are marked with circles and the solid lines show the asymptotic approximation (2.11). Arrows show decreasing T.

$T \approx T_{20} + 2025\mathscr{R}^2/8\pi^4$ (see (2.9) below), the positive eigenvalue falls to zero, which corresponds to crossing TC_2 in Figure 2.1(b). As T decreases further to approximately T_{20}, these two eigenvalues coalesce, becoming complex conjugates with negative real part. The real part of this conjugate pair then increases to zero as T decreases to $T \approx T_{20} - 175\mathscr{R}/8\pi^4$ (see (2.12) below), which corresponds to crossing Hopf_2 in Figure 2.1(b).

As suggested by Figure 2.2, the system has a double zero eigenvalue at $T = T_{20}$, $\mathscr{R} = 0$, making this a Takens–Bogdanov bifurcation point. Although the governing equations (1.26, 1.27) are likely to lose quantitative accuracy in this part of parameter space, it is an important organising centre of the dynamical system, justifying a more thorough analysis of the local dynamics near each end of the TC_n curves.

2.2.2 Linear stability in the nearly inviscid limit

We derive parametric expansions of the linear stability problem (2.1, 2.2) in the neighbourhood of the bifurcation points $\mathscr{R} = 0$, $T = T_{n0}$, where $Q_0 \equiv 0$ and $H_0 \equiv \sin n\pi x$

(see (2.4)) at leading order, using

$$Q(x) = Q_0(x) + \varepsilon Q_1(x) + \varepsilon^2 Q_2(x) + \varepsilon^3 Q_3(x) + \cdots, \tag{2.5a}$$

$$H(x) = H_0(x) + \varepsilon H_1(x) + \varepsilon^2 H_2(x) + \varepsilon^3 H_3(x) + \cdots, \tag{2.5b}$$

$$T = T_{n0} + \varepsilon T_{n1} + \varepsilon^2 T_{n2} + \varepsilon^3 T_{n3} + \cdots, \tag{2.5c}$$

$$\mathscr{R} = \varepsilon \mathscr{R}_1 + \varepsilon^2 \mathscr{R}_2 + \varepsilon^3 \mathscr{R}_3 + \cdots, \tag{2.5d}$$

$$\sigma = \varepsilon \sigma_1 + \varepsilon^2 \sigma_2 + \varepsilon^3 \sigma_3 + \cdots. \tag{2.5e}$$

Here $0 < \varepsilon \ll 1$ and the coefficients in (2.5) are assumed to be of order unity as $\varepsilon \to 0$; it is convenient to introduce ε in (2.5) as it enables us to capture different balances between parameters with a single expansion. Substituting (2.5) into (2.1, 2.2), a succession of boundary-value problems is recovered at increasing orders in ε. Solvability conditions at each order yield predictions for the dependence of σ on the governing parameters. Details are provided in Appendix 2.A; these predictions are all independent of L_2, which is assumed to remain $O(1)$ as $\varepsilon \to 0$.

For $\mathscr{R} \to 0$ and $T \to T_{10}$, (2.37) yields

$$\sigma = -\frac{5}{48}\left(144\mathscr{R} + \pi^4(T - T_{10})\right), \tag{2.6}$$

from which follows an approximation for the location of the neutral curve TC_1, on which $\sigma = 0$:

$$T = T_{10} - \frac{144\mathscr{R}}{\pi^4}. \tag{2.7}$$

Figure 2.1(a) confirms the accuracy of this prediction (see TC_1^A), which extends to $\mathscr{R} \lesssim 10^{-2}$.

We use (2.40, 2.42) to capture the behaviour of the dominant eigenvalues near $(T, \mathscr{R}) = (T_{20}, 0)$, noting that the first solvability condition demands that $T_{21} = 0$ in (2.5c). If we assume $T = T_{20} + \varepsilon^2 T_{22}$, $\mathscr{R} = \varepsilon \mathscr{R}_1$, $\sigma = \varepsilon \sigma_1$, so that $T - T_{20} = O(\mathscr{R}^2)$ as $\mathscr{R} \to 0$, (2.40) gives

$$4050\mathscr{R}^2 + 504\mathscr{R}\sigma + 15\sigma^2 + 16\pi^4(-T + T_{20}) = 0. \tag{2.8}$$

Thus neutral stability along TC_2^A emerges when

$$T = T_{20} + \frac{2025\mathscr{R}^2}{8\pi^4}, \tag{2.9}$$

which agrees well with numerical predictions of TC_2 in Figure 2.1(a,b). Alternatively, if we assume $\mathscr{R}_1 = 0$, so that $T = T_{20} + \varepsilon^2 T_{22}$, $\mathscr{R} = \varepsilon^2 \mathscr{R}_2$, $\sigma = \varepsilon\sigma_1 + \varepsilon^2\sigma_2$, and hence that $T - T_{20} = O(\mathscr{R})$ as $\mathscr{R} \to 0$, then (2.40) and (2.42) give

$$T_{22} = \frac{15\sigma_1^2}{16\pi^4}, \quad \mathscr{R}_2 = -\frac{18\sigma_1^2 + 25\sigma_2}{420}, \tag{2.10}$$

so

$$\sigma \approx -\frac{4}{375}\left(1575\mathscr{R} \pm 25\sqrt{15}\pi^2\sqrt{T - T_{20}} + 72\pi^4(T - T_{20})\right). \tag{2.11}$$

The eigenvalue path predicted by (2.11) agrees well with numerical predictions (Figure 2.2). From (2.11), we conclude that neutrally stable oscillations arise when

$$T = T_{20} - \frac{175\mathscr{R}}{8\pi^4}, \tag{2.12}$$

which is the asymptote of the Hopf_2 neutral curve (see Hopf_2^A in Figure 2.1(a,b)). In this case, the leading-order frequency of neutrally stable oscillations is given by

$$\sigma = \pm 4\pi^2 \mathrm{i}\sqrt{\frac{T_{20} - T}{15}}, \tag{2.13}$$

showing that neutrally stable oscillations are very slow as $(\mathscr{R}, T) \to (0+, T_{20}-)$.

Returning briefly to the discussion following (1.16), we now test the effect of varying the assumed axial velocity profile through changes in the coefficient α (say) of the convective inertia term in (1.26b); $\alpha = 6/5$ for Poiseuille flow. Repeating the analysis in Appendix 2.A, we find that the asymptotes TC_2^A and Hopf_2^A become

$$T = T_{20} + \frac{1215\mathscr{R}^2}{4\pi^4\alpha} \quad \text{and} \quad T = T_{20} - \frac{21\mathscr{R}(5\alpha - 1)}{4\pi^4\alpha} \tag{2.14}$$

as $\mathscr{R} \to 0$, $T \to T_{20}$, recovering (2.9) and (2.12) when $\alpha = 6/5$. Recall that variation between Poiseuille flow and a plug flow with boundary layers is accommodated by changing α between 6/5 and 1 and rescaling $\mathscr{R}$. It is evident from (2.14) that this does

not lead to any qualitative change in the arrangement of the neutral curves, suggesting that it is reasonable to retain $\alpha = 6/5$ in the following analysis.

Figure 2.2 demonstrates how the oscillatory instability arises from the coalescence of two static eigenmodes. This interaction becomes clearer when we extend our analysis to include finite-amplitude effects.

2.3 Weakly nonlinear stability in the nearly inviscid limit

Returning to the full problem (1.26, 1.27), we introduce three time scales $(\tau_0, \tau_1, \tau_2) = (\varepsilon t, \varepsilon^2 t, \varepsilon^3 t)$ and expand using

$$\phi(x;\tau_0,\tau_1,\tau_2) = 1 + \varepsilon\phi_0 + \varepsilon^2\phi_1 + \varepsilon^3\phi_2 + \varepsilon^4\phi_3 + \cdots, \tag{2.15a}$$

$$T = T_{n0} + \varepsilon T_{n1} + \varepsilon^2 T_{n2} + \varepsilon^3 T_{n3} + \cdots, \tag{2.15b}$$

$$\mathscr{R} = \varepsilon\mathscr{R}_1 + \varepsilon^2\mathscr{R}_2 + \varepsilon^3\mathscr{R}_3 + \cdots, \tag{2.15c}$$

where $\phi_i \equiv (q_i, h_i, \partial_x h_i, \partial_{xx} h_i)^{\mathrm{T}}$, $i = 0, 1, 2, 3$, etc.. After substituting (2.15) into (1.26, 1.27), a series of boundary-value problems emerges at increasing orders of ε. Details may be found in Appendix 2.B. The leading-order eigenmode is given by (2.38). Solvability conditions at each order yield amplitude equations describing the local dynamics.

2.3.1 Steady solutions near $(T_{20}, 0)$

If we assume $T = T_{20} + \varepsilon^2 T_{22}$ and $\mathscr{R} = \varepsilon\mathscr{R}_1$, so that $T - T_{20} = O(\mathscr{R}^2)$ as $\mathscr{R} \to 0$, we obtain from (2.47) the amplitude equation

$$A\left(9\pi A(\pi A - 180\mathscr{R}) - 10\left(2025\mathscr{R}^2 + 8\pi^4\left(T_{20} - T\right)\right)\right) - 2520\mathscr{R}A_t - 75A_{tt} = 0. \tag{2.16}$$

Steady solutions of (2.16) satisfy $A = 0$ or

$$9\pi^2 A^2 - 1620\pi\mathscr{R}A - 10\left(2025\mathscr{R}^2 - 8\pi^4(T - T_{20})\right) = 0, \tag{2.17}$$

which captures a saddle-node bifurcation at

$$T = T_{20} + \frac{9315\mathscr{R}^2}{8\pi^4}, \tag{2.18}$$

(shown as SN^A in Figure 2.1(b)) and a transcritical bifurcation (given by (2.9)), which are illustrated in Figure 2.3(a). Figure 2.3(a) shows that, for $\mathscr{R} = 10^{-3}$, the predicted solution branches (2.17) agree well with numerical solutions of the steady version of (1.26, 1.27) (setting $q = 1$, this is a nonlinear third-order problem for $h(x)$, with a first integral given by (2.68) below).

2.3.2 Oscillatory solutions near $(T_{20}, 0)$

If we assume $\mathscr{R}_1 = 0$ and $T = T_{20} + \varepsilon^2 T_{22}$, $\mathscr{R} = \varepsilon^2 \mathscr{R}_2$, so that $T - T_{20} = O(\mathscr{R})$ as $\mathscr{R} \to 0$, (2.47) gives

$$\partial_{\tau_0,\tau_0} A_0 = \frac{3}{25}\pi^2 A_0^3 + \frac{16}{15}\pi^4 A_0 T_{22}, \tag{2.19}$$

which is the analogue of (2.16) in the limit $\mathscr{R} \to 0$. Thus, to leading order with $T < T_{20}$ and the assumed balance of parameters, disturbances are governed by a Hamiltonian system, the phase portrait of which is illustrated in Figure 2.3(b). As Figure 2.3(a) indicates, for $T - T_{20} < 0$ the uniform state coexists with two unstable mode-2 solutions of opposite symmetry. To this level of approximation (which neglects viscous effects), the uniform state is neutrally stable but coexists with a family of periodic orbits. Slowly varying perturbations to (2.19) are captured by (2.50), which using (2.19) we can re-express as

$$\begin{aligned}\partial_{\tau_0,\tau_1} A_0 = &-\frac{21}{625}\pi^3 A_0^4 - \frac{2}{375}\pi A_0^2\left(2025\mathscr{R}_2 + 56\pi^4 T_{22}\right) + \frac{288}{625}\pi^2 A_0^2 \partial_{\tau_0} A_0 \\ &- \frac{12}{125}\left(175\mathscr{R}_2 + 8\pi^4 T_{22}\right)\partial_{\tau_0} A_0 + \frac{29}{50}\pi(\partial_{\tau_0} A_0)^2.\end{aligned} \tag{2.20}$$

If we define $A_0(\tau_0, \tau_1, \tau_2) = A_0(\tau_0, \varepsilon\tau_0, \varepsilon^2\tau_0) \equiv B(\tau)$, where $\tau = \tau_0$, then with error $O(\varepsilon^2)$ we can re-express (2.20) as

$$\begin{aligned}B_{\tau\tau} = &\frac{3}{25}\pi^2 B^3 + \frac{16}{15}\pi^4 B T_{22} + \frac{\varepsilon}{1875}\Big(-126\pi^3 B^4 - 20\pi B^2\left(2025\mathscr{R}_2 + 56\pi^4 T_{22}\right) \\ &+ 1728\pi^2 B^2 B_\tau - 360\left(175\mathscr{R}_2 + 8\pi^4 T_{22}\right)B_\tau + 2175\pi B_\tau^2\Big).\end{aligned} \tag{2.21}$$

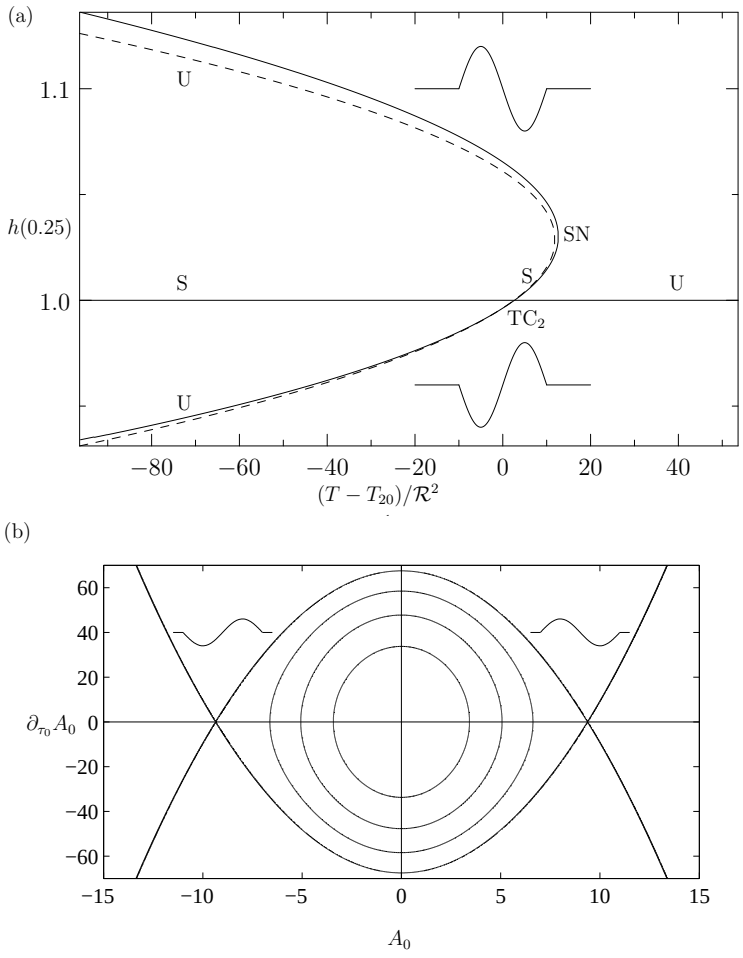

Figure 2.3: (a) Bifurcation diagram for $\mathscr{R} = 10^{-3}$, with $T - T_{20} = O(\mathscr{R}^2)$. The solid line denotes nonlinear steady solutions computed directly from (1.26, 1.27); the dashed line denotes asymptotic solutions from (2.17). Close to the transcritical bifurcation (TC_2) there is an exchange of stability between stable (S) and unstable (U) solution branches; there is a further change in stability at the saddle–node bifurcation (SN). Insets show the shape of the membrane near each non-uniform solution branch. (b) For $T - T_{20} = O(\mathscr{R})$ and $T < T_{20}$, the dynamics is approximately Hamiltonian with non-uniform states (illustrated by insets) represented by saddle points in the $(A_0, \partial_{\tau_0} A_0)$-phase plane. Here we illustrate heteroclinic and periodic orbits of (2.19) with $T_{22} = -1$, with Hamiltonian (2.53) satisfying $\mathscr{H} = \{16, 32, 48, 64\}\pi^6/27$.

In Appendix 2.C, we use a Mel'nikov analysis to show that (2.21) has a heteroclinic connection along

$$T = T_{20} - \frac{375\left(185\sqrt{6}-32\right)\mathscr{R}}{11552\pi^4}, \tag{2.22}$$

and a homoclinic connection along

$$T = T_{20} - \frac{2625\mathscr{R}}{248\pi^4}. \tag{2.23}$$

These asymptotes are plotted in Figure 2.1(b). The Mel'nikov analysis shows that, when including weak viscous effects, a limit cycle exists for T in the parameter range bounded by (2.12) and (2.23), when the uniform state is locally stable, implying that the Hopf bifurcation is subcritical. This can be confirmed by application of the Hopf bifurcation theorem (not shown).

2.3.3 Steady solutions near $(T_{10}, 0)$

In addition, near $\mathscr{R} \to 0$, $T = T_{10}$, from (2.44), solutions with steady amplitude $A = \varepsilon A_0$ satisfy

$$A(24\pi A + 5\left(144\mathscr{R} + \pi^4(T - T_{10})\right)) = 0, \tag{2.24}$$

which indicates $A = 0$ or

$$A = -\frac{5\left(144\mathscr{R} + \pi^4(T - T_{10})\right)}{24\pi}. \tag{2.25}$$

Hence we obtain the condition of a transcritical bifurcation, consistent with (2.7). In the neighbourhood of $(T, \mathscr{R}) = (T_{10}, \mathscr{R})$, a locally stable (unstable) inflated (collapsed) steady state exists for T less than (greater than) the value given in (2.7).

2.3.4 Overview

We summarise the behaviour revealed by this analysis in Figure 2.4. In Figure 2.4(a) we divide $(T, \mathscr{R})$-parameter space (see Figure 2.1(b)) near the intersection of the Hopf_2 and TC_2 curves into seven regions (I-VII); in each region, a distinct phase plane describes the local dynamics. The corresponding bifurcation diagram is given in Fig-

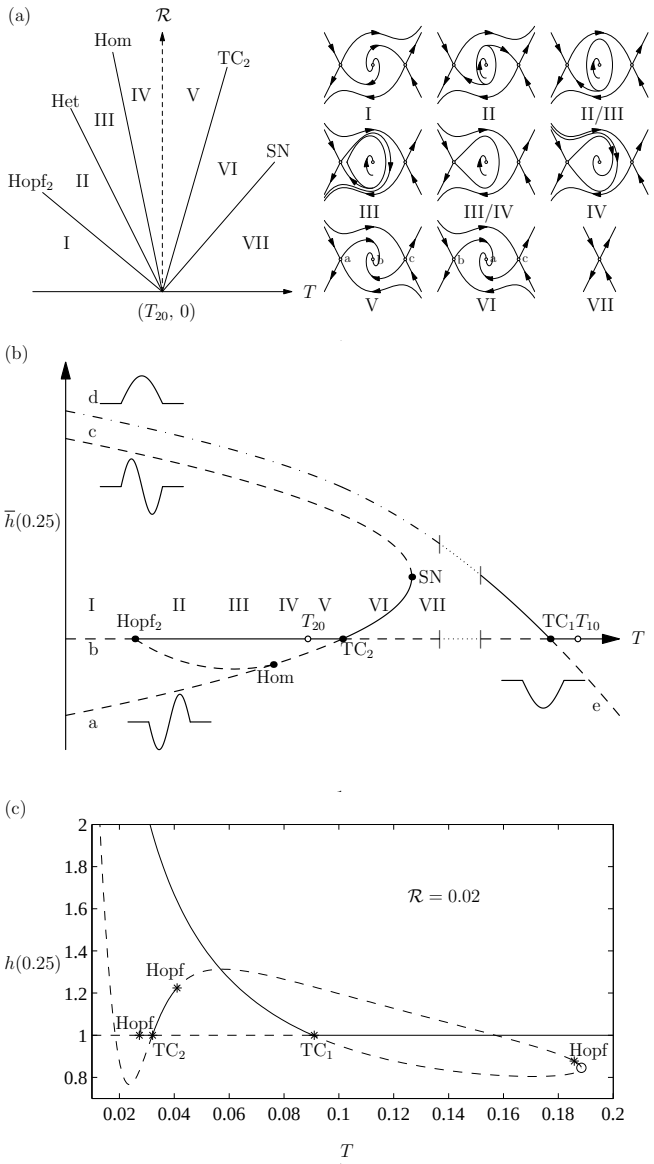

Figure 2.4: (a) shows how different phase portraits (labelled I–VII) arise in different regions of parameter space near $(T_{20}, 0)$, with bifurcation curves labelled as in Figure 2.1. (b) Schematic bifurcation diagram for $\mathscr{R} \to 0$. Solid (dashed) lines represent stable (unstable) steady solutions branches, with insets showing the corresponding membrane shapes; the unstable limit cycle between $Hopf_2$ and Hom is also dashed. Dotted lines indicate that T_{10} is far from T_{20}. The stability of the dot–dash line is not determined here. (c) Steady solution branches for $\mathscr{R} = 0.02$, computed from (1.26,1.27); unstable branches are shown dashed; the circle near $T = 0.19$ marks the transition between mode 1 and mode 2 solutions. A simulation at $T = 0.08$ is shown in Figure 2.7 below.

ure 2.4(b), encompassing the results near $(T_{10}, 0)$ and $(T_{20}, 0)$. In region I, the uniform state (b) is an unstable focus; small disturbances will oscillate and grow, moving first towards (and between) the two non-uniform steady solutions (saddle points labelled a and c in Figure 2.4(b)) before moving away to another region of phase space (this is addressed further in § 2.4 below); the inflated state that emerges from TC_1 is one possible attractor. In regions II and III, the uniform state becomes a stable focus and an unstable limit cycle emerges, so that sufficiently large disturbances to the uniform state will again oscillate and grow. There is a heteroclinic connection between two non-uniform steady solutions (labelled a and c; see (2.22)) at the boundary between regions II and III. The amplitude of the periodic solution increases as T increases up to the value given by (2.23), marking the boundary between regions III and IV. In region IV, the unstable limit cycle disappears, but the uniform state is still unstable to sufficiently large perturbations. In region V small perturbations to the uniform state decay monotonically. Crossing into region VI, there is an exchange of stability between the uniform steady solution (b) and the non-uniform steady solution (a) via a transcritical bifurcation given by (2.9). As T increases to the value given by (2.18), at the boundary between regions VI and VII, two non-uniform steady solutions (one stable (a) and the other unstable (c)) coalesce via a saddle-node bifurcation. In region VII, the uniform state is unstable but the inflated solution branch emerging from TC_1 remains a possible attractor. As T increases across (2.7) (TC_1), there is a further exchange of stability, with restabilisation of the uniform state (b).

The steady solution structure shown in Figures 2.3(a) and 2.4(b) resembles surprisingly closely that reported by Guneratne & Pedley (2006) (see their Figures 6(d,e) and 11, which also show a saddle-node bifurcation of mode 2); their results demonstrate how the solution branches reconnect when the pressure external to the membrane is altered, breaking the symmetry of the uniform state. Figure 2.4(c), which shows nonlinear steady solutions of (1.26, 1.27), shows how a small increase in $\mathscr{R}$ — in this case to 0.02 — also has a profound effect on the solution structure, with the mode-2 saddle node being replaced by a branch connecting mode-2 solutions emerging from TC_2 to mode 1 solutions emerging from TC_1. A linear stability analysis of the non-uniform states, using a Chebyshev method similar to that outlined in §2.2, reveals two additional Hopf bifurcations of non-uniform mode-2 states. Thus in general the system is characterised by the existence of multiple non-uniform states, some of which are unstable. In Chapter 4, we will revisit the turning point near $T = 0.2$ in Figure 2.4(c).

Our analysis for $\mathscr{R} \ll 1$ demonstrates the essential role of the two saddle points

(a,c) in driving an oscillatory instability of the uniform state. Each saddle point has an unstable manifold, representing a divergent instability. Growing oscillations are predicted to pass close to each saddle point, being swept away by the local divergent instability, before being drawn towards the opposite saddle. Thus monotonic instability (an inviscid mechanism relying on the Bernoulli effect, which may be thought of as a form of static divergence), coupled to the symmetry of two nearby steady states, is sufficient to generate neutrally stable oscillations (Figure 2.3(b)); viscous effects perturb this Hamiltonian structure to determine whether trajectories approach the uniform state or diverge away from the saddle points (Figure 2.4(a)). This mechanism does not depend on the conditions in the upstream and downstream rigid tubes (being independent of L_2, provided L_2 is not too large), requiring only that upstream flux and downstream pressure are prescribed.

Further evidence of the difference of this mechanism from the 'sloshing' mode (described by Stewart *et al.* (2009, 2010*a*)) comes from an analysis of the energy budget (Appendix 2.D), which shows that the dominant contributions are the work done by the upstream pressure and viscous dissipation; the rate of kinetic energy transport is not significant.

2.4 Large amplitude solutions

Figure 2.5 shows a representative simulation of (1.26, 1.27), obtained using methods described in Appendix 2.E, for parameter values as indicated by the asterisk in Figure 2.1(b). This falls into region I (see Figure 2.4(a)): as predicted, the amplitude of a small mode-2 disturbance grows until the trajectory encounters a nearby steady solution (a saddle point, illustrated in the phase portrait in Figure 2.4(a)), before diverging rapidly (for $t > 200$ in this example) with h and h_t at $x = 0.25$ both growing in magnitude and the flux at $x = 1$ falling. At small amplitudes, the period of the growing oscillation lies close to the predicted value (for $T = 0.03$, $\mathscr{R} = 10^{-3}$) of 30.96 (see (2.13b)).

Figure 2.6 shows the corresponding spatial structure of this mode 2 solution as it grows rapidly in amplitude. The channel width falls rapidly to zero close to $x = 0.9$, with a very large curvature gradient appearing (Figure 2.6(b)). This appears to be the early stage of a slamming event, as identified previously in simulations with fixed upstream pressure (Stewart *et al.*, 2010*a*) using both a one-dimensional model and two-

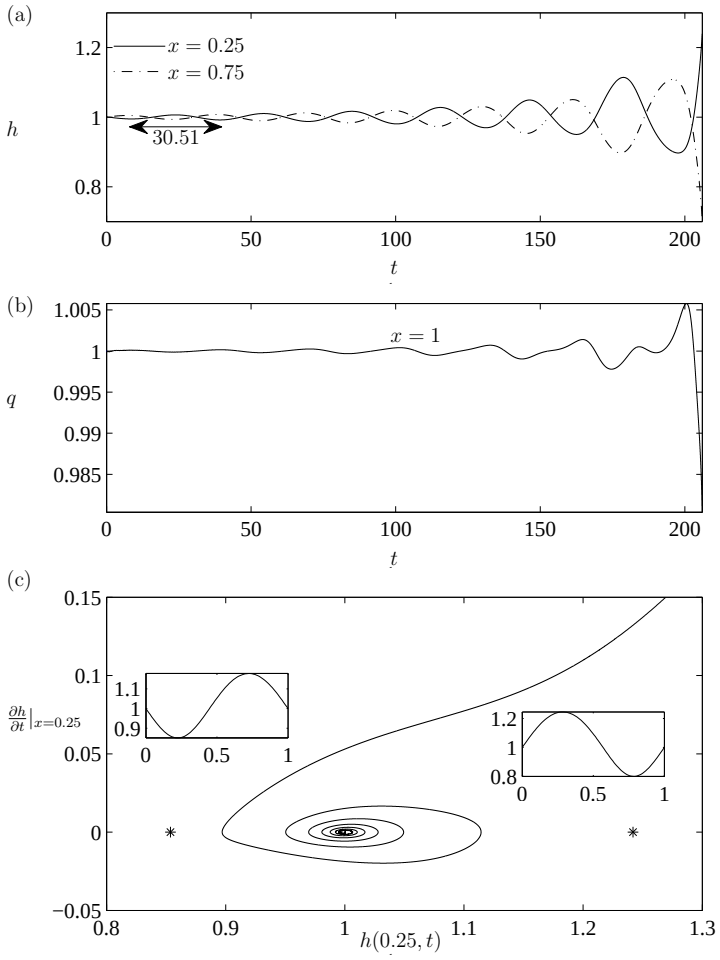

Figure 2.5: (a) h at $x = 0.25$ (solid) and $x = 0.75$ (dashed) plotted versus time for $T = 0.03$ and $\mathscr{R} = 10^{-3}$; the out-of-phase motion is characteristic of a mode 2 oscillation. (b) The corresponding downstream flux $q(1,t)$. (c) A phase portrait that mimics that shown in Figure 2.4(a); asterisks mark the location of steady solutions, shown as insets.

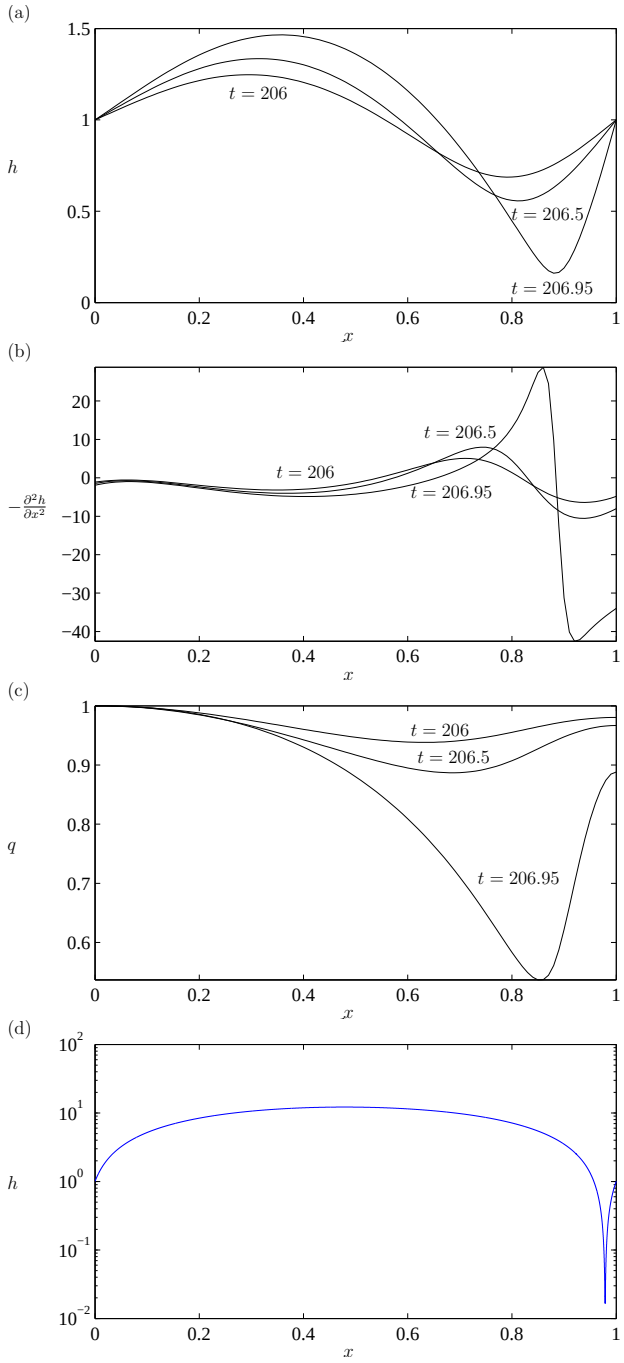

Figure 2.6: Spatial structure of the solution shown in Figure 2.5 at three time instants near a slamming event, showing (a) $h(x,t)$, (b) membrane curvature (a proxy for pressure) $-h_{xx}(x,t)$ and (c) flux $q(x,t)$. (d) The large-amplitude steady mode 2 solution that exists for $\mathscr{R} = 10^{-3}$, $T = 0.03$, showing a sharp constriction (note logarithmic scale).

dimensional simulations. Because T is small in this example, large spatio-temporal gradients arise that prevented us from obtaining reliable simulations for larger times using either a spectral or a finite-difference method.

To illustrate the difficulty, one can analyse the structure of large-amplitude steady solutions arising for $\mathscr{R} \ll 1$ and $\mathscr{R}T \lesssim 1$ (see for example Figure 2.6(d)). These have a sharp symmetric constriction at a location $x = 1-\delta$, where $0 < \delta < 1$ and typically $\delta \ll 1$. The membrane shape is determined by a balance between the terms $\frac{6}{5}(1/h)_x$ and Thh_{xxx} in (1.26b) with $q = 1$. Either side of the constriction, the pressure is approximately uniform ($h_{xxx} = 0$ to leading order), making the membrane shape quadratic upstream and linear downstream (given that $h_{xx}(1) = 0$ in steady flow). These shapes meet at either side of the constriction with slope $1/\delta$; the upstream region inflates to height $O(1/\delta)$. The height and length scales in the constriction ($\mathscr{H} \ll 1$ and $\mathscr{X} \ll 1$ respectively) satisfy the scalings $T\mathscr{H}^3 \sim \mathscr{X}^2$ and $\mathscr{H}/\mathscr{X} \sim \delta$, implying that $\mathscr{H} \sim \delta^2/T$ and $\mathscr{X} \sim \delta^3/T$. The energy budget (2.68) determines the pressure drop across the constriction and hence the curvature of the upstream region: viscous dissipation is dominated by the constriction, so that $T/\delta \sim \mathscr{R}\mathscr{X}/\mathscr{H}^3$, giving $\delta \sim (\mathscr{R}T)^{1/2}$, $\mathscr{H} \sim \mathscr{R}$ and $\mathscr{X} \sim (\mathscr{R}^3T)^{1/2}$. Thus for the parameters used in Figure 2.6, the minimum channel width of the steady solution has magnitude of order $\mathscr{R} = 10^{-3}$ (we find $h_{\min} = 0.0167$ in Figure 2.6(d)) and the constriction length is of magnitude of order $(\mathscr{R}^3T)^{1/2} = 5\times 10^{-6}$, exceeding the resolution capability of our unsteady code.

The long-term dynamics of the system can be illustrated more clearly at larger values of $\mathscr{R}$ and T. Figure 2.7 and the accompanying video (see Supplementary Information) show a simulation with $\mathscr{R} = 0.02$, $T = 0.08$, where linear theory predicts that the uniform state shows a divergent instability (see the asterisk in Figure 2.1(a)); for these parameter values there also exists a linearly stable inflated mode-1 steady solution and a mode-2 steady solution that is unstable to an oscillatory instability (Figure 2.4(c)). In this case, divergent instability of the uniform state (in $0 \le t \lesssim 50$) drives the solution first towards what appears to be a slamming event, and thereafter into sustained oscillations. These include intermittent events (reminiscent of slamming) in which the membrane comes into near contact with the opposite wall of the channel. Following each slam, waves propagate up and down the channel, falling in amplitude until the solution lies close to the mode-2 steady solution, before a growing oscillation drives the system towards another slamming event.

This example demonstrates how an initial divergent instability can result in oscillations, suggesting a potential outcome of the divergent instabilities described in two-

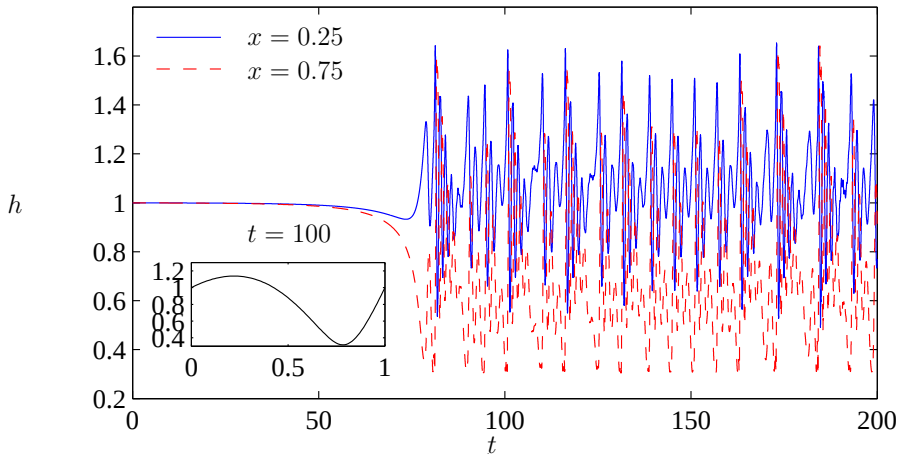

Figure 2.7: A simulation at $\mathscr{R} = 0.02$, $T = 0.08$, showing how an initially monotonic instability leads to repetitive slamming. The insert shows the membrane shape h versus x at $t = 100$. (In color.)

dimensional models of this system (Guneratne & Pedley, 2006; Kudenatti *et al.*, 2012; Pihler-Puzović & Pedley, 2013) (although the instability reported in these models may be driven by ill-posedness rather than the mechanism reported here). It also emphasises the role that intermittent slamming may play in sustaining large-amplitude oscillations.

2.5 Discussion

In this chapter we have examined the origin of a low-frequency mode-2 instability appearing in a flexible channel flow, using the spatially one-dimensional model (1.26, 1.27) described in §1.3. We have assumed that the length of the downstream rigid segment is comparable to that of the membrane. The application of a linear external pressure gradient that ensures that (1.26, 1.27) have a uniform state as a steady solution for any choice of T, $\mathscr{R}$ and L_2. This state typically coexists with non-uniform steady solutions. In the present problem there is an exchange of stability between the uniform and non-uniform steady states at transcritical bifurcations (Figure 2.1), in a manner that is qualitatively similar to the predictions of Guneratne & Pedley (2006). Depending on parameter values, the different steady states can exhibit a monotonic instability driven by an inviscid Bernoulli mechanism, whereby at fixed flux, a constriction increases flow speed locally, decreases pressure and promotes further constriction.

Linear stability analysis of the uniform base state shows that, close to an organ-

ising centre in parameter space ($T \to T_{20}$, $\mathscr{R} \to 0$, $L_2 = O(1)$), a mode-2 oscillation emerges from an interaction between two steady modes (Figure 2.2). Asymptotic predictions of neutral curves emerging from this codimension-2 bifurcation point remain reasonably accurate to moderate values of $\mathscr{R}$ (Figure 2.1), at least for the value of L_2 investigated here (in next chapter we find that for larger L_2 the mode-2 instability mechanism described here will still apply sufficiently close to $(T,\mathscr{R}) = (T_{20},0)$, where oscillations are of very low frequency). In the nearly inviscid limit, the system can exhibit an approximately Hamiltonian structure; from among a family of periodic orbits (Figure 2.3(b)), one orbit is preserved in the presence of weak viscous effects. This orbit turns out to be unstable and the associated Hopf bifurcation to be subcritical. The consequence is that oscillations of sufficiently large amplitude grow until they encounter a nearby saddle point, before diverging to larger amplitude, a prediction confirmed by simulations (Figure 2.6). An energy analysis (Appendix 2.D) shows that the energy source for growing oscillations is work done by the upstream pressure. During each cycle of oscillation, the system is driven towards, and then away from, a nearby non-uniform steady solution (Figures 2.4(a), 2.6), allowing the monotonic Bernoulli-driven instability of nearby steady states to drive the growth of oscillations. We also numerically solved our one-dimensional model to illustrate the resulting large-amplitude behaviour. As also reported for flows driven by fixed upstream pressure (Stewart *et al.*, 2010*a*), what appears to be transient 'slamming' motion can arise during which the channel briefly becomes almost fully constricted, before recovering rapidly (Figures 2.6, 2.7).

In conclusion, in this chapter we have shown how the growth of a mode-2 oscillation in a flux-driven flexible-channel flow can be driven by divergent instability of two unstable steady states. This mechanism is distinct from the sloshing instability reported in the corresponding pressure-driven system. Larger amplitude motions can be dominated by intermittent slamming events. In the next chapter we examine the effect of increasing the length of the downstream rigid segment (which provides additional coupling between pressure and flux at the downstream end of the channel, and hence further potential routes to self-excited oscillation) and use numerical simulations of a two-dimensional model (to resolve viscous and unsteady effects more accurately) to test the robustness of our predictions.

2.A Parametric expansions

We apply the expansion (2.5) to (2.1, 2.2). At $O(1)$, the system may be represented compactly as

$$\mathscr{F}\phi_0 = 0, \quad \mathscr{B}_0\phi_0(0) = 0, \quad \mathscr{B}_1\phi_0(1) = 0, \tag{2.26a}$$

where $\phi_i \equiv (Q_i, H_i, H_i', H_i'')^{\mathrm{T}}$, $i = 0,1,2,3,$ etc. Here $\mathscr{F} = \mathscr{F}_{\mathrm{D}}\partial_x + \mathscr{F}_{\mathrm{L}}$ is a linear differential operator, where

$$\mathscr{F}_{\mathrm{D}} = \begin{pmatrix} 1 & 0 & 0 & 0 \\ 0 & 1 & 0 & 0 \\ 0 & 0 & 1 & 0 \\ -12 & 0 & 0 & 5T_{n0} \end{pmatrix}, \qquad \mathscr{F}_{\mathrm{L}} = \begin{pmatrix} 0 & 0 & 0 & 0 \\ 0 & 0 & -1 & 0 \\ 0 & 0 & 0 & -1 \\ 0 & 0 & 6 & 0 \end{pmatrix}; \tag{2.27}$$

the boundary condition operators are

$$\mathscr{B}_0 = \begin{pmatrix} 1 & 0 & 0 & 0 \\ 0 & 1 & 0 & 0 \\ 0 & 0 & 0 & 0 \\ 0 & 0 & 0 & 0 \end{pmatrix}, \qquad \mathscr{B}_1 = \begin{pmatrix} 0 & 0 & 0 & 0 \\ 0 & 1 & 0 & 0 \\ 0 & 0 & 0 & 0 \\ 0 & 0 & 0 & T_{n0} \end{pmatrix}. \tag{2.28}$$

At $O(\varepsilon^j)$, $j = 1,2,3$, the system of equations may be expressed as

$$\mathscr{F}\phi_j = \mathscr{N}_j, \quad \mathscr{B}_0\phi_j(0) = 0, \quad \mathscr{B}_1\phi_j(1) = \mathscr{G}_j. \tag{2.29a}$$

where

$$\mathscr{N}_j = \begin{pmatrix} N_{j1} \\ 0 \\ 0 \\ N_{j2} \end{pmatrix}, \qquad \mathscr{G}_j = \begin{pmatrix} 0 \\ 0 \\ 0 \\ G_j(1) \end{pmatrix}, \tag{2.30}$$

and

$$N_{11} = -\sigma_1 H_0, \tag{2.31a}$$
$$N_{12} = -180\mathscr{R}_1 H_0 + 60\mathscr{R}_1 Q_0 + 5\sigma_1 Q_0 - 5T_1 H_0''', \tag{2.31b}$$
$$N_{21} = -\sigma_2 H_0 - \sigma_1 H_1, \tag{2.31c}$$
$$N_{22} = -180\mathscr{R}_2 H_0 - 180\mathscr{R}_1 H_1 + 60\mathscr{R}_2 Q_0 + 5\sigma_2 Q_0 + 60\mathscr{R}_1 Q_1 + 5\sigma_1 Q_1 - 5T_2 H_0''' - 5T_1 H_1''', \tag{2.31d}$$
$$N_{31} = -\sigma_3 H_0 - \sigma_2 H_1 - \sigma_1 H_2, \tag{2.31e}$$
$$N_{32} = -180\mathscr{R}_3 H_0 - 180\mathscr{R}_2 H_1 - 180\mathscr{R}_1 H_2 + 60\mathscr{R}_3 Q_0 + 5\sigma_3 Q_0 + 60\mathscr{R}_2 Q_1 + 5\sigma_2 Q_1 + 60\mathscr{R}_1 Q_2 + 5\sigma_1 Q_2 - 5T_3 H_0''' - 5T_2 H_1''' - 5T_1 H_2''', \tag{2.31f}$$
$$G_1 = -T_1 H_0'' - 12L_2 Q_0 \mathscr{R}_1 - L_2 Q_0 \sigma_1, \tag{2.31g}$$
$$G_2 = -T_2 H_0'' - T_1 H_1'' - 12L_2 Q_0 \mathscr{R}_2 - 12L_2 Q_1 \mathscr{R}_1 - L_2 Q_0 \sigma_2 - L_2 Q_1 \sigma_1, \tag{2.31h}$$
$$G_3 = -T_3 H_0'' - T_2 H_1'' - T_1 H_2'' - 12L_2 Q_0 \mathscr{R}_3 - 12L_2 Q_1 \mathscr{R}_2 - 12L_2 Q_2 \mathscr{R}_1 - L_2 Q_0 \sigma_3 - L_2 Q_1 \sigma_2 - L_2 Q_2 \sigma_1. \tag{2.31i}$$

The inhomogeneous terms in (2.29) must satisfy a solvability condition. To find this, we introduce the inner product

$$\langle \phi, \psi \rangle \equiv \int_0^1 \phi \psi \mathrm{d}x \tag{2.32}$$

and then calculate the eigensolution $\phi^\dagger$ of the adjoint operator $\mathscr{F}^\dagger = -\mathscr{F}_{\mathrm{D}}^T \partial_x + \mathscr{F}_{\mathrm{L}}^T$. This is defined so that the boundary condition terms vanish in

$$\langle (\phi^\dagger)^T, \mathscr{F}\phi_0 \rangle = \langle \phi_0^T, \mathscr{F}^\dagger \phi^\dagger \rangle + (\phi^\dagger)^T \mathscr{F}_{\mathrm{D}} \phi_0 |_0^1, \tag{2.33}$$

which requires that the corresponding adjoint boundary condition operators are

$$\mathscr{B}_0^\dagger = \begin{pmatrix} 0 & 0 & 0 & 0 \\ 0 & 0 & 0 & 0 \\ 0 & 0 & 1 & 0 \\ 0 & 0 & 0 & 1 \end{pmatrix}, \qquad \mathscr{B}_1^\dagger = \begin{pmatrix} 1 & 0 & 0 & -12 \\ 0 & 0 & 0 & 0 \\ 0 & 0 & 1 & 0 \\ 0 & 0 & 0 & 0 \end{pmatrix}. \tag{2.34}$$

After calculating $\phi^\dagger$, the solvability condition on (2.29) is

$$\langle (\phi^\dagger)^T, N_j \rangle = (\phi^\dagger)^T \mathscr{F}_{\mathrm{D}} \phi_j |_0^1, \tag{2.35}$$

for the problem at $O(\varepsilon^j)$. The solution of the homogeneous problem, the solvability conditions and the solutions of the inhomogeneous problems can be secured in succession.

For $n = 1$, we obtain

$$\phi_0 = A_0 \begin{pmatrix} 0 \\ \sin \pi x \\ \pi \cos \pi x \\ -\pi^2 \sin \pi x \end{pmatrix}, \quad \phi^\dagger = C \begin{pmatrix} 2(1-\cos \pi x) \\ 1 \\ -(\sin \pi x)/\pi \\ (1-\cos 2\pi x)/6 \end{pmatrix}, \tag{2.36}$$

where A_0 and C are constants; we assume $C = 1$ without loss of generality. Given ϕ_0 and $\phi^\dagger$, the first solvability condition (using (2.31a, 2.31b) in (2.35)) is

$$T_{11} = -\frac{48\,(15\mathscr{R}_1 + \sigma_1)}{5\pi^4}, \tag{2.37}$$

from which we obtain (2.6) and (2.7).

For $n = 2$, the leading-order eigenmode becomes

$$\phi_0 = A_0 \begin{pmatrix} 0 \\ \sin 2\pi x \\ 2\pi \cos 2\pi x \\ -4\pi^2 \sin 2\pi x \end{pmatrix}, \quad \phi^\dagger = C \begin{pmatrix} 2(1-\cos 2\pi x) \\ 1 \\ -(\sin 2\pi x)/(2\pi) \\ (1-\cos 2\pi x)/6 \end{pmatrix}. \tag{2.38}$$

Given ϕ_0 and $\phi^\dagger$, the first solvability condition (using (2.31a, 2.31b) in (2.35)) is $T_{21} = 0$. This condition admits the solution of (2.29) at $O(\varepsilon)$

$$\phi_1 = A_0 \begin{pmatrix} -(\sigma_1/\pi)\sin^2 \pi x \\ (\cos 2\pi x + \pi x \sin 2\pi x - 1)(15\mathscr{R}_1 + \sigma_1)/\pi \\ (2\pi x \cos 2\pi x - \sin 2\pi x)(15\mathscr{R}_1 + \sigma_1) \\ -4\pi^2 x \sin 2\pi x (15\mathscr{R}_1 + \sigma_1) \end{pmatrix}. \tag{2.39}$$

At $O(\varepsilon^2)$, using (2.31c, 2.31d) in (2.35), we obtain second solvability condition as

$$T_{22} = \frac{3\left(1350\mathscr{R}_1^2 + 168\mathscr{R}_1\sigma_1 + 5\sigma_1^2\right)}{16\pi^4} \tag{2.40}$$

and the solution of (2.29) at $O(\varepsilon^2)$, $\phi_2 = A_0\left(\phi_{21}, \phi_{22}, \phi_{23}, \phi_{24}\right)^{\mathrm{T}}$, where

$$\phi_{21} = \frac{(2\pi x(\cos 2\pi x + 2) - 3\sin 2\pi x)\sigma_1\left(15\mathscr{R}_1 + \sigma_1\right) - 4\pi\sin^2(\pi x)\sigma_2}{4\pi^2}, \tag{2.41a}$$

$$\begin{aligned}\phi_{22} = {} & \frac{\sin\pi x}{24\pi^2}(4\pi\sin\pi x(2700(2x-3)\mathscr{R}_1^2 + 60(11x-17)\sigma_1\mathscr{R}_1 + (19x-31)\sigma_1^2 \\ & - 12\left(15\mathscr{R}_2 + \sigma_2\right)) + 3\cos\pi x(450\left(4\pi^2x^2+13\right)\mathscr{R}_1^2 + 240\left(\pi^2x^2+3\right)\sigma_1\mathscr{R}_1 \\ & + 21\sigma_1^2 + 8\pi^2x\left(x\sigma_1^2 + 30\mathscr{R}_2 + 2\sigma_2\right))),\end{aligned} \tag{2.41b}$$

$$\begin{aligned}\phi_{23} = {} & \frac{1}{24\pi}(1350\left(\left(4\pi^2x^2+5\right)\cos 2\pi x + 4\pi(5x-6)\sin 2\pi x + 8\right)\mathscr{R}_1^2 \\ & + 120\left(\left(6\pi^2x^2+7\right)\cos 2\pi x + 2\pi(14x-17)\sin 2\pi x + 11\right)\sigma_1\mathscr{R}_1 \\ & + 38\sigma_1^2 - 4\pi\sin 2\pi x\left((31-25x)\sigma_1^2 + 90\mathscr{R}_2 + 6\sigma_2\right) \\ & + \cos 2\pi x\left(25\sigma_1^2 + 24\pi^2x\left(x\sigma_1^2 + 30\mathscr{R}_2 + 2\sigma_2\right)\right)),\end{aligned} \tag{2.41c}$$

$$\begin{aligned}\phi_{24} = {} & \frac{1}{3}\pi(x-1)\cos 2\pi x\left(8100\mathscr{R}_1^2 + 1020\sigma_1\mathscr{R}_1 + 31\sigma_1^2\right) \\ & - \frac{1}{12}\sin 2\pi x(1350\left(4\pi^2x^2-5\right)\mathscr{R}_1^2 + 120\left(6\pi^2x^2-7\right)\sigma_1\mathscr{R}_1 - 25\sigma_1^2 \\ & + 24\pi^2x\left(x\sigma_1^2 + 30\mathscr{R}_2 + 2\sigma_2\right)).\end{aligned} \tag{2.41d}$$

Using (2.41), we can deduce the third solvability condition, using (2.31e, 2.31f) in (2.35), at $O(\varepsilon^3)$, which is

$$\begin{aligned}T_{23} = {} & \frac{3}{40\pi^4}(12150R_1^2\sigma_1 + 30R_1\left(225R_2 + 27\sigma_1^2 + 14\sigma_2\right) + \sigma_1\left(420R_2 + 18\sigma_1^2 + 25\sigma_2\right) \\ & + 60750R_1^3).\end{aligned} \tag{2.42}$$

Equations (2.40, 2.42) yield predictions for the locations of the neutral curves TC_2 and Hopf_2.

2.B Weakly nonlinear analysis

We apply the expansion (2.15) to (1.26, 1.27), writing $\phi(x;\tau_0,\tau_1,\tau_2) = \phi(x)$ in shorthand below.

At $O(1)$, we recover the uniform solution $h = q = 1$. At following order, the linear problem is the form (2.26), and the linear differential operators and the boundary conditions operators are as defined in (2.27, 2.28). At $O(\varepsilon^j)$, $j = 1,2,3$, the systems of equations are expressed as (2.29), where $\mathscr{N}_j$ and $\mathscr{G}_j$ are defined as in (2.30), but now

$$N_{11} = -\partial_{\tau_1} h_0, \tag{2.43a}$$

$$\begin{aligned} N_{12} = &-180\mathscr{R}_1 h_0 + 12\partial_x q_0 h_0 - 15T_{n0}\partial_{x,x,x} h_0 h_0 + 60\mathscr{R}_1 q_0 + 5\partial_{\tau_0} q_0 - 12 q_0 \partial_x h_0 \\ &+ 12 q_0 \partial_x q_0 - 5T_{n1}\partial_{x,x,x} h_0, \end{aligned} \tag{2.43b}$$

$$N_{21} = -\partial_{\tau_1} h_0 - \partial_{\tau_0} h_1, \tag{2.43c}$$

$$\begin{aligned} N_{22} = &-180\mathscr{R}_1 h_0^2 - 15T_{n0}\partial_{x,x,x} h_0 h_0^2 - 180\mathscr{R}_2 h_0 + 10\partial_{\tau_0} q_0 h_0 + 12 q_0 \partial_x q_0 h_0 \\ &+ 12\partial_x q_1 h_0 - 15T_{n1}\partial_{x,x,x} h_0 h_0 - 15T_{n0}\partial_{x,x,x} h_1 h_0 - 180\mathscr{R}_1 h_1 + 60\mathscr{R}_2 q_0 \\ &+ 60\mathscr{R}_1 q_1 + 5\partial_{\tau_1} q_0 + 5\partial_{\tau_0} q_1 - 6q_0^2 \partial_x h_0 - 12 q_1 \partial_x h_0 - 12 q_0 \partial_x h_1 + 12 h_1 \partial_x q_0 \\ &+ 12 q_1 \partial_x q_0 + 12 q_0 \partial_x q_1 - 5T_{n2}\partial_{x,x,x} h_0 - 15T_{n0} h_1 \partial_{x,x,x} h_0 - 5T_{n1}\partial_{x,x,x} h_1, \end{aligned} \tag{2.43d}$$

$$N_{31} = -\partial_{\tau_2} h_0 - \partial_{\tau_1} h_1 - \partial_{\tau_0} h_2, \tag{2.43e}$$

$$\begin{aligned} N_{32} = &-60\mathscr{R}_1 h_0^3 - 5T_{n0}\partial_{x,x,x} h_0 h_0^3 - 180\mathscr{R}_2 h_0^2 + 5\partial_{\tau_0} q_0 h_0^2 - 15T_{n1}\partial_{x,x,x} h_0 h_0^2 \\ &- 15T_{n0}\partial_{x,x,x} h_1 h_0^2 - 180\mathscr{R}_3 h_0 - 360\mathscr{R}_1 h_1 h_0 + 10\partial_{\tau_1} q_0 h_0 + 10\partial_{\tau_0} q_1 h_0 \\ &+ 12 q_1 \partial_x q_0 h_0 + 12 q_0 \partial_x q_1 h_0 + 12\partial_x q_2 h_0 - 15T_{n2}\partial_{x,x,x} h_0 h_0 - 30T_{n0} h_1 \partial_{x,x,x} h_0 h_0 \\ &- 15T_{n1}\partial_{x,x,x} h_1 h_0 - 15T_{n0}\partial_{x,x,x} h_2 h_0 - 180\mathscr{R}_2 h_1 - 180\mathscr{R}_1 h_2 + 60\mathscr{R}_3 q_0 + 60\mathscr{R}_2 q_1 \\ &+ 60\mathscr{R}_1 q_2 + 5\partial_{\tau_2} q_0 + 5\partial_{\tau_1} q_1 + 10 h_1 \partial_{\tau_0} q_0 + 5\partial_{\tau_0} q_2 - 12 q_0 q_1 \partial_x h_0 - 12 q_2 \partial_x h_0 \\ &- 6q_0^2 \partial_x h_1 - 12 q_1 \partial_x h_1 - 12 q_0 \partial_x h_2 + 12 h_2 \partial_x q_0 + 12 h_1 q_0 \partial_x q_0 + 12 q_2 \partial_x q_0 \\ &+ 12 h_1 \partial_x q_1 + 12 q_1 \partial_x q_1 + 12 q_0 \partial_x q_2 - 5T_{n3}\partial_{x,x,x} h_0 - 15T_{n1} h_1 \partial_{x,x,x} h_0 \\ &- 15T_{n0} h_2 \partial_{x,x,x} h_0 - 5T_{n2}\partial_{x,x,x} h_1 - 15T_{n0} h_1 \partial_{x,x,x} h_1 - 5T_{n1}\partial_{x,x,x} h_2, \end{aligned} \tag{2.43f}$$

$$G_1 = -T_{n1}\partial_{x,x} h_0 - L_2 \partial_{\tau_0} q_0 - 12 L_2 \mathscr{R}_1 q_0, \tag{2.43g}$$

$$\begin{aligned} G_2 = &-T_{n2}\partial_{x,x} h_0 - T_{n1}\partial_{x,x} h_1 - L_2\partial_{\tau_1} q_0 - L_2\partial_{\tau_0} q_1 - 12 L_2 \mathscr{R}_2 q_0 - 12 L_2 \mathscr{R}_1 q_1, \end{aligned} \tag{2.43h}$$

$$\begin{aligned} G_3 = &-T_{n3}\partial_{x,x} h_0 - T_{n2}\partial_{x,x} h_1 - T_{n1}\partial_{x,x} h_2 - L_2\partial_{\tau_2} q_0 - L_2\partial_{\tau_1} q_1 - L_2\partial_{\tau_0} q_2 \\ &- 12 L_2 \mathscr{R}_3 q_0 - 12 L_2 \mathscr{R}_2 q_1 - 12 L_2 \mathscr{R}_1 q_2. \end{aligned} \tag{2.43i}$$

Once again we impose the solvability condition (2.35) and solve the corresponding boundary-value problem at each order.

For $n=1$, we obtain (2.36) with $A_0 = A_0(\tau_0,\tau_1,\tau_2)$ and the solvability condition

$$T_{11}A_0 = -\frac{24\left(2\partial_{\tau_0}A_0 + 30\mathscr{R}_1 A_0 + \pi A_0^2\right)}{5\pi^4}. \tag{2.44}$$

This yields (2.24).

For $n=2$, we obtain (2.38) with $A_0 = A_0(\tau_0,\tau_1,\tau_2)$ and solvability condition $T_{21} = 0$. The analogue of (2.39), now including nonlinear terms, is

$$q_1 = -\frac{\sin^2\pi x\,\partial_{\tau_0}A_0}{\pi}, \tag{2.45}$$

$$\begin{aligned} h_1 = {} & \frac{2\sin\pi x}{\pi}(\pi A_0^2\sin^3\pi x + 15A_0(\pi x\cos\pi x - \sin\pi x)\mathscr{R}_1 \\ & + (\pi x\cos\pi x - \sin\pi x)\partial_{\tau_0}A_0) \end{aligned} \tag{2.46}$$

and the second solvability condition (the analogue of (2.40)) is

$$T_{22}A_0 = -\frac{3}{80\pi^4}\left(3\pi^2A_0^3 - 540\pi A_0^2\mathscr{R}_1 - 6750A_0\mathscr{R}_1^2 - 840\mathscr{R}_1\partial_{\tau_0}A_0 - 25\partial_{\tau_0,\tau_0}A_0\right). \tag{2.47}$$

The second-order solution, including amplitude-dependent terms, is

$$\begin{aligned} q_2 = {} & -\frac{1}{8\pi^2}(8\pi\partial_{\tau_1}A_0\sin^2\pi x + \pi A_0(12\pi x - 8\sin 2\pi x + \sin 4\pi x)\partial_{\tau_0}A_0 \\ & - 2(2\pi x(\cos 2\pi x + 2) - 3\sin 2\pi x)\left(15\mathscr{R}_1\partial_{\tau_0}A_0 + \partial_{\tau_0,\tau_0}A_0\right)), \end{aligned} \tag{2.48}$$

$$\begin{aligned} h_2 = {} & \frac{1}{96\pi^2}(\sin\pi x(3\pi^2(25(\cos\pi x + \cos 3\pi x) - 7\cos 5\pi x)A_0^3 \\ & - 360\pi(-15\cos\pi x + 5\cos 3\pi x + 4\pi(2\cos 2\pi x x - 3x + 1)\sin\pi x)\mathscr{R}_1A_0^2 \\ & + 12(225\left(\left(8\pi^2x^2 + 37\right)\cos\pi x + 16\pi(2x-3)\sin\pi x\right)\mathscr{R}_1^2 + 240\pi(\pi x\cos\pi x - \sin\pi x)\mathscr{R}_2 \\ & - 8\pi(\cos\pi x + \cos 3\pi x + \pi(x-4)\sin\pi x + \pi x\sin(3\pi x))\partial_{\tau_0}A_0)A_0 \\ & + 4(48\pi(\pi x\cos\pi x - \sin\pi x)\partial_{\tau_1}A_0 \\ & + 30(\left(24\pi^2x^2 + 103\right)\cos\pi x + 8\pi(11x - 17)\sin\pi x)\mathscr{R}_1\partial_{\tau_0}A_0 \\ & + \left(\left(24\pi^2x^2 + 91\right)\cos\pi x + 4\pi(19x - 31)\sin\pi x\right)\partial_{\tau_0,\tau_0}A_0))), \end{aligned} \tag{2.49}$$

which generalises (2.41). The third solvability condition (extending (2.42)) becomes

$$\begin{aligned}T_{23}A_0^2 = \frac{3}{160\pi^4}&(90\pi^2A_0^4\mathscr{R}_1 + 6\pi A_0^3\left(180\left(25\mathscr{R}_1^2+\mathscr{R}_2\right)-13\pi\partial_{\tau_0}A_0\right)\\ &-5\partial_{\tau_0}A_0\left(168\mathscr{R}_1\partial_{\tau_0}A_0+5\partial_{\tau_0,\tau_0}A_0\right)\\ &+4A_0^2\left(15\mathscr{R}_1\left(450\left(9\mathscr{R}_1^2+\mathscr{R}_2\right)+41\pi\partial_{\tau_0}A_0\right)+7\pi\partial_{\tau_0,\tau_0}A_0\right)\\ &+A_0(48600\mathscr{R}_1^2\partial_{\tau_0}A_0+1680\mathscr{R}_2\partial_{\tau_0}A_0-58\pi\partial_{\tau_0}A_0^2+100\partial_{\tau_0,\tau_1}A_0\\ &+240\mathscr{R}_1\left(7\partial_{\tau_1}A_0+17\partial_{\tau_0,\tau_0}A_0\right)+97\partial_{\tau_0,\tau_0,\tau_0}A_0)).\end{aligned} \tag{2.50}$$

2.C Mel'nikov analysis

To analyse (2.21), we set $\lambda = -T_{22}$, and consider $\lambda > 0$. Equation (2.21) can be rewritten as $(X_\tau, Y_\tau) = (Y, f(X) + \varepsilon g(X,Y))$ where $X = B$, $Y = B_\tau$ and

$$f = \frac{3}{25}\pi^2X^3 - \frac{16}{15}\pi^4\lambda X, \tag{2.51}$$

$$\begin{aligned}g = \frac{1}{1875}\Big(&-126\pi^3X^4 - 20\pi X^2\left(2025\mathscr{R}_2 - 56\pi^4\lambda\right) + 1728\pi^2X^2Y\\ &-360\left(175\mathscr{R}_2 - 8\pi^4\lambda\right)Y + 2175\pi Y^2\Big).\end{aligned} \tag{2.52}$$

The unperturbed system, $(X_\tau, Y_\tau) = (Y, f(X))$ is Hamiltonian with $X_\tau = \mathscr{H}_Y$, $Y_\tau = -\mathscr{H}_X$ and Hamiltonian

$$\mathscr{H} = \frac{Y^2}{2} - \frac{3\pi^2X^4}{100} + \frac{8\pi^4\lambda X^2}{15}. \tag{2.53}$$

It has a centre at $(X,Y) = (0,0)$ and saddle points at $(X,Y) = (\pm\frac{4\sqrt{5\lambda}\pi}{3}, 0)$.

We use Mel'nikov theory to investigate the dynamics of the perturbed Hamiltonian system (2.21) because it gives a algebraic method to measure difference between orbit in unperturbed system and its perturbed counterpart. We expand about a solution of the unperturbed system using $X = X^0 + \varepsilon X^1$, $Y = Y^0 + \varepsilon Y^1$, where $X_\tau^0 = Y^0$, $Y_\tau^0 = f(X^0)$. Then $X_\tau^1 = Y^1$ and $Y_\tau^1 = f'(X^0)X^1 + g(X^0, Y^0)$. The tangent to the unperturbed solution is $(Y^0, f(X^0))$, and its normal is therefore $(-f(X^0), Y^0)$. The distance between the unperturbed and perturbed solution is given by the function

$$D = ((-f(X^0), Y^0)) \cdot (X^1, Y^1) = -f(X^0)X^1 + Y^0Y^1 \tag{2.54}$$

Now

$$\begin{aligned} D_\tau &= -f'(X^0)X^0_\tau X^1 - f(X^0)X^1_\tau + Y^0_\tau Y^1 + Y^0 Y^1_\tau \\ &= -f'(X^0)Y^0 X^1 - f(X^0)Y^1 + f(X^0)Y^1 + Y^0(f'(X^0)X^1 + g(X^0,Y^0)) \\ &= Y^0 g(X^0,Y^0). \end{aligned} \tag{2.55}$$

Thus the Mel'nikov function (Guckenheimer & Holmes, 1983) $M = \int^\tau Y^0 g(X^0,Y^0)\mathrm{d}\tau$ can be used to identify closed orbits in the perturbed system.

A pair of heteroclinic orbits $(X^0_\pm(\tau), Y^0_\pm(\tau))$ (see Figure 2.3(b)) lie along

$$\frac{Y^2}{2} - \frac{3\pi^2 X^4}{100} + \frac{8\pi^4\lambda X^2}{15} = \frac{64\pi^6\lambda^2}{27}. \tag{2.56}$$

Thus we have

$$Y^0_\pm(X^0_\pm) = \pm\frac{\pi\sqrt{6400\pi^4\lambda^2 - 1440\pi^2\lambda(X^0_\pm)^2 + 81(X^0_\pm)^4}}{15\sqrt{6}}, \tag{2.57}$$

for $X^0_\pm$ between $\pm 4\sqrt{5\lambda}/\pi$.

On the upper orbit, we use the Mel'nikov function

$$\begin{aligned} M^+ &= \int_{-\infty}^{\infty} Y^0_+(\tau) g(X^0_+(\tau), Y^0_+(\tau))\mathrm{d}\tau = \int_{-\frac{4\sqrt{5\lambda}\pi}{3}}^{\frac{4\sqrt{5\lambda}\pi}{3}} g(X^0_+, Y^0_+(X^0_+))\mathrm{d}X^0_+ \\ &= \frac{512\pi^4\lambda^{3/2}\left(16\left(60+31\sqrt{6}\right)\pi^4\lambda - 375\left(45+14\sqrt{6}\right)\mathscr{R}_2\right)}{10125\sqrt{5}}. \end{aligned} \tag{2.58}$$

The condition $M^+ = 0$ implies that the upper heteroclinic orbit is preserved under the perturbation, which yields a heteroclinic connection along (2.22) for sufficiently small ε. No heteroclinic connection exists for the lower orbit for $\lambda > 0$, but for later reference we define the corresponding Melnikov function as

$$M^- = \frac{512\pi^4\lambda^{3/2}\left(16\left(-60+31\sqrt{6}\right)\pi^4\lambda + 375\left(45-14\sqrt{6}\right)\mathscr{R}_2\right)}{10125\sqrt{5}}. \tag{2.59}$$

Second, the unperturbed system possesses a family of concentric periodic orbits

$(X^{\mathscr{H}}(\tau), Y^{\mathscr{H}}(\tau))$ (see Figure 2.3(b)) lying on

$$\frac{Y^2}{2} - \frac{3\pi^2 X^4}{100} + \frac{8\pi^4 \lambda X^2}{15} = \mathscr{H}, \tag{2.60}$$

where $0 < \mathscr{H} < 64\pi^6\lambda^2/27$. Then we have

$$Y_{\pm}^{\mathscr{H}}(X) = \pm\sqrt{2}\sqrt{\mathscr{H} + \frac{3\pi^2 X^4}{100} - \frac{8}{15}\pi^4 X^2 \lambda}. \tag{2.61}$$

We introduce a subharmonic Mel'nikov function (Guckenheimer & Holmes, 1983), defined as

$$\begin{aligned} M^{\mathscr{H}} &= \int_0^{T^{\mathscr{H}}} Y^{\mathscr{H}}(\tau) g(X^{\mathscr{H}}(\tau), Y^{\mathscr{H}}(\tau)) \mathrm{d}\tau \\ &= \int_{X_1}^{X_2} g(X^{\mathscr{H}}, Y_+^{\mathscr{H}}(X^{\mathscr{H}})) \mathrm{d}X^{\mathscr{H}} + \int_{X_2}^{X_1} g(X^{\mathscr{H}}, Y_-^{\mathscr{H}}(X^{\mathscr{H}})) \mathrm{d}X^{\mathscr{H}}, \end{aligned} \tag{2.62}$$

where $T^{\mathscr{H}}$ is the period, X_1 and X_2 ($X_1 < X_2$) are the intersection of the periodic orbit and X axis, to determine the condition of each periodic orbit being preserved under perturbation, that is $M^{\mathscr{H}} = 0$.

Two limits of these periodic orbits are of interest. First, the orbits collapse onto the equilibrium point $(0,0)$ as $\mathscr{H} \to 0$, which means $\lim_{\mathscr{H}\to 0} M^{\mathscr{H}} = 0$ gives a critical condition for the existence of a periodic orbit in the perturbed system, i.e. a Hopf bifurcation. For small $\mathscr{H}$, we have

$$X_{1,2} = \pm\frac{1}{2\pi^2}\sqrt{\frac{15\mathscr{H}}{2\lambda}} + O(\mathscr{H}^{3/2}), \tag{2.63}$$

$$g(X, Y_{\pm}^{\mathscr{H}}(X)) = \pm\frac{24}{125}\sqrt{2\mathscr{H}}\left(8\pi^4\lambda - 175\mathscr{R}_2\right) + \frac{58\mathscr{H}\pi}{25} + O(\mathscr{H}^{3/2}, X^2). \tag{2.64}$$

Then, the subharmonic Mel'nikov function becomes

$$M^{\mathscr{H}} = \frac{48}{25\pi^2}\sqrt{\frac{3}{5\lambda}}\mathscr{H}\left(8\pi^4\lambda - 175\mathscr{R}_2\right). \tag{2.65}$$

Hence the condition for the Hopf bifurcation is consistent with (2.12).

Second, we obtain the heteroclinic orbits (2.57) as $\mathscr{H} \to 64\pi^6\lambda^2/27$, which means $\lim_{\mathscr{H}\to 64\pi^6\lambda^2/27} M^{\mathscr{H}} = 0$ is a condition for the existence of a periodic orbit with infinite period, i.e. a homoclinic orbit, in the perturbed system. We obtain (using (2.58,

2.59))

$$\lim_{\mathscr{H}\to 64\pi^6\lambda^2/27} M^{\mathscr{H}} = M^+ + M^-, \tag{2.66}$$

so a homoclinic bifurcation emerges along (2.23).

2.D Energy Budget

For the steady flow, $q = 1$ and $h = h(x)$, thus (1.33) is simplified as

$$\mathscr{K} = 0, \tag{2.67a}$$
$$\mathscr{F} = 0, \tag{2.67b}$$
$$\mathscr{P} = \frac{6}{5}\left(12\mathscr{R}(L_2+1) - Th_{xx}(0)\right), \tag{2.67c}$$
$$\mathscr{E} = 0, \tag{2.67d}$$
$$\mathscr{D} = \frac{72\mathscr{R}}{5}\left(\int_0^1 \frac{1}{h^3}\mathrm{d}x + L_2\right). \tag{2.67e}$$

The energy balance (1.32) then implies

$$12\mathscr{R}\int_0^1 \left(1 - \frac{1}{h^3}\right)\mathrm{d}x = Th_{xx}(0), \tag{2.68}$$

representing a balance between viscous dissipation and the rate of working of upstream pressure forces.

Here we define the time average of a quantity g over a period of oscillation $\mathscr{T}_1$ as

$$\overline{g} = \frac{1}{\mathscr{T}_1}\int_t^{t+\mathscr{T}_1} g\,\mathrm{d}t'. \tag{2.69}$$

For the special case $g = f_t$, where f is periodic with period $\mathscr{T}_1$, it follows that $\overline{g} = 0$. Thus, averaging each component of the energy budget (1.32) over one period of oscillation, we obtain

$$\overline{\mathscr{K}} = 0, \tag{2.70a}$$
$$\overline{\mathscr{F}} = \overline{\frac{18}{25}(1-q(1,t)^3)} = \frac{18}{25}(1-\overline{q(1,t)^3}), \tag{2.70b}$$

$$\overline{\mathscr{P}} = \overline{\frac{6}{5}p(0,t)} = \frac{6}{5}\left(12\mathscr{R}(L_2+1) - T\overline{h_{xx}(0,t)}\right), \tag{2.70c}$$

$$\begin{aligned}
\overline{\mathscr{E}} &= \overline{\frac{6}{5}\int_0^1 h_t p\,\mathrm{d}x}, \\
&= \overline{\frac{6}{5}\int_0^1 h_t\left(12\mathscr{R}(L_2+1-x) - Th_{xx}\right)\mathrm{d}x}, \\
&= \overline{\frac{6}{5}\int_0^1 h_t\left(12\mathscr{R}(L_2+1-x)\right)\mathrm{d}x - \frac{6}{5}\int_0^1 Th_t h_{xx}\mathrm{d}x}, \\
&= \overline{\frac{6}{5}\left(\int_0^1 h\left(12\mathscr{R}(L_2+1-x)\right)\mathrm{d}x\right)_t - \frac{6T}{5}\left(h_x h_t|_0^1 - \int_0^1 h_x h_{xt}\mathrm{d}x\right)}, \\
&= \overline{\frac{6}{5}\left(\int_0^1 h\left(12\mathscr{R}(L_2+1-x)\right)\mathrm{d}x\right)_t + \frac{6T}{10}\left(\int_0^1 h_x^2\mathrm{d}x\right)_t}, \\
&= 0,
\end{aligned} \tag{2.70d}$$

$$\begin{aligned}
\overline{\mathscr{D}} &= \overline{\frac{72\mathscr{R}}{5}\left(\int_0^1 \frac{q^2}{h^3}\mathrm{d}x + q(1,t)^2 L_2\right) + \frac{3}{25}\int_0^1 \frac{q^2 q_x}{h^2}\mathrm{d}x}, \\
&= \frac{72\mathscr{R}}{5}\left(\int_0^1 \overline{\frac{q^2}{h^3}}\mathrm{d}x + \overline{q(1,t)^2}L_2\right) + \frac{3}{25}\int_0^1 \overline{\frac{q^2 q_x}{h^2}}\mathrm{d}x \equiv \overline{\mathscr{D}_1} + \overline{\mathscr{D}_2}.
\end{aligned} \tag{2.70e}$$

Thus, the energy budget becomes

$$\overline{\mathscr{F}} + \overline{\mathscr{P}} = \overline{\mathscr{D}_1} + \overline{\mathscr{D}_2}. \tag{2.71}$$

For small-amplitude oscillations, expressed by q_i and h_i, $i = 1,2,\ldots$ as given in Appendix 2.B, the time-averaged energies (2.70) take the form

$$\overline{\mathscr{F}} = O(\varepsilon^5), \quad \overline{\mathscr{D}_2} = O(\varepsilon^5), \tag{2.72}$$

$$\overline{\mathscr{P}} = \overline{\mathscr{D}_1} = \frac{72}{5}(1+L_2)\mathscr{R}_2\varepsilon^2 + \frac{54}{5}\overline{A_0^2}\mathscr{R}_2\varepsilon^4 + O(\varepsilon^5), \tag{2.73}$$

confirming a dominant balance between work done by the upstream pressure and viscous dissipation.

2.E Numerical method

To investigate the evolution of small disturbances, we require numerical solutions of (1.26, 1.27) with given initial conditions. For time derivatives, we use a first-order semi-implicit time-stepping scheme; we use an implicit representation only for the

highest spatial derivatives in each equation. Denoting $[\cdot]_{t=t_k} \equiv [\cdot]^k$, the time-discretized governing equations are

$$\frac{h^{k+1}-h^k}{\Delta t} + [q_x]^{k+1} = 0, \tag{2.74}$$

$$\frac{q^{k+1}-q^k}{\Delta t} + \left[\frac{6}{5}\left(\frac{q^2}{h}\right)_x\right]^k = Th^k [h_{xxx}]^{k+1} + 12\mathscr{R}\left[\left(h-\frac{q}{h^2}\right)\right]^k. \tag{2.75}$$

For spatial derivatives, we use a spectral method. To apply a Chebyshev approximation, we use a coordinate transform $\hat{x} = 2x-1$ to rescale the flow domain ($0 \le x \le 1$) to the numerical domain ($-1 \le \hat{x} \le 1$). We expand h and q at timestep $k+1$ as a series of l Chebyshev polynomials of the first kind in the form

$$h(\hat{x}) \approx \sum_{l=0}^{n} a_l T_l(\hat{x}), \quad q(\hat{x}) \approx \sum_{l=0}^{n} b_l T_l(\hat{x}) \tag{2.76}$$

where a_l and b_l are undetermined numerical coefficients. Then the spatial derivatives can be expressed in terms of derivatives of Chebyshev polynomials and the undetermined numerical coefficients. The approximated solution is represented by its value at the Gauss–Lobatto points $\hat{x}_i = \cos i\pi/n$ for $i = 0,1,\ldots,n$. Denoting $[\cdot]_{\hat{x}=\hat{x}_i,t=t_k} \equiv [\cdot]_i^k$, the discretized governing equations and boundary conditions are, for $1 \le i \le n-1$,

$$h_i^{k+1} + 2[q_{\hat{x}}]_i^{k+1}\Delta t = h_i^k, \tag{2.77}$$

$$q_i^{k+1} - 8Th_i^k [h_{\hat{x}\hat{x}\hat{x}}]_i^{k+1}\Delta t = q_i^k - \left[\frac{12}{5}\left(\frac{q^2}{h}\right)_{\hat{x}}\right]_i^k \Delta t + 12\mathscr{R}\left[\left(h-\frac{q}{h^2}\right)\right]_i^k \Delta t, \tag{2.78}$$

$$h_0^{k+1} = 1, \tag{2.79}$$

$$h_n^{k+1} = 1, \tag{2.80}$$

$$q_0^{k+1} + \frac{4\mathscr{L}T[h_{\hat{x}\hat{x}}]_0^{k+1}\Delta t}{1+12\mathscr{R}\Delta t} = \frac{q_0^k + 12\mathscr{R}\Delta t}{1+12\mathscr{R}\Delta t}, \tag{2.81}$$

$$q_n^{k+1} = 1. \tag{2.82}$$

We used the initial conditions $h = 1 + A_{\text{init}}(1-\hat{x}^2)$, $q = 1$ with $A_{\text{init}} \ll 1$.

For the calculations reported here, we found that 64 Chebyshev polynomials were typically sufficient to meet the required spatial accuracy; results were validated against a finite difference method from (Stewart *et al.*, 2009, 2010*a*). 128 modes were used in Figure 2.6.

Chapter 3

Resonance-driven oscillations

In Chapter 2, we found a degenerate bifurcation point, in a parameter regime near which growing oscillations around a uniform state can arise that are driven by divergent instabilities of nearby steady (but unstable) flexible segment configurations, in a manner that is independent of the downstream segment. This instability mechanism is by no means exclusive and its range of applicability is restricted to certain parameter regimes. In order to obtain a broader view of the origin of instabilities, we consider in this chapter the case when the downstream rigid segment is substantially longer than the flexible segment.

The model is briefly recalled in §3.1, and then the linear stability of the uniform state is described in §3.2, restricting attention to the neighbourhood of the degenerate bifurcation point. We identify three dominant balances between parameters, associated with three distinct branches of the primary Hopf neutral curve, from which we derive leading-order approximations of the linear stability problem in §3.3. One limit, in particular, forms the basis for a weakly nonlinear analysis in §3.4, from which we derive a fourth-order amplitude equation. This has two independent parameters and a rich phenomenology, which we sketch briefly. Predictions from this reduced-order model are tested against simulations of the full one-dimensional model and against two-dimensional Navier–Stokes simulations in §3.5. Our results are summarised and discussed in §3.6.

3.1 Model

In this chapter we consider the one-dimensional model governed by (1.26, 1.27) and also the corresponding two-dimensional fluid-structure interaction problem formulated in §1.4, which we solve numerically using a demonstration-driver from the finite-element library `oomph-lib` (Heil & Hazel, 2006).

According to descriptions in §1.4.3, the two-dimensional problem can be characterised by seven dimensionless parameters

$$L_1^* = \frac{L_1^{**}}{a}, \quad L^* = \frac{L^{**}}{a}, \quad L_2^* = \frac{L_2^{**}}{a}, \quad h_0^* = \frac{h_0^{**}}{a},$$
$$Q = \frac{\mu U_0}{Ea}, \quad \mathscr{R} = \frac{\mu L^{**}}{\rho a^2 U_0}, \quad T = \frac{T_0 a}{\rho U_0^2 (L^{**})^2}. \tag{3.1}$$

The parameter Q indicates the strength of the fluidstructure interaction, $\mathscr{R}$ measures the strength of viscous effects (a form of inverse Reynolds number) and T is a dimensionless tension. Under small viscous stress ($L^*/\mathscr{R} \gg 1$), the variation of the initial longitudinal tension along the membrane is negligible (Pedley, 1992). From equation (1.50) we infer that during flow-induced wall deformation, changes in membrane tension due to stretching are small compared to T if $(L^*)^5 QT/(\mathscr{R} h_0^*) \gg 1$ and the effects of bending are small if $(L^*)^5 QT/(\mathscr{R}(h_0^*)^3) \gg 1$. In two-dimensional simulations we subject the ends of the beam to pinned boundary conditions, fixing their positions but allowing them to rotate freely; we set the wall thickness $h_0^* = 0.01$ and $Q = 0.01$, and choose appropriate values of other parameters to ensure the viscous stress, wall stretching and the wall bending terms are all negligibly small. Simulations are reported in §3.5 below.

For convenience, we rewrite the boundary condition of the one-dimensional model (1.27d) as

$$\mathscr{L} T h_{xx} = -\left(12\mathscr{R}(q-1) + q_t\right), \qquad (x = 1), \tag{3.2}$$

where $\mathscr{L} = 1/L_2$. Equation (3.2) accounts for viscous and unsteady pressure drops along the downstream rigid segment in $1 < x < 1 + 1/\mathscr{L}$. Here we focus our attention on the case where the downstream rigid segment is longer than the membrane, that is $\mathscr{L} \ll 1$. We first examine the linear stability of the uniform state $h = 1$, $q = 1$.

3.2 Linear stability of the uniform state

Solving the linear eigenvalue problem (2.1, 2.2) as in Chapter 2, we obtain eigenvalue and eigenmodes then neutral curves for small $\mathscr{L}$. In the following, we focus on the neutral curves in the vicinity of the degenerate bifurcation point $(T, \mathscr{R}) = (T_{20}, 0)$.

3.2.1 Numerical results

The linearised equations (2.1, 2.2) show that static neutral curves (on which $\sigma = 0$) are independent of $\mathscr{L}$ while oscillatory neutral curves (on which $\sigma \neq 0$) depend on $\mathscr{L}$. This is illustrated by Figure 3.1(a), which shows static and oscillatory neutral curves in $(T, \mathscr{R})$-parameter space for $\mathscr{L} = 1$, 0.1 and 0.01 (a wider view of $(T, \mathscr{R})$-parameter space is given in Figure 2.1(a)). The static neutral curve in $T > T_{20}$, labelled TC_2, defines a transcritical bifurcation to a mode-2 steady solution; the oscillatory neutral curve in $T < T_{20}$, labelled Hopf_2, defines a Hopf bifurcation to mode-2 oscillations. The uniform state is linearly stable for $\mathscr{R}$ values above each neutral curve. As $\mathscr{L}$ decreases, a wobble appears on the Hopf_2 curve and the parameter range over which the uniform state is stable reduces. Defining $\mathscr{T} = T - T_{20}$, Figure 3.1(b) shows in greater detail some mode-2 oscillatory neutral curves in $(-\mathscr{T}, \mathscr{R})$-space (together with their asymptotic approximations, derived below). As $\mathscr{L}$ decreases, the wobble becomes more evident and it lies closer to $T = T_{20}$; we can then identify distinct upper-, lower- and middle-branch behaviour. As $\mathscr{R}$ decreases for fixed $\mathscr{L}$, first $-\mathscr{T}$ decreases like $O(\mathscr{R}^2)$ on the upper branch, then $-\mathscr{T}$ increases on the middle branch, and finally $-\mathscr{T}$ decreases like $O(\mathscr{R})$ on the lower branch. Figure 3.1(c) demonstrates the corresponding frequency of eigenmodes on the Hopf_2 curve. On the upper branch, the frequency of mode-2 oscillations is approximately $\sqrt{27\mathscr{L}/8}$ (as we show in (3.13) below), independent of $-\mathscr{T}$. However, the frequency is approximately $4\pi^2\sqrt{-\mathscr{T}/15}$ (see (3.27) below) on the lower branch, independent of $\mathscr{L}$.

Figure 3.2 depicts eigenvalue paths as the parameter pair $(-\mathscr{T}, \mathscr{R})$ crosses the Hopf_2 curve close to the turning point between the middle and lower branches. As seen in Figure 3.2(a), for $\mathscr{R} = 6 \times 10^{-4}$ and $-\mathscr{T} = 10^{-6}$, there exist two pairs of complex conjugate eigenvalues with almost the same negative real part, both of which are mode 2. As $-\mathscr{T}$ increases, the imaginary part of the conjugate pair with large imaginary part falls while that of the conjugate pair with small imaginary part rises, until they nearly coalesce. Then, the real part of the higher-frequency modes ascends through zero,

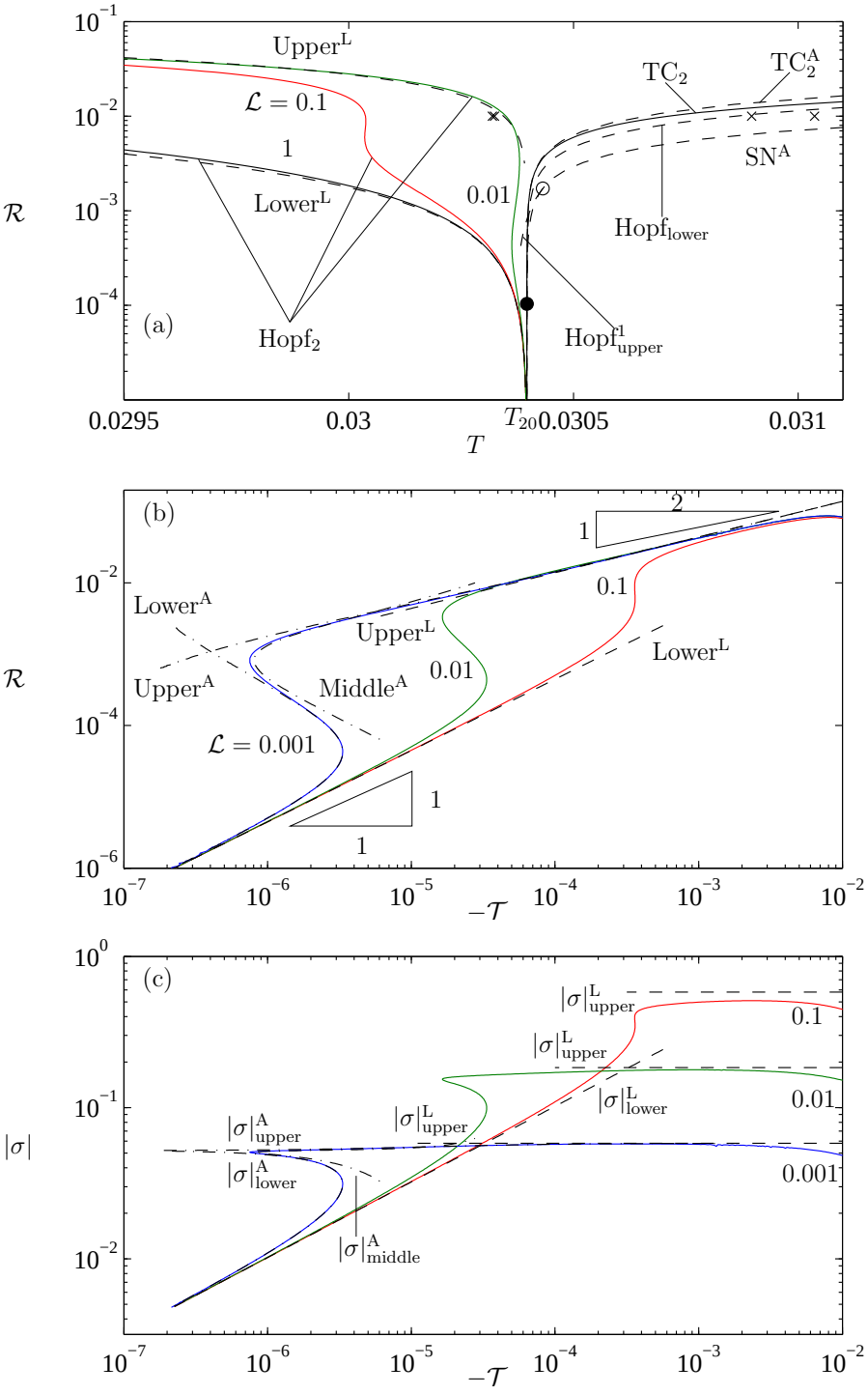
(a)
Upper^L
$\mathcal{L} = 0.1$
1
Lower^L
0.01
Hopf_2
Hopf^1_upper
Hopf_lower
TC_2
TC_2^A
SN^A
$\mathcal{R}$
T
T_{20}
0.0295
0.03
0.0305
0.031
(b)
Lower^A
Upper^A
Upper^L
Middle^A
Lower^L
$\mathcal{L} = 0.001$
0.1
0.01
2
1
1
1
$-\mathcal{T}$
(c)
$|\sigma|^L_{upper}$
$|\sigma|^L_{upper}$
$|\sigma|^L_{lower}$
$|\sigma|^L_{upper}$
$|\sigma|^A_{upper}$
$|\sigma|^A_{lower}$
$|\sigma|^A_{middle}$
0.1
0.01
0.001
$|\sigma|$
$-\mathcal{T}$

Figure 3.1: (a) Neutral curves of static mode-2 perturbations (in $T > T_{20}$, labelled TC_2, solid) and of oscillatory mode-2 perturbations (in $T < T_{20}$, labelled Hopf_2, solid) for $\mathscr{L} = 1$, 0.1 and 0.01. Dashed lines show the asymptotes (3.12) (labelled $\mathrm{Upper}^{\mathrm{L}}$) and (3.26) (labelled $\mathrm{Lower}^{\mathrm{L}}$), the asymptotes (3.51) and (3.52) from Chapter 2 (labelled $\mathrm{TC}_2^{\mathrm{A}}$ and SN^{A}) and the asymptotes (3.81) for $\mathscr{L} = 0.01$ (labelled $\mathrm{Hopf}_{\mathrm{lower}}$) that coalesces with the SN^{A} at the closed circle. The open circle on SN^{A} denotes a Takens–Bogdanov point. The crosses denote the parameters used in the PDE simulations in §3.5. (b) Hopf_2 curves for $\mathscr{L} = 0.1$, 0.01 and 0.001 (solid), in addition to the dashed lines showing the asymptotes (3.12) (labelled $\mathrm{Upper}^{\mathrm{L}}$) and (3.26) (labelled $\mathrm{Lower}^{\mathrm{L}}$) and dash-dot lines showing the asymptotes (3.10) (labelled $\mathrm{Upper}^{\mathrm{A}}$), (3.20, 3.21) (labelled $\mathrm{Lower}^{\mathrm{A}}$) and (3.32, 3.33) (labelled $\mathrm{Middle}^{\mathrm{A}}$) for $\mathscr{L} = 0.001$. (c) Frequency of neutral mode-2 oscillations for $\mathscr{L} = 0.1$, 0.01 and 0.001 (solid), as well as dashed lines showing the asymptotes (3.13) (labelled $|\sigma|^{\mathrm{L}}_{\mathrm{upper}}$) and (3.27) (labelled $|\sigma|^{\mathrm{L}}_{\mathrm{lower}}$); the dash-dot lines show the asymptotes (3.11) (labelled $|\sigma|^{\mathrm{A}}_{\mathrm{upper}}$), (3.20, 3.21) (labelled $|\sigma|^{\mathrm{A}}_{\mathrm{lower}}$) and (3.32, 3.33) (labelled $|\sigma|^{\mathrm{A}}_{\mathrm{middle}}$) for $\mathscr{L} = 0.001$.

which corresponds to crossing the middle branch of the neutral curve in Figure 3.1(b). Subsequently, the pair collide and split into two positive real eigenvalues. In the meantime, the lower-frequency pair remain stable but coalesce and become two negative real eigenvalues. The eigenvalue path in Figure 3.2(c), for $\mathscr{R} = 2 \times 10^{-4}$, is similar to that in Figure 3.2(a) except that it is the lower-frequency modes that become unstable on crossing the lower branch of the neutral curve; this resembles the behaviour analysed in Chapter 2. The intermediate case is shown in Figure 3.2(b). This mode interaction is strongly reminiscent of a 1:1 resonance, and suggests a possible mechanism of self-excited oscillation consistent with the conjecture of Mandre & Mahadevan (2010). Figure 3.1(c) shows how the frequency of neutral modes approaches zero as $\mathscr{L} \to 0$, $\mathscr{T} \to 0$ and $\mathscr{R} \to 0$. Thus the structure illustrated in Figure 3.2 collapses to the origin in this limit, yielding four zero eigenvalues.

For larger $\mathscr{R}$, corresponding to moving up the middle and upper branches of the Hopf_2 curve, there are further changes to the pattern of eigenvalues. Figure 3.3 illustrates the eigenvalue paths towards the upper end of the upper branch. As $-\mathscr{T}$ increases, the eigenvalue pair with initially higher frequency remains stable, while two real eigenvalues coalesce to form a conjugate pair that become unstable.

In Figure 3.4 we replot the oscillatory neutral curves of Figure 3.1(b) to reveal their dependence on $\mathscr{L}$. In Figure 3.4(a) we plot $-\mathscr{T}/\mathscr{L}$ versus $\mathscr{R}/\mathscr{L}^{1/2}$ and find that the upper branches of the neutral curves coalesce, which suggests that the upper branch

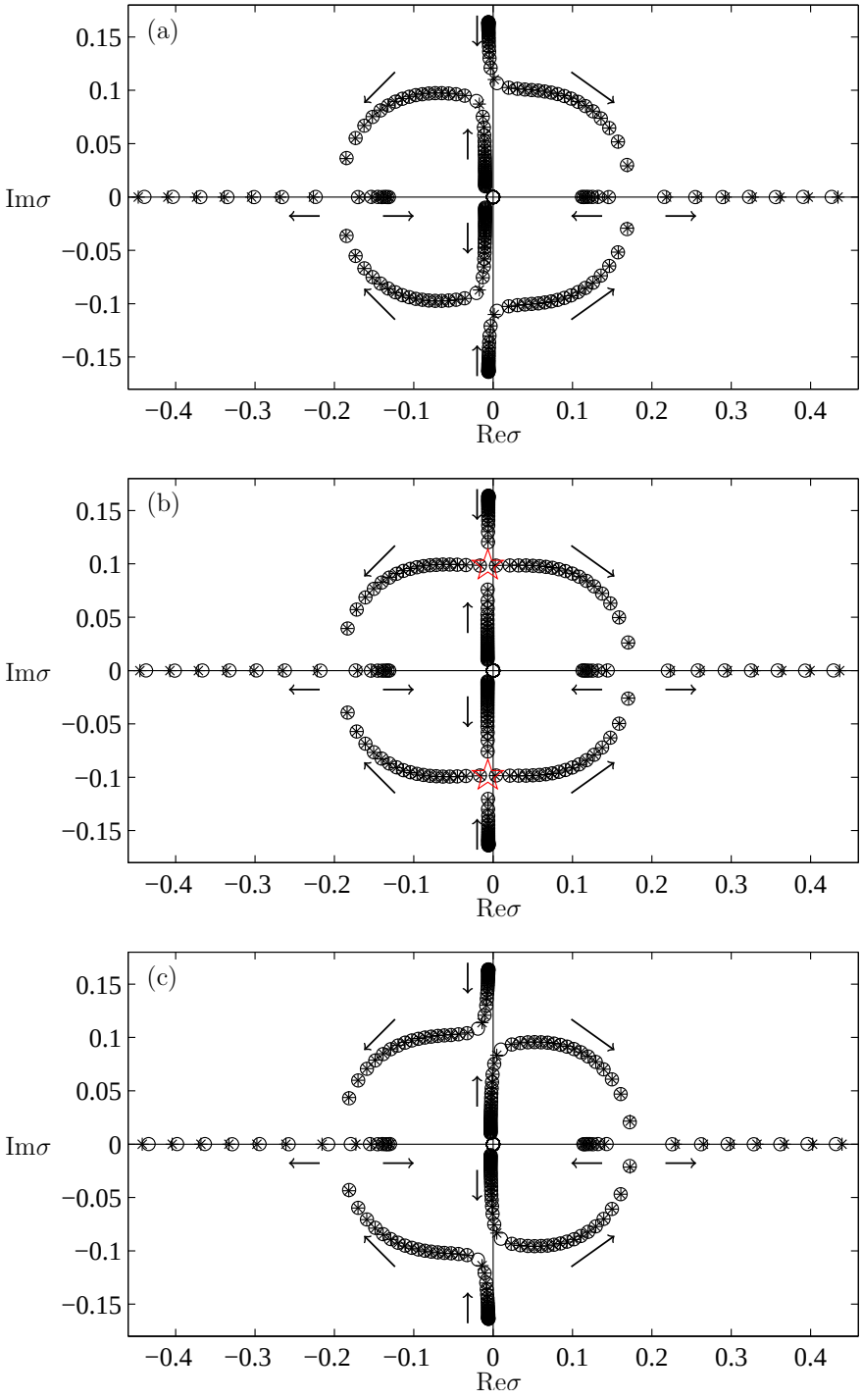

Figure 3.2: Eigenvalue paths as $-\mathscr{T}$ varies from 10^{-6} to 10^{-3} with $\mathscr{L} = 0.01$ and (a) $\mathscr{R} = 6 \times 10^{-4}$, (b) $\mathscr{R} = 4.27 \times 10^{-4}$ (from (3.22)) and (c) $\mathscr{R} = 2 \times 10^{-4}$. Circles represent numerical results from (2.1, 2.2) while asterisks represent asymptotic results from (3.20, 3.21) for the same value of $\mathscr{T}$. In (b), two stars are the pair of eigenvalues on coalescence, from (3.24). Arrows show increasing $-\mathscr{T}$.

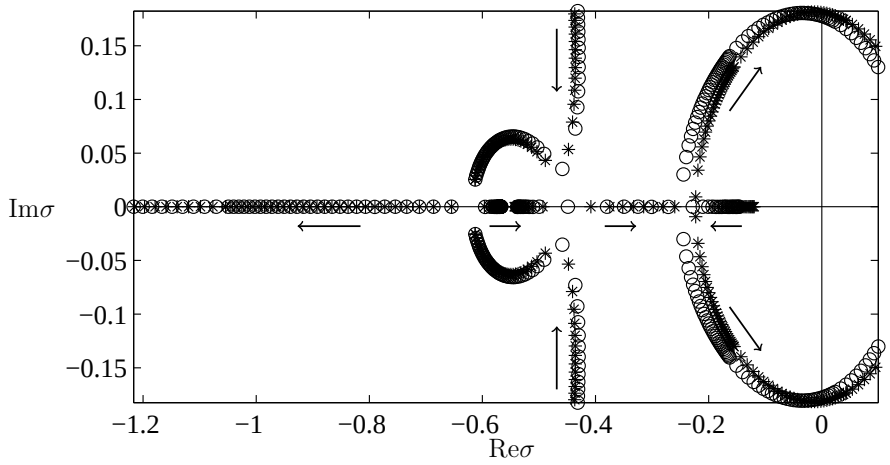

Figure 3.3: Eigenvalue path as T varies from 0.0306 to 0.028 with $\mathscr{L} = 0.01$ and $\mathscr{R} = 1/22$. Circles represent numerical results from (2.1, 2.2) while asterisks represent asymptotic results from (3.9).

has the scaling $\mathscr{R}^2 \sim -\mathscr{T} \sim \mathscr{L}$ as $\mathscr{L} \to 0$, $\mathscr{T} \to 0$ and $\mathscr{R} \to 0$. Similarly, by plotting $-\mathscr{T}/\mathscr{L}$ versus $\mathscr{R}/\mathscr{L}$, collapse of the data in Figure 3.4(c) suggests the lower branch and the lower turning point have the scaling $\mathscr{R} \sim -\mathscr{T} \sim \mathscr{L}$. For the middle branch, we plot $-\mathscr{T}/\mathscr{L}^{3/2}$ versus $\mathscr{R}/\mathscr{L}^{1/2}$ (Figure 3.4(b)). In this case, a rough coalescence can be seen, sufficient to motivate investigation of this scaling relationship. We recall from Chapter 2 that TC_2 follows the scaling $\mathscr{T} \sim \mathscr{R}^2$, independent of $\mathscr{L}$.

3.3 Parametric asymptotics

We now seek asymptotic approximations of the linear stability problem by expanding the solution in the neighbourhood of $(\mathscr{T},\mathscr{R},\mathscr{L}) = (0,0,0)$, seeking to unfold the patterns traced out by the four eigenvalues close to the origin. We assume different relations between the parameters in order to capture behaviour on the lower, middle and upper branches of the Hopf_2 curve. We make expansions using

$$Q(x) = Q_0(x) + \varepsilon Q_1(x) + \varepsilon^2 Q_2(x) + \varepsilon^3 Q_3(x) + \cdots, \tag{3.3a}$$

$$H(x) = H_0(x) + \varepsilon H_1(x) + \varepsilon^2 H_2(x) + \varepsilon^3 H_3(x) + \cdots, \tag{3.3b}$$

$$\sigma = \varepsilon\sigma_1 + \varepsilon^2\sigma_2 + \varepsilon^3\sigma_3 + \cdots, \tag{3.3c}$$

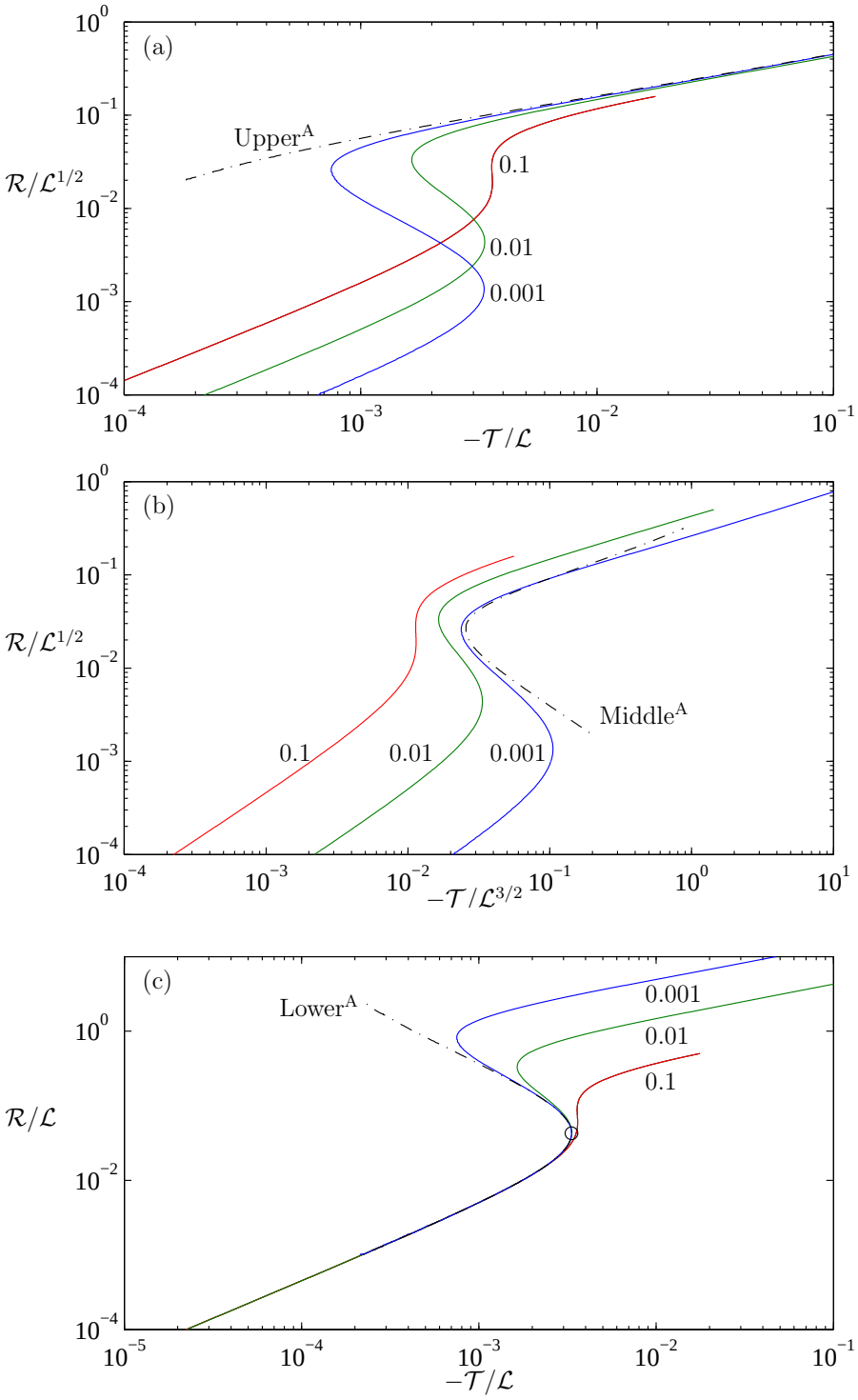

Figure 3.4: Oscillatory mode-2 neutral curves for $\mathscr{L} = 0.1$, 0.01 and 0.001 (solid), in addition to the dash-dot lines showing the asymptotes (3.10) (labelled Upper$^{\mathrm{A}}$), (3.20, 3.21) (labelled Lower$^{\mathrm{A}}$) and (3.32, 3.33) (labelled Middle$^{\mathrm{A}}$). The circle in panel (c) represents the coalescence point from (3.22, 3.23).

where $0 < \varepsilon \ll 1$ is a tuning parameter; the coefficients in (3.3) are assumed to be of order unity as $\varepsilon \to 0$. Details of the expansions are provided in Appendix 3.A.

3.3.1 Upper branch: $\mathscr{R}^2 \sim -\mathscr{T} \sim \mathscr{L}$

Motivated by Figure 3.4(a) we scale the parameters as

$$\mathscr{T} = \varepsilon^2 \mathscr{T}_2, \quad \mathscr{R} = \varepsilon \mathscr{R}_1, \quad \mathscr{L} = \varepsilon^2 \mathscr{L}_2. \tag{3.4}$$

Here $\mathscr{T}_2$, $\mathscr{R}_1$ and $\mathscr{L}_2$ are assumed to be of order unity as $\varepsilon \to 0$. Upon substituting (3.3) and (3.4) into (2.1, 2.2), one homogeneous system (3.70) and a series of inhomogeneous systems (3.71, 3.72) are recovered in succession. Solutions of (3.70) can be derived directly. For each inhomogeneous system, the existence of non-trivial solutions requires a solvability condition, which provides conditions on coefficients appearing at previous orders.

At $O(1)$, solutions of (3.70) are

$$Q_0 = 0, \qquad H_0 = A_0 \sin 2\pi x + B_0(1 - \cos 2\pi x). \tag{3.5}$$

Here A_0 and B_0 are constants. The A_0 component is a typical “mode-2" solution, whereas the B_0 component has the same wavelength but a single extremum in h at the mid-point of the membrane.

At $O(\varepsilon)$, the solvability condition of (3.71) requires $B_0 = 0$, which admits solutions

$$Q_1 = A_0 \sigma_1 (\cos 2\pi x - 1)/2\pi, \tag{3.6a}$$

$$H_1 = A_1 \sin 2\pi x + B_1(1 - \cos 2\pi x) + A_0(15\mathscr{R}_1 + \sigma_1) x \sin 2\pi x. \tag{3.6b}$$

Here A_1 and B_1 are constants. Thus the single-humped mode (B_1) persists but with smaller magnitude than the primary mode-2 component. Note that $Q_1(1) = 0$, so that the downstream rigid channel segment has no influence at this order.

At $O(\varepsilon^2)$, the solvability conditions of (3.72) give the conditions

$$B_1 = -\frac{A_0(15\mathscr{R}_1+\sigma_1)(12\mathscr{L}_2+5\sigma_1(12\mathscr{R}_1+\sigma_1))}{4\pi^2(6\mathscr{L}_2-5\sigma_1(12\mathscr{R}_1+\sigma_1))}, \tag{3.7a}$$

$$\mathscr{T}_2 = \frac{3\left(6\mathscr{L}_2\left(1350\mathscr{R}_1^2+168\mathscr{R}_1\sigma_1+5\sigma_1^2\right)+\sigma_1(12\mathscr{R}_1+\sigma_1)\left(1350\mathscr{R}_1^2+240\mathscr{R}_1\sigma_1+11\sigma_1^2\right)\right)}{16\pi^4(6\mathscr{L}_2-5\sigma_1(12\mathscr{R}_1+\sigma_1))}, \tag{3.7b}$$

which admits solutions H_2 and Q_2. We find that

$$Q_2(1) = \sigma_1\left(\frac{15\mathscr{R}_1+\sigma_1}{2\pi}A_0 - B_1\right) = -\frac{18\mathscr{L}_2 B_1}{12\mathscr{L}_2+5\sigma_1(12\mathscr{R}_1+\sigma_1)}, \tag{3.8}$$

which means that there exists a weak flux perturbation influenced by the downstream rigid segment. In particular, the B_1 mode drives sloshing in the downstream segment that brings in the coupling to $\mathscr{L}$. The first condition (3.7a) slaves the single-humped mode to the primary mode-2 solution. The second condition (3.7b) gives a quartic for σ_1, which we re-express as

$$\begin{aligned}&12\mathscr{L}\left(2025\mathscr{R}^2-8\pi^4\mathscr{T}\right)+24\mathscr{R}\left(2025\mathscr{R}^2+126\mathscr{L}+40\pi^4\mathscr{T}\right)\sigma\\&+10\left(1269\mathscr{R}^2+9\mathscr{L}+8\pi^4\mathscr{T}\right)\sigma^2+1116\mathscr{R}\sigma^3+33\sigma^4=0.\end{aligned} \tag{3.9}$$

Figure 3.3 shows how (3.9) successfully approximates the solution of (2.1, 2.2).

If we assume σ is purely imaginary and isolate the real and imaginary parts of (3.9), we obtain explicit expressions for the upper branch of the Hopf_2 curve and the corresponding neutral frequency as

$$\mathscr{T} = \frac{9\left(-1183\mathscr{L}-59700\mathscr{R}^2+31\sqrt{3}\sqrt{(3\mathscr{L}+200\mathscr{R}^2)(161\mathscr{L}+2400\mathscr{R}^2)}\right)}{4000\pi^4}, \tag{3.10}$$

and

$$\sigma = \pm\mathrm{i}\sqrt{\frac{21\mathscr{L}}{50}-72\mathscr{R}^2+\frac{3}{50}\sqrt{3}\sqrt{483\mathscr{L}^2+39400\mathscr{L}\mathscr{R}^2+480000\mathscr{R}^4}}. \tag{3.11}$$

Good agreement between (3.10, 3.11) and predictions from the linearised equations (2.1, 2.2) can be seen in Figure 3.1(b, c) and Figure 3.4(a), although the approximation (3.10) (labelled $\mathrm{Upper}^{\mathrm{A}}$ in Figure 3.1(b)) does not capture the upper turning point in

the neutral curve.

Assuming $1 \gg \mathscr{R}^2 \sim -\mathscr{T} \gg \mathscr{L}$ in (3.10), the upper branch of the Hopf_2 curve asymptotes to

$$-\mathscr{T} = \frac{405}{8\pi^4}\mathscr{R}^2, \tag{3.12}$$

shown in Figure 3.1(a, b) as Upper^{L}; the approximate neutral frequency in (3.11) becomes

$$\sigma = \pm \mathrm{i}\sqrt{\frac{27\mathscr{L}}{8}}, \tag{3.13}$$

as shown in Figure 3.1(c). Interestingly, the neutral curve asymptote (3.12) is independent of $\mathscr{L}$, whereas the oscillation frequency (3.13) is independent of $\mathscr{T}$. In addition, setting $\sigma = 0$ in (3.9) recovers the locations of the TC_2 curve, $\mathscr{T} = 2025\mathscr{R}^2/8\pi^4$ provided $\mathscr{L} > 0$ (Chapter 2), shown as TC_2^{A} in Figure 3.1(a).

Assuming $\mathscr{L}^{3/2} \ll \mathscr{T} \ll \mathscr{L} \sim \mathscr{R}^2$, by balancing terms in (3.9) at increasing order, we derive eigenvalues

$$\sigma = \overline{\sigma_1} + \overline{\sigma_2} + \cdots, \tag{3.14}$$

where $\overline{\sigma_1} \gg \overline{\sigma_2}$ and $\overline{\sigma_1}$, $\overline{\sigma_2}$ satisfy

$$\begin{aligned} &8100\mathscr{L}\mathscr{R}^2 + 72\mathscr{R}\left(14\mathscr{L} + 225\mathscr{R}^2\right)\overline{\sigma_1} + 30\left(\mathscr{L} + 141\mathscr{R}^2\right)\overline{\sigma_1}^2 \\ &+ 372\mathscr{R}\overline{\sigma_1}^3 + 11\overline{\sigma_1}^4 = 0, \end{aligned} \tag{3.15a}$$

$$\begin{aligned} \overline{\sigma_2} = -96\pi^4\mathscr{T}\overline{\sigma_1}(12\mathscr{R} + \overline{\sigma_1})(15\mathscr{R} + \overline{\sigma_1})^2/\big(&2^3 3^7 5^4\mathscr{R}^5 + 2^2 3^5 5^3 47\mathscr{R}^4\overline{\sigma_1} \\ &+ 2^3 3^3 5\cdot 23\cdot 43\mathscr{R}^3\overline{\sigma_1}^2 + 2^2 3^2 13\cdot 197\mathscr{R}^2\overline{\sigma_1}^3 + 3702\mathscr{R}\overline{\sigma_1}^4 + 55\overline{\sigma_1}^5\big), \end{aligned} \tag{3.15b}$$

respectively, which represent the overlap with the middle branch, as we will see below.

3.3.2 Lower branch: $\mathscr{R} \sim -\mathscr{T} \sim \mathscr{L}$

Motivated by Figure 3.4(c) we now assume

$$\mathscr{T} = \varepsilon^2\mathscr{T}_2, \quad \mathscr{R} = \varepsilon^2\mathscr{R}_2, \quad \mathscr{L} = \varepsilon^2\mathscr{L}_2. \tag{3.16}$$

Here $\mathscr{T}_2$, $\mathscr{R}_2$ and $\mathscr{L}_2$ are assumed to be of order unity as $\varepsilon \to 0$. Upon substituting (3.3) and (3.16) into the linearised equations (2.1, 2.2), one homogeneous system and a series of inhomogeneous systems (see Appendix 3.A.2) are recovered in succession, following the pattern in the upper-branch calculation.

At $O(1)$, solutions of (3.73) are as in (3.5). At $O(\varepsilon)$, the solvability condition of (3.74) is again $B_0 = 0$, which admits solutions

$$Q_1 = A_0\sigma_1(\cos 2\pi x - 1)/2\pi, \tag{3.17a}$$

$$H_1 = A_1 \sin 2\pi x + B_1(1-\cos 2\pi x) + A_0\sigma_1 x \sin 2\pi x, \tag{3.17b}$$

missing a viscous term present in (3.6b).

At $O(\varepsilon^2)$, the solvability conditions of (3.75) are

$$B_1 = -\frac{A_0\sigma_1\left(12\mathscr{L}_2+5\sigma_1^2\right)}{4\pi^2\left(6\mathscr{L}_2-5\sigma_1^2\right)}, \quad \mathscr{T}_2 = \frac{3\sigma_1^2\left(30\mathscr{L}_2+11\sigma_1^2\right)}{16\pi^4\left(6\mathscr{L}_2-5\sigma_1^2\right)}, \tag{3.18a,b}$$

which secures solutions Q_2 and H_2 containing two new coefficients A_2 and B_2. Notice that (3.18) corresponds to (3.7) in the limit of $\mathscr{R}_1 \to 0$. Then Q_0, H_0, Q_1, H_1, Q_2 and H_2 are inserted into inhomogeneous terms of the next order problem, in order to take into account viscous effects.

At $O(\varepsilon^3)$, the solvability conditions of (3.76) are

$$\begin{aligned} B_2 =& \Big(60A_1\sigma_1\left(-2160\mathscr{L}_2^3-2484\mathscr{L}_2^2\sigma_1^2+275\sigma_1^6\right) \\ &+A_0\big(2^6 3^6 5\mathscr{L}_2^3\mathscr{R}_2-432\mathscr{L}_2^2(559\mathscr{L}_2-4185\mathscr{R}_2)\sigma_1^2-2^2 3^2\cdot 5\cdot 1327\mathscr{L}_2^2\sigma_1^4 \\ &+1500(-22\mathscr{L}_2+45\mathscr{R}_2)\sigma_1^6+5^3 11\cdot 23\sigma_1^8\big)\Big) \\ &/\Big(240\pi^2\left(6\mathscr{L}_2-5\sigma_1^2\right)\left(180\mathscr{L}_2^2+132\mathscr{L}_2\sigma_1^2-55\sigma_1^4\right)\Big), \end{aligned} \tag{3.19a}$$

$$\sigma_2 = \frac{24\left(-630\mathscr{L}_2^2\mathscr{R}_2+3\mathscr{L}_2(-9\mathscr{L}_2+35\mathscr{R}_2)\sigma_1^2+125\mathscr{R}_2\sigma_1^4\right)}{900\mathscr{L}_2^2+660\mathscr{L}_2\sigma_1^2-275\sigma_1^4}. \tag{3.19b}$$

Here we finally see the appearance of viscous terms, plus additional interactions not present in (3.7). The solvability conditions (3.18b) and (3.19b) give the eigenvalue

$$\sigma = \overline{\sigma_1} + \overline{\sigma_2}, \tag{3.20}$$

where $\overline{\sigma_1}$ and $\overline{\sigma_2}$ satisfy

$$\overline{\sigma_1}^2 = \frac{-45\mathscr{L} - 40\pi^4\mathscr{T} \pm \sqrt{2025\mathscr{L}^2 + 6768\mathscr{L}\pi^4\mathscr{T} + 1600\pi^8\mathscr{T}^2}}{33}, \tag{3.21a}$$

$$\overline{\sigma_2} = \frac{24\left(-630\mathscr{L}^2\mathscr{R} + 3\mathscr{L}(-9\mathscr{L} + 35\mathscr{R})\overline{\sigma_1}^2 + 125\mathscr{R}\overline{\sigma_1}^4\right)}{900\mathscr{L}^2 + 660\mathscr{L}\overline{\sigma_1}^2 - 275\overline{\sigma_1}^4}. \tag{3.21b}$$

From (3.20, 3.21), the asymptote of the Hopf$_2$ curve (which we denote Lower$^{\mathrm{A}}$) and the corresponding neutral frequency ($|\sigma|^{\mathrm{A}}_{\mathrm{lower}}$) can be determined. We see good agreement between these predictions and solutions of (2.1, 2.2) in Figure 3.1(b, c) and Figure 3.4(c). The lower-branch approximation captures the lower turning point in the neutral curve but does not connect smoothly to the upper-branch approximation, showing the need for a middle-branch approximation, given below.

Figure 3.2 shows eigenvalue paths computed from (3.20, 3.21) and from (2.1, 2.2), which again agree well. Equation (3.20) captures the coalescence of two pairs of conjugate eigenvalues, which takes place when

$$\mathscr{R} = \frac{11\left(\sqrt{11} - 6\right)\mathscr{L}}{90\left(\sqrt{11} - 11\right)} \approx 0.0427\mathscr{L}, \tag{3.22}$$

$$-\mathscr{T} = \frac{9\left(47 - 12\sqrt{11}\right)\mathscr{L}}{200\pi^4} \approx 0.0033\mathscr{L}; \tag{3.23}$$

the corresponding pair of eigenvalues are

$$\sigma = -\frac{\left(539 - 31\sqrt{11}\right)\mathscr{L}}{660} \pm \mathrm{i}\sqrt{\frac{\left(36\sqrt{11} - 66\right)\mathscr{L}}{55}}. \tag{3.24}$$

The agreement between the asymptotic and numerical results can be observed in Figure 3.2(b). In Figure 3.4(c) we see that the coalescence point lies close to the lower turning point of the mode-2 neutral curve. As (3.24) and Figure 3.2(b) indicate, when the two modes interact they are almost neutrally stable, with small decay rate of $O(\mathscr{L})$. The rapid rise in growth rate of one mode is characteristic of a 1:1 resonance. Note that the two interacting eigenmodes are each of mode-2 type, with a two-humped A_0 contribution supplemented with a smaller one-humped B_1 contribution (see (3.18a)).

Assuming $\mathscr{R} \sim -\mathscr{T} \ll \mathscr{L}$, the two eigenvalue components are given from (3.21a)

and (3.21b) as

$$\overline{\sigma_1} = \pm 4\pi^2 \mathrm{i}\sqrt{\frac{-\mathscr{T}}{15}} + \cdots, \qquad \overline{\sigma_2} = -\frac{12}{125}\left(175\mathscr{R} + 8\pi^4\mathscr{T}\right) + \cdots, \tag{3.25}$$

thus the real part of $\overline{\sigma}$ vanishes when

$$-\mathscr{T} = \frac{175}{8\pi^4}\mathscr{R}, \tag{3.26}$$

shown in Figure 3.1(a, b) as Lower$^{\mathrm{L}}$, and the approximate neutral frequency is

$$\sigma = \pm 4\pi^2 \mathrm{i}\sqrt{\frac{-\mathscr{T}}{15}}, \tag{3.27}$$

shown in Figure 3.1(c) as $|\sigma|^{\mathrm{L}}_{\mathrm{lower}}$. Here we recover results given in Chapter 2 for the case where the downstream rigid channel is sufficiently short to have no leading-order influence. In this case, the dominant balance in the boundary condition (2.2) at $x = 1$ is $H'' = 0$, implying zero pressure perturbation. The neutral oscillation is captured by the A_0 mode in (3.17), and does not require a contribution from the B_1 mode.

Assuming $\mathscr{L}^{3/2} \ll -\mathscr{T} \ll \mathscr{L} \ll \mathscr{R} \ll \mathscr{L}^{1/2}$, i.e. beyond the turning point of the lower-branch approximation, by balancing terms in (3.21a) and (3.21b) at increasing order, we obtain

$$\overline{\sigma_1} = \pm \mathrm{i}\sqrt{\frac{30}{11}}\mathscr{L}^{1/2} \pm \frac{16\pi^4\mathrm{i}}{5}\sqrt{\frac{6}{55}}\frac{\mathscr{T}}{\sqrt{\mathscr{L}}} + \cdots, \tag{3.28}$$

$$\overline{\sigma_2} = -\frac{6\mathscr{R}}{55} - \frac{3\mathscr{L}}{5} - \frac{2016\pi^4\mathscr{R}\mathscr{T}}{125\mathscr{L}} + \cdots, \tag{3.29}$$

Thus the two approximate eigenvalues are

$$\sigma = -\left(\frac{6\mathscr{R}}{55} + \frac{3\mathscr{L}}{5} + \frac{2016\pi^4\mathscr{R}\mathscr{T}}{125\mathscr{L}}\right) \pm \mathrm{i}\left(\sqrt{\frac{30}{11}}\mathscr{L}^{1/2} + \frac{16\pi^4}{5}\sqrt{\frac{6}{55}}\frac{\mathscr{T}}{\sqrt{\mathscr{L}}}\right) + \cdots, \tag{3.30}$$

which represent the overlap with the middle branch, as we see below.

3.3.3 Middle branch: $\mathscr{R}(-\mathscr{T}) \sim \mathscr{L}^2$

In order to connect the upper limit of the lower branch (3.30) to the lower limit of the upper branch (3.14, 3.15), we introduce a third region. Motivated by Figure 3.4(b), we introduce the scalings

$$\mathscr{T} = \varepsilon^3 \mathscr{T}_3, \quad \mathscr{R} = \varepsilon \mathscr{R}_1, \quad \mathscr{L} = \varepsilon^2 \mathscr{L}_2. \tag{3.31}$$

Here $\mathscr{T}_3$, $\mathscr{R}_1$ and $\mathscr{L}_2$ are assumed to be of order unity as $\varepsilon \to 0$. Upon substituting (3.3) and (3.31) into the linearised equations (2.1, 2.2), one homogeneous system and a series of inhomogeneous systems (see Appendix 3.A.3) are recovered in succession.

Defining

$$\begin{aligned} f(\mathscr{R},\mathscr{L},\sigma) &= 8100\mathscr{L}\mathscr{R}^2 + 72\mathscr{R}\left(14\mathscr{L} + 225\mathscr{R}^2\right)\sigma + 30\left(\mathscr{L} + 141\mathscr{R}^2\right)\sigma^2 \\ &\quad + 372\mathscr{R}\sigma^3 + 11\sigma^4, \end{aligned} \tag{3.32a}$$

$$\begin{aligned} g_1(\mathscr{T},\mathscr{R},\sigma) &= \sigma(12\mathscr{R}+\sigma)(15\mathscr{R}+\sigma)\left(\left(1350\mathscr{R}^2 + 240\mathscr{R}\sigma + 11\sigma^2\right)^2\right. \\ &\quad \left. - 960\pi^4(15\mathscr{R}+\sigma)\mathscr{T}\right), \end{aligned} \tag{3.32b}$$

$$\begin{aligned} g_2(\mathscr{R},\sigma) &= 10\big(2^3 3^7 5^4 \mathscr{R}^5 + 2^2 3^5 5^3 47 \mathscr{R}^4\sigma + 2^3 3^3 5\cdot 23\cdot 43\mathscr{R}^3\sigma^2 \\ &\quad + 2^2 3^2 13\cdot 197\mathscr{R}^2\sigma^3 + 3702\mathscr{R}\sigma^4 + 55\sigma^5\big), \end{aligned} \tag{3.32c}$$

using the method in previous subsections, we derive two solvability conditions $f(\mathscr{R}_1,\mathscr{L}_2,\sigma_1) = 0$ and $\sigma_2 = g_1(\mathscr{T}_3,\mathscr{R}_1,\sigma_1)/g_2(\mathscr{R}_1,\sigma_1)$, which give the eigenvalue

$$\sigma = \overline{\sigma_1} + \overline{\sigma_2}, \tag{3.33}$$

where $\overline{\sigma_1}$ satisfies $f(\mathscr{R},\mathscr{L},\overline{\sigma_1}) = 0$ and $\overline{\sigma_2} = g_1(\mathscr{T},\mathscr{R},\overline{\sigma_1})/g_2(\mathscr{R},\overline{\sigma_1})$. We can see qualitative agreement between the neutral curves and the corresponding neutral frequency determined from (3.32, 3.33) and from the linearised equations (2.1, 2.2) in Figure 3.1(b, c) and Figure 3.4(b).

Assuming $\mathscr{L}^{3/2} \ll \mathscr{T} \ll \mathscr{L} \sim \mathscr{R}^2$, by balancing terms in (3.32) at increasing order, we recover the same eigenvalues in (3.14, 3.15), matching the middle- and upper-branch solutions.

Assuming $\mathscr{L}^{3/2} \ll -\mathscr{T} \ll \mathscr{L} \ll \mathscr{R} \ll \mathscr{L}^{1/2}$, by balancing terms in (3.32) at in-

creasing order we have

$$\overline{\sigma_1} = \pm \mathrm{i}\sqrt{\frac{30}{11}}\mathscr{L}^{1/2} - \frac{6\mathscr{R}}{55} + \cdots, \tag{3.34}$$

$$\overline{\sigma_2} = \pm \frac{16\pi^4\mathrm{i}}{5}\sqrt{\frac{6}{55}}\frac{\mathscr{T}}{\sqrt{\mathscr{L}}} - \frac{3\mathscr{L}}{5} - \frac{2016\pi^4\mathscr{R}\mathscr{T}}{125\mathscr{L}} + \cdots, \tag{3.35}$$

Thus we have two approximate eigenvalues being same as that in (3.30); thus the middle-branch solution matches onto the lower-branch solution.

As is evident from (3.32), the dominant physical balance on the middle branch is intricate and we do not attempt to pursue it further. The oscillation mechanism described in Chapter 2 explains the behaviour at the base of the lower branch. The instability is amplified by the resonant mode interaction illustrated in Figure 3.2. The first impact of the downstream rigid channel is to generate the lower bend in the mode-2 Hopf neutral curves. Beyond the other bend, on the upper branch of the Hopf_2 curve, there is less evidence of resonance (Figure 3.3), but nevertheless a mode interaction generates instability. We focus now on this branch, investigating how nonlinearity influences the interaction between the two mode-2 eigenmodes.

3.4 Weakly nonlinear theory for the upper branch

3.4.1 Derivation of amplitude equations

Returning to the scalings used in §3.3.1, we expand variables as

$$\phi(x;\tau_0,\tau_1) = 1 + \varepsilon\phi_0 + \varepsilon^2\phi_1 + \varepsilon^3\phi_2 + \varepsilon^4\phi_3 + \cdots, \tag{3.36}$$

where $\tau_0 = \varepsilon t$, $\tau_1 = \varepsilon^2 t$, $\phi \equiv (q,h)^{\mathrm{T}}$ and $\phi_i \equiv (q_i,h_i)^{\mathrm{T}}$, $i = 0,1,2,3$, etc. Here τ_0, τ_1, q_i, h_i, $\mathscr{T}_2$, $\mathscr{R}_1$ and $\mathscr{L}_2$ (see (3.4)) are assumed to be of order unity as $\varepsilon \to 0$.

The leading-order system is

$$q_{0x} = 0, \tag{3.37a}$$

$$6h_{0x} - 12q_{0x} + 5T_{20}h_{0xxx} = 0, \tag{3.37b}$$

$$h_0 = 0, \quad q_0 = 0, \qquad (x = 0), \tag{3.37c}$$

$$h_0 = 0, \quad 12\mathscr{R}_1 q_0 + q_{0\tau_0} = 0, \qquad (x = 1), \tag{3.37d}$$

and so, as in (3.5),

$$q_0 = 0, \quad h_0 = A_0 \sin 2\pi x + B_0(1 - \cos 2\pi x). \tag{3.38}$$

Here A_0 and B_0 are functions of τ_0 and τ_1.

The first-order system is

$$q_{1x} = -h_{0\tau_0}, \tag{3.39a}$$

$$6h_{1x} - 12q_{1x} + 5T_{20}h_{1xxx} = -180\mathscr{R}_1 h_0 + 60\mathscr{R}_1 q_0 + 5q_{0\tau_0} - 12q_0 h_{0x} + 12h_0 q_{0x} + 12q_0 q_{0x} - 15T_{20}h_0 h_{0xxx}. \tag{3.39b}$$

$$h_1 = 0, \quad q_1 = 0, \quad (x = 0), \tag{3.39c}$$

$$h_1 = 0, \quad 12\mathscr{R}_2 q_{0x} + 12\mathscr{R}_1 q_{1x} + q_{1\tau_0} + \mathscr{L}_2 T_{20} h_{0xx} = 0, \quad (x = 1). \tag{3.39d}$$

Solvability conditions for the first-order system require that

$$B_{0\tau_0} + B_0(\pi A_0 + 15\mathscr{R}_1) = 0, \tag{3.40a}$$

$$5\left(B_{0\tau_0\tau_0} + 12\mathscr{R}_1 B_{0\tau_0}\right) - 6B_0\mathscr{L}_2 = 0. \tag{3.40b}$$

This system has a divergently unstable mode for $\mathscr{R}_1 > 0$, which we suppress by enforcing $B_0 = 0$. Thus the solution of the first-order system is (cf. (3.6))

$$q_1 = A_{0\tau_0}(\cos 2\pi x - 1)/2\pi, \tag{3.41a}$$

$$h_1 = A_1 \sin 2\pi x + B_1(1 - \cos 2\pi x) - \frac{A_0^2}{4}(\cos 2\pi x - \cos 4\pi x) + (15A_0\mathscr{R}_1 + A_{0\tau_0})x \sin 2\pi x. \tag{3.41b}$$

Here A_1 and B_1 are arbitrary functions of τ_0 and τ_1. The $\sin 2\pi x$ mode appears in h_0 in (3.38), so we assume $A_1 = 0$ without loss of generality.

Solvability conditions for the second-order system require that

$$A_0\left(72\pi^2 B_1 - 4050\mathscr{R}_1^2 + 80\pi^4\mathscr{T}_2 - 36\pi A_{0\tau_0}\right) + 72\pi\left(15\mathscr{R}_1 B_1 + B_{1\tau_0}\right) = 45\left(\pi A_0^2(\pi A_0 + 30\mathscr{R}_1) + 8\mathscr{R}_1 A_{0\tau_0}\right) + 3A_{0\tau_0\tau_0}, \tag{3.42a}$$

$$\pi\left(9\mathscr{L}_2A_0^2+10\left(12\mathscr{R}_1B_{1\tau_0}+B_{1\tau_0\tau_0}\right)\right)$$
$$=3\left(4\pi\mathscr{L}_2B_1+60\mathscr{L}_2\mathscr{R}_1A_0+4\left(\mathscr{L}_2+75\mathscr{R}_1^2\right)A_{0\tau_0}+45\mathscr{R}_1A_{0\tau_0\tau_0}\right)+5A_{0\tau_0\tau_0\tau_0}, \tag{3.42b}$$

which generalises (3.7).

By using the original parameters $\mathscr{T}$, $\mathscr{R}$, $\mathscr{L}$, time t and defining amplitude functions $A=\varepsilon A_0$, $B=\varepsilon^2B_1$, we can therefore assemble terms to give

$$h=1+A(t)\sin2\pi x+B(t)(1-\cos2\pi x)$$
$$-\frac{A(t)^2}{4}(\cos2\pi x-\cos4\pi x)+(15\mathscr{R}A(t)+A_t)x\sin2\pi x+\cdots, \tag{3.43a}$$
$$q=1+A_t(\cos2\pi x-1)/2\pi+\frac{1}{8\pi^2}\Big(60\pi\mathscr{R}A_tx\cos2\pi x+2\pi A(t)A_t\sin2\pi x-30\mathscr{R}A_t\sin2\pi x$$
$$-\pi A(t)A_t\sin4\pi x-8\pi^2B_tx+4\pi B_t\sin2\pi x+4\pi A_{tt}x\cos2\pi x-2A_{tt}\sin2\pi x\Big)+\cdots, \tag{3.43b}$$

where, from (3.42), the nonlinear fourth-order system governing A and B is

$$A\left(72\pi^2B-4050\mathscr{R}^2+80\pi^4\mathscr{T}-36\pi A_t\right)+72\pi\left(15\mathscr{R}B+B_t\right)$$
$$=45\left(\pi A^2(\pi A+30\mathscr{R})+8\mathscr{R}A_t\right)+3A_{tt}, \tag{3.44a}$$
$$3\left(4\pi\mathscr{L}B+60\mathscr{L}\mathscr{R}A+4\left(\mathscr{L}+75\mathscr{R}^2\right)A_t+45\mathscr{R}A_{tt}\right)+5A_{ttt}$$
$$=\pi\left(9\mathscr{L}A^2+10\left(12\mathscr{R}B_t+B_{tt}\right)\right). \tag{3.44b}$$

The linearised system about $A=0$, $B=0$ is consistent with the quartic equation (3.9).

From (3.43a) we can write h at $x=0.25$ and $x=0.75$ in terms of $A(t)$ and $B(t)$ as follows,

$$h(0.25,t)=1+\left(1+\frac{15}{4}\mathscr{R}\right)A-\frac{A^2}{4}+B+\frac{1}{4}A_t, \tag{3.45a}$$
$$h(0.75,t)=1-\left(1+\frac{45}{4}\mathscr{R}\right)A-\frac{A^2}{4}+B-\frac{3}{4}A_t. \tag{3.45b}$$

We use time-average of h over one period to represent the magnitude of asymmetries

of h about $h=1$. By time-averaging (3.45) we obtain

$$\overline{h(0.25,t)} = 1 + \left(1 + \frac{15}{4}\mathscr{R}\right)\overline{A} - \frac{\overline{A^2}}{4} + \overline{B}, \tag{3.46a}$$

$$\overline{h(0.75,t)} = 1 - \left(1 + \frac{45}{4}\mathscr{R}\right)\overline{A} - \frac{\overline{A^2}}{4} + \overline{B}, \tag{3.46b}$$

where bars denote time-averaged quantities. Applying time-averaging to (3.44b) we get

$$\overline{A^2} = \frac{4}{3}\overline{B} + \frac{20\mathscr{R}}{\pi}\overline{A}. \tag{3.47}$$

Substituting (3.47) into (3.46) we eliminate $\overline{A^2}$ terms

$$\overline{h(0.25,t)} = 1 + \left(1 + \left(\frac{15}{4} - \frac{5}{\pi}\right)\mathscr{R}\right)\overline{A} + \frac{2}{3}\overline{B}, \tag{3.48a}$$

$$\overline{h(0.75,t)} = 1 - \left(1 + \left(\frac{45}{4} + \frac{5}{\pi}\right)\mathscr{R}\right)\overline{A} + \frac{2}{3}\overline{B}. \tag{3.48b}$$

From (3.48) we find that $\overline{h(0.25,t)}$ and $\overline{h(0.75,t)}$ are equal to 1 if $\overline{A}$ and $\overline{B}$ vanish. Since $\overline{A} \gg \overline{B}$ and $\mathscr{R} \ll 1$, the leading approximation of asymmetries are $\overline{A}$ and $-\overline{A}$ for $h(0.25,t)$ and $h(0.75,t)$ respectively.

3.4.2 Steady solutions and their stability

For $\mathscr{L} \gg \mathscr{R}^2 \sim \mathscr{T}$, from (3.44b) where terms involving $\mathscr{L}$ are dominant, we recover

$$B \approx -\frac{15\mathscr{R}A}{\pi} + \frac{3A^2}{4} - \frac{A_t}{\pi}. \tag{3.49}$$

Substituting B and B_t into (3.44a), we have

$$A\left(80\pi^4\mathscr{T} - 20250\mathscr{R}^2 + 9\pi A(\pi A - 180\mathscr{R})\right) = 2520\mathscr{R}A_t + 75A_{tt}. \tag{3.50}$$

This amplitude equation was derived in Chapter 2 for the case $\mathscr{L} = O(1)$. This has a transcritical bifurcation ($\mathrm{TC}_2^{\mathrm{A}}$) for

$$\mathscr{T} = 2025\mathscr{R}^2/8\pi^4 \tag{3.51}$$

and a saddle-node bifurcation (SN^A) at

$$\mathscr{T} = 9315\mathscr{R}^2/8\pi^4, \tag{3.52}$$

both of which are illustrated in Figure 3.1(a). The approximation TC_2^A agrees well with the numericallly predicted TC_2. For $\mathscr{T} < 0$ and $-\mathscr{T} \gg \mathscr{R}^2$, (3.50) is approximately Hamiltonian, with nested periodic orbits confined between $A = 0$ and two steady non-uniform solutions with $80\pi^2\mathscr{T} + 9A^2 = 0$ (Chapter 2). The uniform state $A = 0$ loses stability to a mode-2 equilibrium state as $\mathscr{T}$ increases through the transcritical bifurcation. These bifurcations are independent of $\mathscr{L}$ and so are shared by the full system (3.44). The steady solutions of (3.50) are indicated in the bifurcation diagram in Figure 3.5. We now turn to oscillatory instabilities of these solutions, governed by (3.44).

We can eliminate $\mathscr{R}$ from (3.44) by rescaling as

$$\mathscr{T} = \mathscr{R}^2\hat{\mathscr{T}}, \quad \mathscr{L} = \mathscr{R}^2\hat{\mathscr{L}}, \quad t = \hat{t}/\mathscr{R}, \quad \sigma = \hat{\sigma}\mathscr{R}, \quad A = \mathscr{R}\hat{A}, \quad B = \mathscr{R}^2\hat{B}; \tag{3.53}$$

then (3.44) becomes

$$\begin{aligned}
&\hat{A}\left(72\pi^2\hat{B} - 4050 + 80\pi^4\hat{\mathscr{T}} - 36\pi\hat{A}_{\hat{t}}\right) + 72\pi\left(15\hat{B} + \hat{B}_{\hat{t}}\right) \\
&= 45\left(\pi\hat{A}^2(\pi\hat{A} + 30) + 8\hat{A}_{\hat{t}}\right) + 3\hat{A}_{\hat{t}\hat{t}}, &(3.54a)\\
&3\left(4\pi\hat{\mathscr{L}}\hat{B} + 60\hat{\mathscr{L}}\hat{A} + 4\left(\hat{\mathscr{L}} + 75\right)\hat{A}_{\hat{t}} + 45\hat{A}_{\hat{t}\hat{t}}\right) + 5\hat{A}_{\hat{t}\hat{t}\hat{t}} \\
&= \pi\left(9\hat{\mathscr{L}}\hat{A}^2 + 10\left(12\hat{B}_{\hat{t}} + \hat{B}_{\hat{t}\hat{t}}\right)\right). &(3.54b)
\end{aligned}$$

Using (3.54a), we can eliminate $\hat{A}_{\hat{t}\hat{t}}$ and $\hat{A}_{\hat{t}\hat{t}\hat{t}}$ in (3.54b). Thus, $\hat{A}_{\hat{t}\hat{t}}$ is the highest derivative in (3.54a) and $\hat{B}_{\hat{t}\hat{t}}$ is the highest derivative in (3.54b), allowing (3.54) to be written as a system of four first-order equations, with two parameters $\hat{\mathscr{T}}$ and $\hat{\mathscr{L}}$.

For $\hat{\mathscr{L}} \neq 0$, (3.54) has the equilibrium points $(\hat{A}, \hat{B}) = (0, 0)$ and

$$\left(\hat{A}_\pm, \hat{B}_\pm\right) = \left(\frac{270 \pm \sqrt{10}\sqrt{9315 - 8\pi^4\hat{\mathscr{T}}}}{3\pi}, \frac{5\left(14985 - 8\pi^4\hat{\mathscr{T}} \pm 48\sqrt{10}\sqrt{9315 - 8\pi^4\hat{\mathscr{T}}}\right)}{6\pi^2}\right). \tag{3.55}$$

The equilibria (3.55) are shown in Figure 3.5, with the transcritical bifurcation TC_2^A and the saddle-node bifurcation SN^A arising as predicted in (3.51, 3.52). By calculating the eigenvalues of the Jacobian matrix at these equilibria we find an additional Hopf

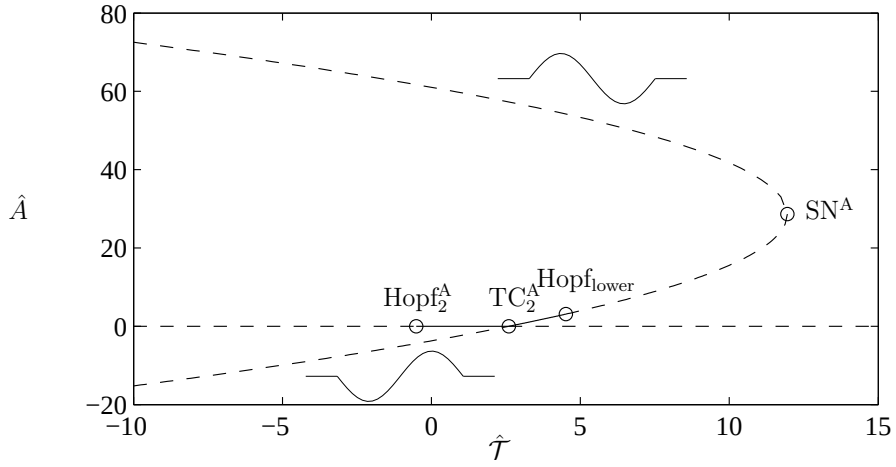

Figure 3.5: Equilibrium curves of (3.54) with $\hat{\mathscr{L}} = \mathscr{L}/\mathscr{R}^2 = 1$, where stable branches are labelled by solid lines and unstable branches labelled by dashed lines. Two insets show mode shapes.

bifurcation point $\mathrm{Hopf}_{\mathrm{lower}}$ for $(\hat{A}_-, \hat{B}_-)$ and (for sufficiently large $\hat{\mathscr{L}}$) two Hopf bifurcation points $\mathrm{Hopf}^1_{\mathrm{upper}}$ and $\mathrm{Hopf}^2_{\mathrm{upper}}$ for $(\hat{A}_+, \hat{B}_+)$. The bifurcation points are shown on Figure 3.6(a). We find that $\mathrm{Hopf}^1_{\mathrm{upper}}$ emerges from SN^{A} at a Takens–Bogdanov bifurcation point when $\hat{\mathscr{L}} = 3375$ and that $\mathrm{Hopf}_{\mathrm{lower}}$ connects to $\mathrm{Hopf}^2_{\mathrm{upper}}$ on SN^{A} at a fold-Hopf bifurcation point when $\hat{\mathscr{L}} = 2^3 \cdot 3 \cdot 5 \cdot 23 \cdot 337 \approx 9.3 \times 10^5$, at which point neutral oscillations have frequency of approximately 2.5×10^6. Details are given in Appendix 3.B. We illustrate the corresponding emergence of $\mathrm{Hopf}_{\mathrm{lower}}$ from SN^{A} in Figure 3.6(b) for $\mathscr{L} = 0.01$. For $\hat{\mathscr{L}} < 3375$, we find that steady stable states exist only for $\hat{\mathscr{T}}$ lying between $\mathrm{Hopf}_2^{\mathrm{A}}$ and $\mathrm{Hopf}_{\mathrm{lower}}$, as illustrated in Figure 3.5.

Being fourth-order, there is potential for (3.54) to exhibit complex dynamics, which we do not aim to describe in detail here. By way of illustration, however, Figure 3.6(c) shows where limit cycles emerging from $\mathrm{Hopf}_2^{\mathrm{A}}$ first undergo a period-doubling bifurcation, while Figure 3.6(d) shows how subsequent period-doublings lead to apparently chaotic dynamics. Our primary interest is in the structure of the oscillations close to $\mathrm{Hopf}_2^{\mathrm{A}}$, which we now investigate in the limit in which $\hat{\mathscr{L}}$ is small. This corresponds to the upper limit of the upper branch in Figure 3.1, where the oscillation frequency is determined primarily by the length of the downstream rigid segment.

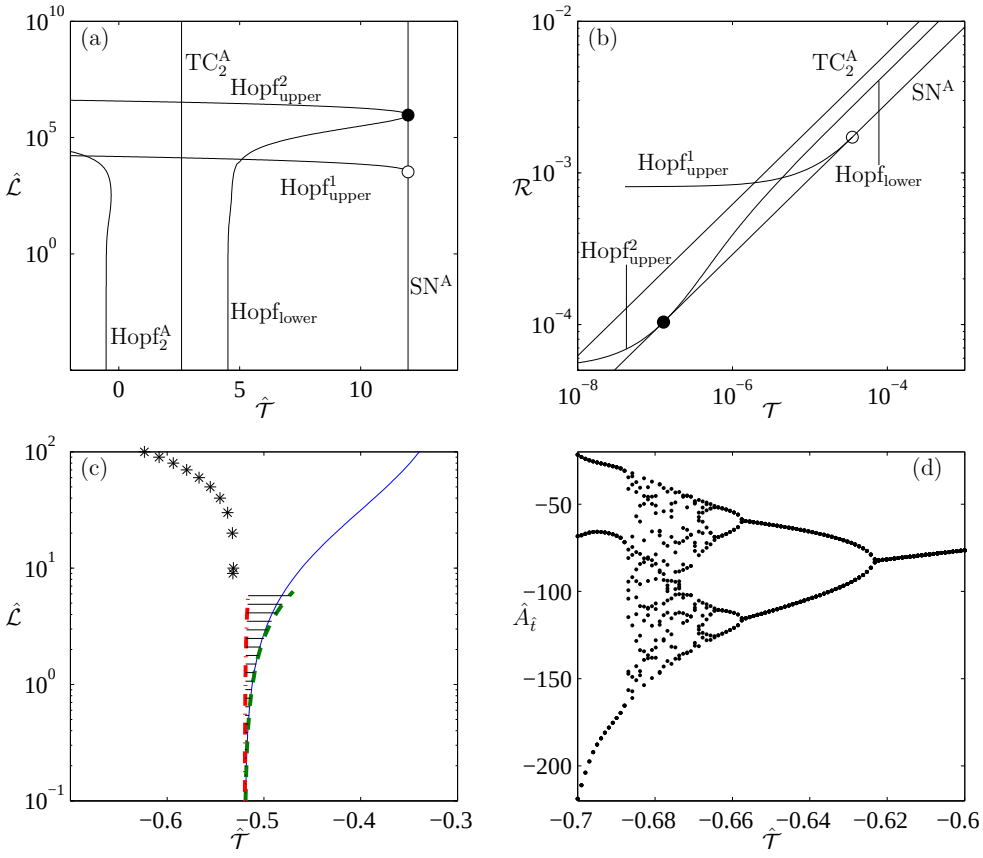

Figure 3.6: (a) Neutral curves of (3.54) in $(\hat{\mathscr{T}}, \hat{\mathscr{L}})$-space. Symbols denote the location of the fold-Hopf point at $\hat{\mathscr{L}} \approx 9.3 \times 10^5$ (solid circle) and the Takens–Bogdanov point at $\hat{\mathscr{L}} = 3375$ (open circle). (b) Neutral curves in $(\mathscr{T}, \mathscr{R})$-space ($\mathscr{T} > 0$) for $\mathscr{L} = 0.01$. (c) Stars represent the onset of period-doubling bifurcations. Solid and dashed lines are the oscillatory neutral curve $\mathrm{Hopf}_2^{\mathrm{A}}$ and its two-term approximation given by (3.56a) respectively. The vertical dash-dotted line represents (3.100). The shaded region illustrates (3.66) for $\hat{\mathscr{L}} \ll 1$, within which oscillations develop sawtooth behaviour. (d) $\hat{A}_{\hat{t}}$ values of 10 iterations of Poincaré maps from (3.54) as $\hat{\mathscr{T}}$ changes from -0.7 to -0.6, where $\hat{\mathscr{L}} = 100$ and the Poincaré section is $\hat{A} = 0, \hat{A}_{\hat{t}} < 0$.

3.4.3 Oscillations arising for small $\hat{\mathscr{L}}$

From (3.10, 3.11), the Hopf_2^{A} curve, plotted on Figure 3.6, and the corresponding frequency can be re-expressed in terms of $\hat{\mathscr{T}}$ and $\hat{\mathscr{L}}$ using (3.53). Then, as $\hat{\mathscr{L}} \to 0$, the two-term approximations are

$$\hat{\mathscr{T}} = -\frac{405}{8\pi^4} + \frac{99\hat{\mathscr{L}}}{128\pi^4} + O(\hat{\mathscr{L}}^2), \tag{3.56a}$$

$$\hat{\sigma} = \pm \mathrm{i}\sqrt{\frac{27\hat{\mathscr{L}}}{8} - \frac{25\hat{\mathscr{L}}^2}{1024} + O(\hat{\mathscr{L}}^3)}. \tag{3.56b}$$

Equation (3.56a) is illustrated in Figure 3.6(c). Recall that the one-term approximations correspond to the asymptotes Upper^{L} and $|\sigma|^{\text{L}}_{\text{upper}}$ in Figure 3.1.

We now simplify (3.54) for small $\hat{\mathscr{L}}$ in the neighbourhood of the Hopf_2^{A} curve. We rescale $\hat{A} = \hat{\mathscr{L}}^{1/2}\tilde{A}$, $\hat{B} = \hat{\mathscr{L}}^{1/2}\tilde{B}$ and introduce two time scales $\{\tilde{t}_1, \tilde{t}_2\} = \{\hat{\mathscr{L}}^{1/2}, \hat{\mathscr{L}}\}\hat{t}$. Then, motivated by (3.56a), we set $\hat{\mathscr{T}} = -405/8\pi^4 + \hat{\mathscr{L}}\tilde{\mathscr{T}}$ and expand

$$\tilde{A} = \tilde{A}_0 + \hat{\mathscr{L}}^{1/2}\tilde{A}_1 + \hat{\mathscr{L}}\tilde{A}_2 + \cdots, \quad \tilde{B} = \tilde{B}_0 + \hat{\mathscr{L}}^{1/2}\tilde{B}_1 + \hat{\mathscr{L}}\tilde{B}_2 + \cdots. \tag{3.57}$$

Under the rescalings and expansions, (3.54) becomes a succession of amplitude equations at increasing orders in $\hat{\mathscr{L}}^{1/2}$. At $O(1)$, we have $15\tilde{A}_0 = 2\pi\tilde{B}_0$ and $15\tilde{A}_{0\tilde{t}_1} = 2\pi\tilde{B}_{0\tilde{t}_1}$, which gives $\tilde{B}_0 = 15\tilde{A}_0/(2\pi)$.

At $O(\hat{\mathscr{L}}^{1/2})$, we have

$$4\pi\left(\pi\tilde{A}_0\tilde{B}_0 + 15\tilde{B}_1 + \tilde{B}_{0\tilde{t}_1}\right) = 5\left(15\pi\tilde{A}_0^2 + 90\tilde{A}_1 + 4\tilde{A}_{0\tilde{t}_1}\right), \tag{3.58a}$$

$$3\left(60\tilde{A}_0 + 4\pi\tilde{B}_0 + 300\tilde{A}_{1\tilde{t}_1} + 45\tilde{A}_{0\tilde{t}_1\tilde{t}_1}\right) = 10\pi\left(12\tilde{B}_{1\tilde{t}_1} + \tilde{B}_{0\tilde{t}_1\tilde{t}_1}\right), \tag{3.58b}$$

which gives

$$\tilde{B}_1 = \frac{9\pi\tilde{A}_0^2 + 90\tilde{A}_1 - 2\tilde{A}_{0\tilde{t}_1}}{12\pi}, \quad \tilde{A}_{0\tilde{t}_1\tilde{t}_1} = -\frac{27}{8}\tilde{A}_0 + \frac{9}{4}\pi\tilde{A}_0\tilde{A}_{0\tilde{t}_1}. \tag{3.59a,b}$$

At $O(\hat{\mathscr{L}})$, we have

$$\begin{aligned}
&4\pi\tilde{A}_0\left(20\pi^3\tilde{\mathscr{T}}-675\tilde{A}_1+18\pi\tilde{B}_1-9\tilde{A}_{0\tilde{t}_1}\right)=\\
&3\Big(15\pi^2\tilde{A}_0^3+2700\tilde{A}_2-24\pi^2\tilde{A}_1\tilde{B}_0-360\pi\tilde{B}_2+120\tilde{A}_{0\tilde{t}_2}-24\pi\tilde{B}_{0\tilde{t}_2}\\
&+120\tilde{A}_{1\tilde{t}_1}-24\pi\tilde{B}_{1\tilde{t}_1}+\tilde{A}_{0\tilde{t}_1\tilde{t}_1}\Big), \qquad (3.60a)\\
&\pi\left(9\tilde{A}_0^2+10\left(12\tilde{B}_{1\tilde{t}_2}+12\tilde{B}_{2\tilde{t}_1}+2\tilde{B}_{0\tilde{t}_1\tilde{t}_2}+\tilde{B}_{1\tilde{t}_1\tilde{t}_1}\right)\right)=\\
&180\tilde{A}_1+12\pi\tilde{B}_1+900\tilde{A}_{1\tilde{t}_2}+12\tilde{A}_{0\tilde{t}_1}+900\tilde{A}_{2\tilde{t}_1}+270\tilde{A}_{0\tilde{t}_1\tilde{t}_2}\\
&+135\tilde{A}_{1\tilde{t}_1\tilde{t}_1}+5\tilde{A}_{0\tilde{t}_1\tilde{t}_1\tilde{t}_1}, \qquad (3.60b)
\end{aligned}$$

which gives

$$\begin{aligned}
\tilde{B}_2=&\Big(-80\pi^4\tilde{\mathscr{T}}\tilde{A}_0-9\pi^2\tilde{A}_0^3+1620\pi\tilde{A}_0\tilde{A}_1+8100\tilde{A}_2-180\tilde{A}_{0\tilde{t}_2}-60\pi\tilde{A}_0\tilde{A}_{0\tilde{t}_1}\\
&-180\tilde{A}_{1\tilde{t}_1}+15\tilde{A}_{0\tilde{t}_1\tilde{t}_1}\Big)/(1080\pi), \qquad (3.61a)\\
\tilde{A}_{0\tilde{t}_1\tilde{t}_2}=&\frac{9\pi\tilde{A}_0^2\left(35-34\pi\tilde{A}_{0\tilde{t}_1}\right)}{5120}+\frac{9\pi\tilde{A}_0\left(\tilde{A}_{0\tilde{t}_2}+\tilde{A}_{1\tilde{t}_1}\right)}{8}\\
&+\frac{\tilde{A}_{0\tilde{t}_1}\left(99-128\pi^4\tilde{\mathscr{T}}-42\pi\tilde{A}_{0\tilde{t}_1}\right)}{2304}-\frac{9\tilde{A}_1\left(3-2\pi\tilde{A}_{0\tilde{t}_1}\right)}{16}-\frac{\tilde{A}_{1\tilde{t}_1\tilde{t}_1}}{2}. \qquad (3.61b)
\end{aligned}$$

Setting $\theta(\tau)=\tilde{A}_0(\tilde{t}_1,\tilde{t}_2)+\hat{\mathscr{L}}^{1/2}\tilde{A}_1(\tilde{t}_1,\tilde{t}_2)$, with $\tilde{t}_1=\tau$ and $\tilde{t}_2=\hat{\mathscr{L}}^{1/2}\tau$, from (3.59*b*, 3.61b), we have, with error $O(\hat{\mathscr{L}})$,

$$\theta_{\tau\tau}+\frac{27}{8}\theta-\frac{9\pi}{4}\theta\theta_\tau=\hat{\mathscr{L}}^{1/2}\left(\frac{63\pi}{2^9}\theta^2+\frac{\left(99-128\pi^4\tilde{\mathscr{T}}\right)}{2^73^2}\theta_\tau-\frac{153\pi^2}{2^85}\theta^2\theta_\tau-\frac{7\pi}{2^63}\theta_\tau^2\right). \qquad (3.62)$$

The leading part of (3.62),

$$\theta_{\tau\tau}+\frac{27}{8}\theta-\frac{9\pi}{4}\theta\theta_\tau=0, \qquad (3.63)$$

is a Liénard equation, which has the trivial solution $\theta_\tau=3/2\pi$. The substitution $\eta(\theta)=\theta_\tau$ leads to

$$\eta\eta_\theta+\frac{27}{8}\theta-\frac{9\pi}{4}\theta\eta=0, \qquad (3.64)$$

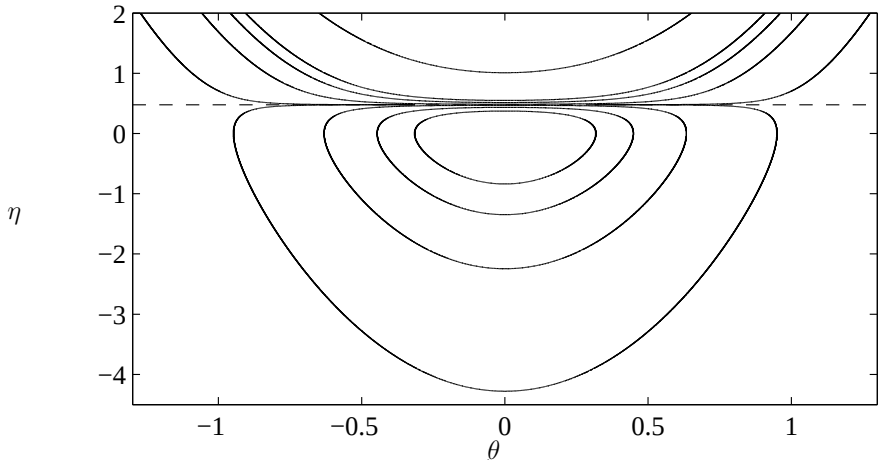

Figure 3.7: The phase portrait of (3.63). The closed orbits (moving inwards) are from (3.65) with $C = 1$, 0.5, 0.3 and 0.2. The open orbits (upwards) are from (3.65) with $C = 1$, 0.5, 0.3, 0.2 and -0.2. The dashed line is $\eta = 3/2\pi$.

which is an Abel equation of the second kind and has solution

$$\theta^2 - \frac{8}{9\pi}\left(\eta + \frac{3}{2\pi}\ln\left|\eta - \frac{3}{2\pi}\right|\right) = C, \tag{3.65}$$

with integral constant C. Since $\theta = \theta(\tau)$, we use $\eta = \eta(\tau)$ in the following. The solution (3.65) represents a closed orbit and an open orbit for $C \geq 4\ln(2\pi/3)/3\pi^2$ (≈ 0.0999) and an open orbit for $C < 4\ln(2\pi/3)/3\pi^2$ (see figure 3.7).

A Mel'nikov analysis (Appendix 3.C) reveals how the forcing terms on the right-hand-side of (3.62) imply stability on particular orbits for different values of $\tilde{\mathscr{T}}$. We confirm numerical evidence that the Hopf$_2$ bifurcation is supercritical and show that a stable limit cycle grows to large amplitude as $\tilde{\mathscr{T}} \to 9/160\pi^4$ from above. Thus for

$$\frac{9\hat{\mathscr{L}}}{160\pi^4} < \hat{\mathscr{T}} + \frac{405}{8\pi^4} < \frac{99\hat{\mathscr{L}}}{128\pi^4}, \quad (\hat{\mathscr{L}} \ll 1) \tag{3.66}$$

a region indicated in Figure 3.6(c), oscillations are approximated by members of the family of closed orbits shown in Figure 3.7. As the oscillations grow in amplitude, they take on a pronounced "sawtooth" structure, with $h(0.25,t) \approx 1 + \mathscr{L}^{1/2}\theta$ rising linearly with time (along $\theta_\tau = 3/2\pi$), then falling abruptly before rising linearly again. Correspondingly the downstream constriction near $x = 0.75$ opens rapidly but closes slowly. We illustrate this behaviour in more detail below through comparison with

PDE simulations. For the sawtooth oscillations we have approximately

$$B = \frac{15\mathscr{R}}{2\pi}A. \tag{3.67}$$

In this case from (3.48) the time-averaged $h(0,25,t)$ and $h(0.75,t)$ are simplified as

$$\overline{h(0.25,t)} = 1 + \left(1 + \frac{15}{4}\mathscr{R}\right)\overline{A}, \tag{3.68}$$

$$\overline{h(0.75,t)} = 1 - \left(1 + \frac{45}{4}\mathscr{R}\right)\overline{A}, \tag{3.69}$$

which means that if $\overline{A} < 0$ ($\overline{A} > 0$) the time-averaged $h-1$ over one period is negative (positive) at $x = 0.25$ and positive (negative) at $x = 0.75$, and the size of the latter is larger than that of the former by $7.5\mathscr{R}|\overline{A}|$. Once parameters $\mathscr{R}$, T and $\mathscr{L}$ are given, $\overline{A}$ can be calculated from (3.44). These asymmetries can be observed qualitatively in Figure 3.8(a) ($\overline{h(0.75,t)} > 1 > \overline{h(0.25,t)}$) and Figure 3.10(a) ($\overline{h(0.75,t)} > 1 \approx \overline{h(0.25,t)}$), suggesting that $\overline{A} < 0$.

3.5 Testing the asymptotic predictions

We now return to the full PDEs (1.26, 1.27) to validate the predictions of the linear and weakly nonlinear analysis (§3.5.1). We then undertake a more stringent test of the one-dimensional model by presenting some simulations of the full two-dimensional Navier–Stokes problem (§3.5.2). In the former case, discrepancies may arise because the parameters $\mathscr{R}$, $\mathscr{T}$ and $\mathscr{L}$ are not sufficiently close to zero; in the latter case, we cannot expect quantitative agreements with the one-dimensional model as the one-dimensional model is derived on the basis of some *ad hoc* assumptions.

3.5.1 One-dimensional simulations

Using the method given in §2.E, we perform numerical simulations of the one-dimensional model (1.26, 1.27) for parameter values near the Hopf_2 and TC_2 bifurcation points, as indicated by the crosses in Figure 3.1(a). We again write $T = T_{20} + \hat{\mathscr{T}}\mathscr{R}^2$, fix $\mathscr{R} = 0.01$ and $\mathscr{L} = 0.01$ and use the initial condition $h = 1 + A_{\mathrm{init}} \sin 2\pi x$ with $A_{\mathrm{init}} = 0.01$.

Figure 3.8 shows, for $\hat{\mathscr{T}} = -0.7$ and -0.75 (the two crosses near $\mathrm{Upper}^{\mathrm{L}}$ in Figure 3.1(a) are almost indistinguishable), that a mode-2 oscillatory instability arises

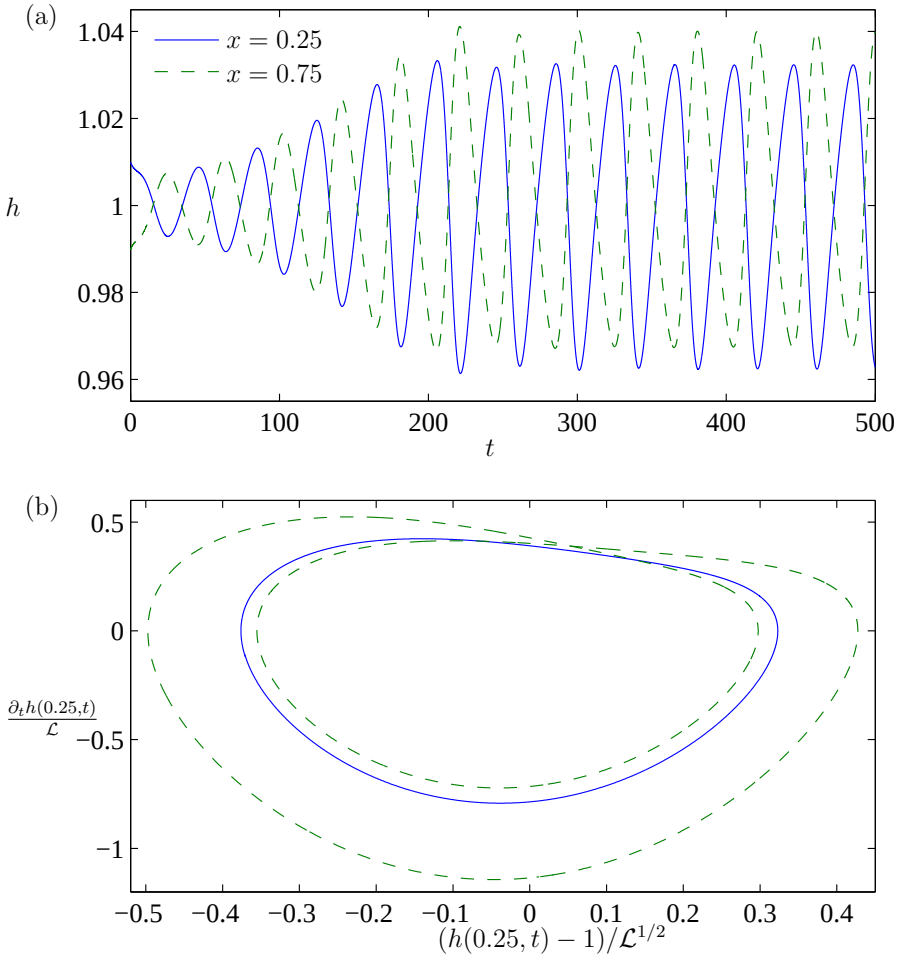

Figure 3.8: Simulations of the one-dimensional model (1.26, 1.27) for $\mathscr{R} = 0.01$ and $\mathscr{L} = 0.01$. (a) The time trace of membrane displacements at $x = 0.25$ and $x = 0.75$ for $\hat{\mathscr{T}} = -0.7$; the out-of-phase motion is characteristic of a mode-2 oscillation. (b) The final limit cycle represented by $h(0.25,t) - 1$ scaled by $\mathscr{L}^{1/2}$ and its time derivative scaled by $\mathscr{L}$ for $\hat{\mathscr{T}} = -0.7$ (solid) and for $\hat{\mathscr{T}} = -0.75$ (dashed).

from the uniform steady state as expected, to yield a sustained mode-2 sawtooth oscillation. The oscillation shown in Figure 3.8(a, b) has period of about 40, which is close to the predicted period 37 of the neutral oscillation at the nearby Hopf bifurcation point (see (3.11)). Slightly decreasing T, we see period doubling in Figure 3.8(b), which agrees qualitatively with the prediction from the fourth-order amplitude equation (3.54) (see Figure 3.6(c)). For these parameter values, $\hat{\mathscr{L}} = 100$ and period-doubling is predicted for $\hat{\mathscr{T}} \approx -0.6236$ via asymptotics (Figure 3.6(c)), whereas the PDE results indicate that it lies in the interval $(-0.75, -0.7)$.

Figure 3.9 shows simulations for parameter values near TC_2 and $\mathrm{Hopf}_{\mathrm{lower}}$ (see the crosses on Figure 3.1(a)). For $\hat{\mathscr{T}} = 5$, linear stability analysis suggests that the uniform steady state should be destabilized by divergent instability (see Figure 3.5, 3.6(a)), which is confirmed by the PDE simulation shown in Figure 3.9(a). The simulation predicts that the uniform steady state finally goes to a mode-2 steady state. In contrast, for $\hat{\mathscr{T}} = 6.4$ in Figure 3.9(b), the uniform state is divergently unstable before going to a small-amplitude oscillation about the mode-2 steady state. Thus the simulations provide evidence for the existence of $\mathrm{Hopf}_{\mathrm{lower}}$, placing it in the range $5 < \hat{\mathscr{T}} < 6.4$, whereas the weakly nonlinear analysis predicts that it lies at $\hat{\mathscr{T}} \approx 4.6343$ for these values of $\mathscr{L}$ and $\mathscr{R}$ (see (3.81)).

3.5.2 Two-dimensional Simulations

In the two-dimensional numerical simulations, we fix $L_1^* = 5$, $L^* = 10$, $L_2^* = 100$ (so that $\mathscr{L} = 0.1$), and $\mathscr{R} = 0.01$. These parameters comfortably satisfy the constraints given in §3.1 for membrane stretching and bending effects to be weak. To investigate the evolution of the system, as in Stewart *et al.* (2010*a*), we firstly slightly perturb the linear external pressure supporting the uniform state, to get a steady state with a slightly deformed membrane shape. Then we use the steady state as the initial condition for the unsteady simulation. We undertook grid convergence studies in order to ensure that predictions were accurate; in order to avoid a grid-scale instability in the downstream segment, for the initial guess we used a coarse structured grid which was then refined adaptively.

For these parameters, we find that a Hopf bifurcation (resembling Hopf_2) is located in the range $0.017 < T < 0.018$, whereas the linear stability analysis of the one-dimensional model predicts that Hopf_2 lies at $T \approx 0.03004$ for these values of $\mathscr{R}$ and $\mathscr{L}$ (Figure 3.1(a)). Decreasing T, sawtooth oscillations are seen when $T = 0.0167$

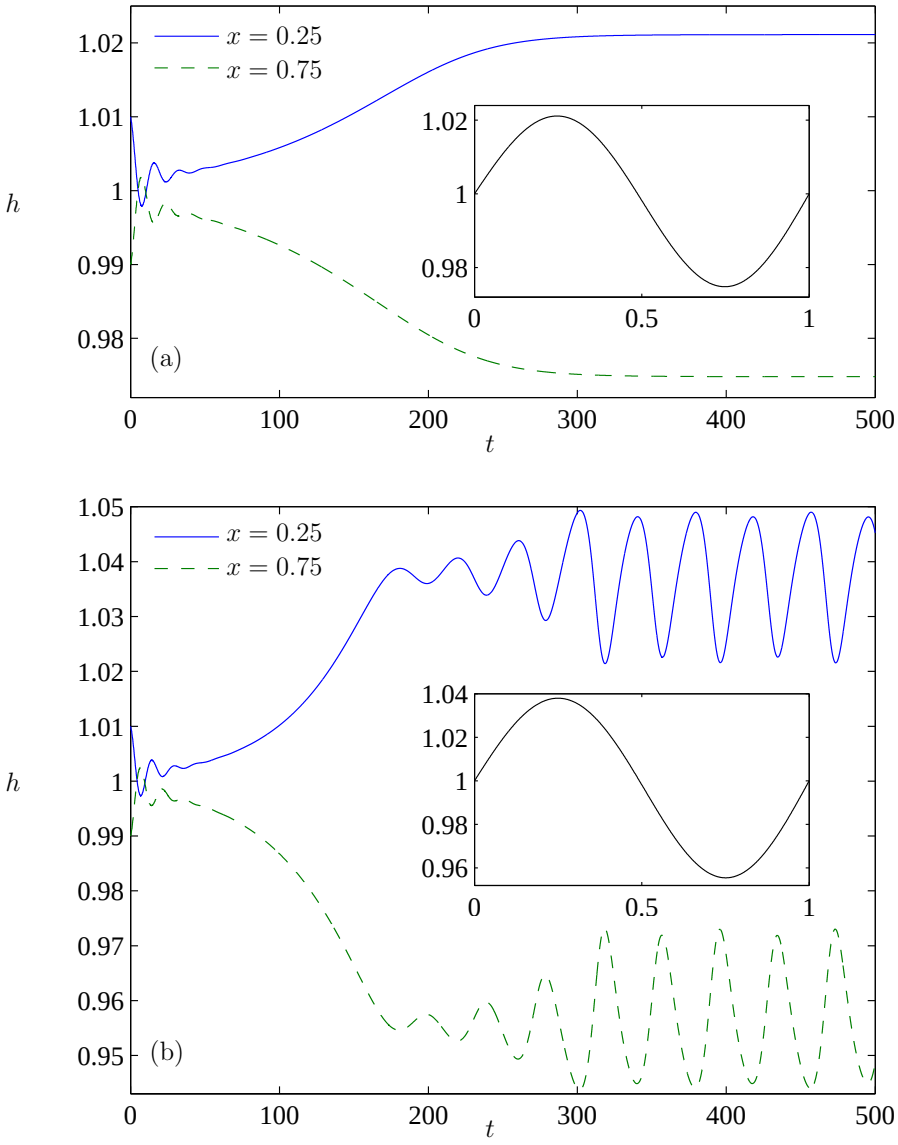

Figure 3.9: Simulations of the one-dimensional model (1.26, 1.27) for $\mathscr{R} = 0.01$ and $\mathscr{L} = 0.01$. The time trace of the membrane displacements at $x = 0.25$ and $x = 0.75$ for $\hat{\mathscr{T}} = 5$ (a) and $\hat{\mathscr{T}} = 6.4$ (b). The insets show the shape of the corresponding mode-2 steady solutions.

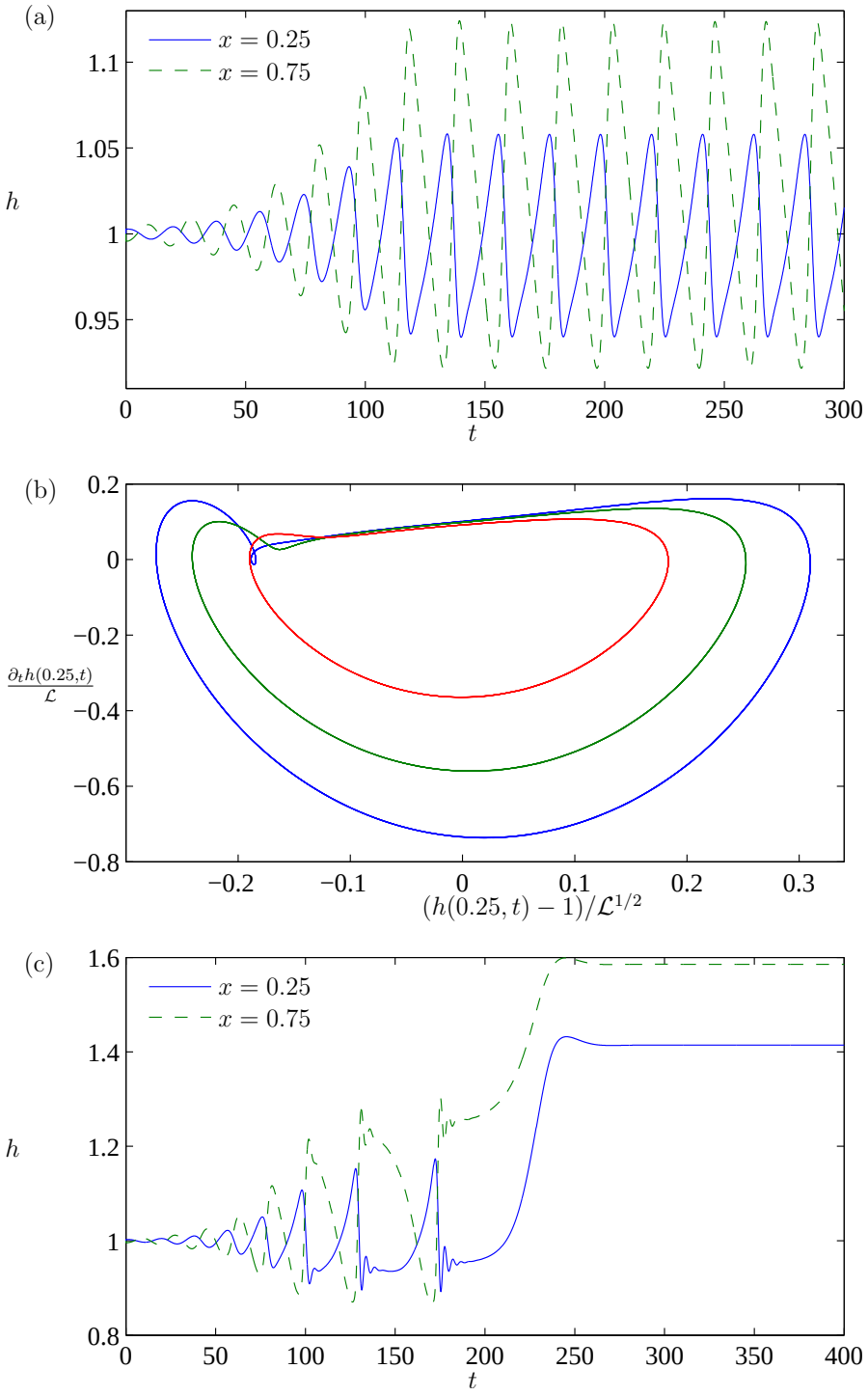

Figure 3.10: two-dimensional simulations for $\mathscr{R} = 0.01$ and $\mathscr{L} = 0.1$. (a) The time trace of the channel width at $x = 0.25$ and $x = 0.75$ for $T = 0.0167$. (b) The final limit cycle for $T = 0.0167$, 0.0165, 0.0164 (with amplitude increasing as T falls). (c) The time trace of the channel width at $x = 0.25$ and $x = 0.75$ for $T = 0.0163$.

(Figure 3.10(a)). The accompanying video illustrates the structure of the internal flow field, which show minimal evidence of flow separation or of disturbance propagating into the downstream segment. The downstream constriction opens within 30% of the total period. Figure 3.10(b) shows that the limit cycle becomes distorted as T decreases further; period doubling was not observed. Instead, as T is reduced to 0.0163, the system goes to a mode-1 (inflated) steady state rather than a stable limit cycle (Figure 3.10(c)). In this example, we can see a few transient sawtooth oscillations increasing in amplitude and period, with "ringing" taking place when the tube opens abruptly at its downstream end.

Figure 3.11 shows similar behaviour to Figure 3.9, but for $T = 0.03$ (resembling the case of $\hat{\mathscr{T}} = 5$) and $T = 0.0315$ (resembling the case of $\hat{\mathscr{T}} = 6.4$), which suggests that the analogue of $\mathrm{Hopf}_{\mathrm{lower}}$ exists in the range $0.03 < T < 0.0315$. We also find a transcricritical bifurcation point resembling TC_2 in the range $0.024 < T < 0.026$, whereas the linear stability analysis of the one-dimensional model predicts that TC_2 lies at $T \approx 0.03071$ for the value of $\mathscr{R}$ (Figure 3.1(a)).

3.6 Discussion

In this chapter, by exploring the one-dimensional model (1.26, 1.27) of an idealised two-dimensional flexible-channel flow system, we have been able to understand in detail the conditions leading to instability, and the role played by the downstream rigid channel. We have explored the neighbourhood of an organising centre in parameter space, in the hope that it presents a microcosm of the broader range of possible behaviour, while still being accessible to asymptotic analysis. The singular point we have investigated is one at which the inviscid problem admits neutrally stable wave-like disturbances; analogous bifurcation points were identified independently by Guneratne & Pedley (2006) using a two-dimensional model based on interactive boundary-layer theory. We have identified three important classes of behaviour: low-frequency transiently growing oscillations (arising along the lower branch of the Hopf_2 curve), that are largely independent of L_2 (see Figure 3.1(b, c)) but are driven by divergent instabilities of nearby saddle points (for details see Chapter 2); a 1:1 resonance (Figure 3.2(b)), mediated by L_2, leading to an abrupt bend in the Hopf_2 curve (see Figure 3.4(c), where the lower branch of the Hopf_2 curve joins the middle branch); and higher-frequency (yet still slow) oscillations that induce a weak sloshing motion in the downstream rigid

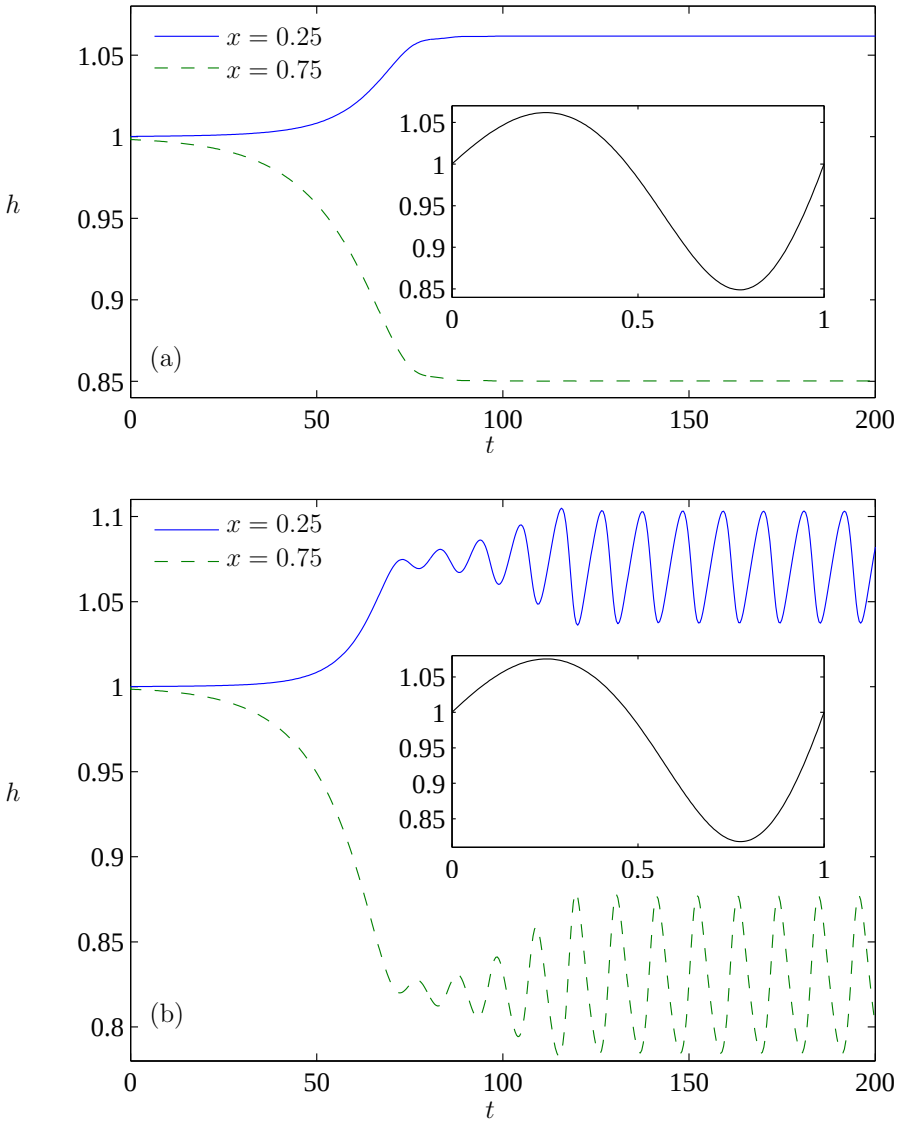

Figure 3.11: two-dimensional simulations for $\mathscr{R} = 0.01$ and $\mathscr{L} = 0.1$. The time trace of the channel width at $x = 0.25$ and $x = 0.75$ for $T = 0.03$ (a) and 0.0315 (b). The insets are the shape of the corresponding mode-2 steady solutions.

tube, arising along the upper branch of the Hopf_2 curve (see Figure 3.4(a)). The downstream sloshing couples two types of membrane deflection (3.43a): a two-humped $\sin(2\pi x)$ disturbance, made slightly asymmetric by viscous and convective inertia effects; and a smaller-amplitude single-humped $(1-\cos(2\pi x))$ mode. These modes have similar frequency and the same wavelength, promoting their interaction. The resulting oscillations arise at moderate Reynolds numbers (Figure 3.1(a)) and can saturate to give stable limit cycles (Figure 3.6(d)).

By performing a three-parameter unfolding of a degenerate bifurcation, we have derived a fourth-order amplitude equation (3.54), itself having two independent parameters, describing behaviour in a neighbourhood of the organising centre, which captures the upper branch of the Hopf_2 curve. We have not attempted to classify the full properties of (3.54), but instead have focussed on a few prominent features. First, in addition to the primary Hopf instability of the uniform state, (3.54) predicts an additional Hopf bifurcation of a non-uniform steady state ($\mathrm{Hopf}_{\mathrm{lower}}$ in figures 3.5 and 3.6(a)). We had previously seen an indication of such a bifurcation (see Figure 2.4), arising even when $L_2 = 1$, indicating that the behaviour we report need not be restricted to the limit $L_2 \gg 1$ but nevertheless involves coupling with the downstream rigid channel. Second, the oscillations arising from the uniform state develop a characteristic sawtooth structure as they grow in amplitude (Figure 3.7), for which the constriction near the downstream end of the membrane opens rapidly but closes slowly. We have validated both of these asymptotic predictions by comparison with numerical simulations of the full one-dimensional model (1.26, 1.27), as shown in figures 3.8 and 3.9.

In a much more stringent test of these predictions, we have also replicated this behaviour using full two-dimensional Navier–Stokes simulations (Figure 3.10). This provides reassuring justification for our detailed study of the one-dimensional model, as well as demonstrating the robustness of its predictions in this regime of parameter space. Because we are investigating small-amplitude low-frequency oscillations in a slender domain, the internal axial velocity profile remains roughly parabolic without undergoing flow reversal; these are conditions under which the one-dimensional model might be expected to provide an effective approximation, even at moderately high Reynolds numbers. However some predictions of the one-dimensional model that are particularly sensitive to parameters, such as a period-doubling cascade (Figure 3.6(a) and 3.8(b)) may not be expected to be robust, particularly as amplitudes grow and timescales fall. Further computational studies, in both two and three dimensions and with a wider range of wall models, will therefore be needed to assess the

wider relevance of the instability mechanisms identified here.

3.A Parametric expansions

3.A.1 Upper Branch

Upon substituting (3.3) and (3.4) into the linearised equations (2.1, 2.2), one homogeneous system and a series of inhomogeneous systems are recovered in succession.

At $O(1)$, we obtain

$$Q_0' = 0, \tag{3.70a}$$
$$6H_0' - 12Q_0' + 5T_{20}H_0''' = 0, \tag{3.70b}$$
$$H_0 = Q_0 = 0, \qquad (x = 0), \tag{3.70c}$$
$$H_0 = 0, \quad (12\mathscr{R}_1 + \sigma_1)Q_0 = 0, \qquad (x = 1). \tag{3.70d}$$

At $O(\varepsilon)$, we obtain

$$Q_1' = -\sigma_1 H_0, \tag{3.71a}$$
$$6H_1' - 12Q_1' + 5T_{20}H_1''' = -(180\mathscr{R}_1 H_0 - 60\mathscr{R}_1 Q_0 - 5\sigma_1 Q_0), \tag{3.71b}$$
$$H_1 = Q_1 = 0, \qquad (x = 0), \tag{3.71c}$$
$$H_1 = 0, \quad (12\mathscr{R}_1 + \sigma_1)Q_1 = -(\sigma_2 Q_0 + \mathscr{L}_2 T_{20}H_0''), \qquad (x = 1). \tag{3.71d}$$

At $O(\varepsilon^2)$, we obtain

$$Q_2' = -(\sigma_2 H_0 + \sigma_1 H_1), \tag{3.72a}$$
$$6H_2' - 12Q_2' + 5T_{20}H_2''' = -(180\mathscr{R}_1 H_1 - 60\mathscr{R}_1 Q_1 - 5\sigma_2 Q_0 - 5\sigma_1 Q_1 + 5\mathscr{T}_2 H_0'''), \tag{3.72b}$$
$$H_2 = Q_2 = 0, \qquad (x = 0), \tag{3.72c}$$
$$H_2 = 0, \quad (12\mathscr{R}_1 + \sigma_1)Q_2 = -(\sigma_3 Q_0 + \sigma_2 Q_1 + \mathscr{L}_2 T_{20}H_1''), \qquad (x = 1). \tag{3.72d}$$

To solve these linear boundary value problems, we obtain the general solutions with four undetermined coefficients; then we substitute the general solutions into boundary conditions, which leads to a linear system of algebraic equations (homogeneous or inhomogeneous) with four unknowns. The resultant algebraic system for (3.70) is under-

determined and its solution exists unconditionally. For the inhomogeneous systems (3.71, 3.72), we impose solvability conditions following the approach given in Chapter 2. The same method is used for the lower and middle branches in the following and the weakly nonlinear analysis for the upper branch in §3.4.

3.A.2 Lower Branch

Upon substituting (3.3) and (3.16) into the linearised equations (2.1, 2.2), one homogeneous system and a series of inhomogeneous systems are recovered in succession.

At $O(1)$, we obtain (3.70a, 3.70b, 3.70c) with

$$H_0 = 0, \quad \sigma_1 Q_0 = 0, \qquad (x = 1). \tag{3.73}$$

At $O(\varepsilon)$, we obtain (3.71a, 3.71c) with

$$6H_1' - 12Q_1' + 5T_{20}H_1''' = 5\sigma_1 Q_0, \tag{3.74a}$$

$$H_1 = 0, \quad \sigma_1 Q_1 = -((12\mathscr{R}_2 + \sigma_2)Q_0 + \mathscr{L}_2 T_{20} H_0''), \qquad (x = 1). \tag{3.74b}$$

At $O(\varepsilon^2)$, we obtain (3.72a, 3.72b, 3.72c) with

$$H_2 = 0, \quad \sigma_1 Q_2 = -(\sigma_3 Q_0 + (12\mathscr{R}_2 + \sigma_2)Q_1 + \mathscr{L}_2 T_{20} H_1''), \qquad (x = 1). \tag{3.75}$$

At $O(\varepsilon^3)$, we obtain

$$Q_3' = -(\sigma_3 H_0 + \sigma_2 H_1 + \sigma_1 H_2), \tag{3.76a}$$

$$6H_3' - 12Q_3' + 5T_{20}H_3''' = -(180\mathscr{R}_2 H_1 - 5\sigma_3 Q_0 - 60\mathscr{R}_2 Q_1 - 5\sigma_2 Q_1 - 5\sigma_1 Q_2 + 5\mathscr{T}_2 H_1'''), \tag{3.76b}$$

$$H_3 = Q_3 = 0, \qquad (x = 0), \tag{3.76c}$$

$$H_3 = 0, \quad \sigma_1 Q_3 = -(\sigma_4 Q_0 + \sigma_3 Q_1 + (12\mathscr{R}_2 + \sigma_2)Q_2 + \mathscr{L}_2 \mathscr{T}_2 H_0'' + \mathscr{L}_2 T_{20} H_2''), \qquad (x = 1). \tag{3.76d}$$

3.A.3 Middle Branch

Upon substituting (3.3) and (3.31) into the linearised equations (2.1, 2.2), one homogeneous system and a series of inhomogeneous systems are recovered in succession. At $O(1)$, we obtain (3.70a, 3.70b, 3.70c, 3.70d). At $O(\varepsilon)$, we obtain (3.71a, 3.71b, 3.71c,

3.71d). At $O(\varepsilon^2)$, we obtain (3.72a, 3.72c, 3.72d) and

$$6H_2' - 12Q_2' + 5T_{20}H_2''' = -(180\mathscr{R}_1 H_1 - 60\mathscr{R}_1 Q_1 - 5\sigma_2 Q_0 - 5\sigma_1 Q_1), \tag{3.77}$$

At $O(\varepsilon^3)$, we obtain (3.76a, 3.76c) and

$$6H_3' - 12Q_3' + 5T_{20}H_3''' = -(180\mathscr{R}_1 H_2 - 60\mathscr{R}_1 Q_2 - 5\sigma_3 Q_0 - 5\sigma_2 Q_1 - 5\sigma_1 Q_2 + 5\mathscr{T}_3 H_0'''), \tag{3.78a}$$

$$H_3 = 0, \quad (12\mathscr{R}_1 + \sigma_1)Q_3 = -(\sigma_4 Q_0 + \sigma_3 Q_1 + \sigma_2 Q_2 + \mathscr{L}_2 T_{20} H_2''), \qquad (x = 1). \tag{3.78b}$$

3.B Hopf bifurcation along the non-uniform branches

For the equilibrium point $(\hat{A}_-, \hat{B}_-)$, the eigenvalue $\hat{\sigma}$ satisfies

$$\begin{aligned} &24\hat{\mathscr{L}} b\left(27\sqrt{10} - b\right) + 48\left(5b\left(297\sqrt{10} - 5b\right) + 63(\hat{\mathscr{L}} - 3375)\right)\hat{\sigma} \\ &+ 10\left(2b\left(297\sqrt{10} - 5b\right) + 9(\hat{\mathscr{L}} - 9354)\right)\hat{\sigma}^2 + 1116\hat{\sigma}^3 + 33\hat{\sigma}^4 = 0, \end{aligned} \tag{3.79}$$

where $b \equiv \sqrt{9315 - 8\pi^4 \hat{\mathscr{T}}}$ (≥ 0). If $\hat{\sigma} = \mathrm{i}\omega$, for ω nonzero and real, then

$$\omega^2 = 2 \cdot 3^2 \cdot 5 \cdot 7 \cdot 1993 - \frac{4b\left(6264\sqrt{10} - 97b\right)}{3} + 2\sqrt{3^4 5^2 7^2 1993^2 + \frac{4b\Delta_{\text{lower}}}{3}}, \tag{3.80}$$

when $(b, \hat{\mathscr{L}})$ lies on the oscillatory neutral curve $\text{Hopf}_{\text{lower}}$

$$\hat{\mathscr{L}} = \frac{3^3 \cdot 5 \cdot 7 \cdot 62233 - 2b\left(3^3 \cdot 7247\sqrt{10} - 3032b\right) + 31\sqrt{3^6 5^2 7^2 1993^2 + 12b\Delta_{\text{lower}}}}{126}, \tag{3.81}$$

where $\Delta_{\text{lower}} \equiv -3^5 \cdot 5 \cdot 7 \cdot 47 \cdot 9833\sqrt{10} + 2b\left(3^2 \cdot 5 \cdot 59 \cdot 36061 - 4b\left(2^4 3^5 13\sqrt{10} - 391b\right)\right)$. When $b = 0$, that is $\hat{\mathscr{T}} = 9315/8\pi^4$, the $\text{Hopf}_{\text{lower}}$ curve merges with the SN^{A} curve at $\hat{\mathscr{L}} = 2^3 \cdot 3 \cdot 5 \cdot 23 \cdot 337$, as seen in Figure 3.6(a), which suggests a fold-Hopf bifurcation. At the fold-Hopf bifurcation point, the equilibrium has a zero eigenvalue and a pair of purely imaginary eigenvalues $\hat{\sigma} = \pm 2^2 3^2 \cdot 5 \cdot 7 \cdot 1993\mathrm{i}$. Figure 3.6(a) also shows that the $\text{Hopf}_{\text{lower}}$ curve lies along $\hat{\mathscr{T}} \approx 4.5129$ when $\hat{\mathscr{L}} \ll 1$.

For the equilibrium point $(\hat{A}_+, \hat{B}_+)$, the eigenvalue $\hat{\sigma}$ satisfies

$$-24\hat{\mathscr{L}}b\left(27\sqrt{10}+b\right)-48\left(5b\left(297\sqrt{10}+5b\right)-63(\hat{\mathscr{L}}-3375)\right)\hat{\sigma}$$
$$-10\left(2b\left(297\sqrt{10}+5b\right)-9(\hat{\mathscr{L}}-9354)\right)\hat{\sigma}^2+1116\hat{\sigma}^3+33\hat{\sigma}^4=0. \tag{3.82}$$

From (3.82), the nonzero frequency ω satisfies

$$\omega^2=2\cdot3^2\cdot5\cdot7\cdot1993+\frac{4b\left(6264\sqrt{10}+97b\right)}{3}\mp2\sqrt{3^45^27^21993^2+\frac{4b\Delta_{\text{upper}}}{3}}, \tag{3.83}$$

on the oscillatory neutral curve $\text{Hopf}^{\text{l}}_{\text{upper}}/\text{Hopf}^{\text{2}}_{\text{upper}}$

$$\hat{\mathscr{L}}=\frac{3^3\cdot5\cdot7\cdot62233+2b\left(3^3\cdot7247\sqrt{10}+3032b\right)\mp31\sqrt{3^65^27^21993^2+12b\Delta_{\text{upper}}}}{126}, \tag{3.84}$$

where $\Delta_{\text{upper}}\equiv-3^5\cdot5\cdot7\cdot47\cdot9833\sqrt{10}+2b\left(3^2\cdot5\cdot59\cdot36061-4b\left(2^43^513\sqrt{10}-391b\right)\right)$. The $\text{Hopf}^{\text{l}}_{\text{upper}}$ curve originates from a Takens–Bogdanov bifurcation point with double zero eigenvalues located on the SN^{A} curve when $\hat{\mathscr{L}}=3375$. The $\text{Hopf}^{\text{2}}_{\text{upper}}$ curve smoothly connects to the $\text{Hopf}_{\text{lower}}$ through the fold-Hopf bifurcation point. These curves are shown in Figure 3.6(a).

3.C Mel'nikov analysis

The perturbed system (3.62) can be rewritten as $(\theta_\tau,\eta_\tau)^{\text{T}}=\boldsymbol{f}(\theta,\eta)+\varepsilon\boldsymbol{g}\left(\theta,\eta,\tilde{\mathscr{T}}\right)$, where $\varepsilon=\hat{\mathscr{L}}^{1/2}(\ll1)$ and

$$\boldsymbol{f}=\left(\eta,\frac{9\pi}{4}\theta\eta-\frac{27}{8}\theta\right)^{\text{T}}, \tag{3.85a}$$
$$\boldsymbol{g}=\left(0,\frac{63\pi}{2^9}\theta^2+\frac{\left(99-128\pi^4\tilde{\mathscr{T}}\right)}{2^73^2}\eta-\frac{153\pi^2}{2^85}\theta^2\eta-\frac{7\pi}{2^63}\eta^2\right)^{\text{T}}. \tag{3.85b}$$

The unperturbed system, i.e. $\varepsilon=0$, has a one-parameter family of periodic orbits $\left(\theta^C(\tau),\eta^C(\tau)\right)$, $C\in(4\ln(2\pi/3)/3\pi^2,\infty)$ and corresponding period T^C.

The Mel'nikov function (Holmes, 1980, Section 2.C) for the perturbed system

along the cycle $\left(\theta^C(\tau),\eta^C(\tau)\right)$ of period T^C of the unperturbed system is given by

$$M(C,\tilde{\mathscr{T}}) = \int_0^{T^C} \exp\left[-\int_0^\tau \nabla\cdot\boldsymbol{f}\left(\theta^C(s),\eta^C(s)\right)\mathrm{d}s\right] \boldsymbol{f}\left(\theta^C(\tau),\eta^C(\tau)\right)\wedge\boldsymbol{g}\left(\theta^C(\tau),\eta^C(\tau),\tilde{\mathscr{T}}\right)\mathrm{d}\tau \tag{3.86}$$

We evaluate the exponential part of the integrand in the Mel'nikov function, using (3.63), as

$$\begin{aligned}\exp\left[-\int_0^\tau \nabla\cdot\boldsymbol{f}\left(\theta^C(s),\eta^C(s)\right)\mathrm{d}s\right] &= \exp\left[-\frac{9\pi}{4}\int_0^\tau \theta^C(s)\mathrm{d}s\right]\\ &= \exp\left[-2\pi\int_0^\tau \frac{\theta^C_{ss}}{2\pi\theta^C_s-3}\mathrm{d}s\right]\\ &= \frac{3-2\pi\theta_\tau(0)}{3-2\pi\theta_\tau(\tau)} = \frac{3-2\pi\eta(0)}{3-2\pi\eta(\tau)}.\end{aligned} \tag{3.87}$$

The wedge product in the integrand is

$$\begin{aligned}\boldsymbol{f}\left(\theta^C(\tau),\eta^C(\tau)\right)\wedge\boldsymbol{g}\left(\theta^C(\tau),\eta^C(\tau),\tilde{\mathscr{T}}\right) =& \eta\Big(\frac{63\pi}{2^9}\theta^2+\frac{\left(99-128\pi^4\tilde{\mathscr{T}}\right)}{2^7 3^2}\eta\\ &-\frac{153\pi^2}{2^8 5}\theta^2\eta-\frac{7\pi}{2^6 3}\eta^2\Big).\end{aligned} \tag{3.88}$$

Then the condition of periodic orbits of the unperturbed system being preserved under small perturbations, $M(C,\tilde{\mathscr{T}})=0$, becomes

$$\int_0^{T^C}\frac{\eta\left(20\eta\left(-99+128\pi^4\tilde{\mathscr{T}}+42\pi\eta\right)+81\pi(-35+34\pi\eta)\theta^2\right)}{23040(-3+2\pi\eta)}\mathrm{d}\tau = 0. \tag{3.89}$$

We denote the intersections of periodic orbits and $\theta=0$ as $(0,\eta_1^C)$ and $(0,\eta_2^C)$, $(0<\eta_1^C<3/2\pi,\ \eta_2^C<0)$. Thus (3.89) gives, using (3.65),

$$\int_{\eta_1^C}^{\eta_2^C} F_1(\eta,C)\mathrm{d}\eta + \tilde{\mathscr{T}}\int_{\eta_1^C}^{\eta_2^C} F_2(\eta,C)\mathrm{d}\eta = 0, \tag{3.90}$$

where

$$F_1 = \frac{\eta\left(\pi(4\eta(375-274\pi\eta)+27C\pi(35-34\pi\eta))+36(35-34\pi\eta)\ln\left(\frac{3}{2\pi}-\eta\right)\right)}{2880(3-2\pi\eta)^2\sqrt{\pi(9C\pi+8\eta)+12\ln\left(\frac{3}{2\pi}-\eta\right)}}, \tag{3.91a}$$

$$F_2 = -\frac{8\pi^5\eta^2}{27(3-2\pi\eta)^2\sqrt{\pi(9C\pi+8\eta)+12\ln\left(\frac{3}{2\pi}-\eta\right)}}. \tag{3.91b}$$

As $C \to 4\ln(2\pi/3)/3\pi^2$ and $\eta_{1,2}^C \to 0$, we have

$$\eta_{1,2}^C \approx \pm\frac{3\sqrt{3\pi^2C+4\ln\frac{3}{2\pi}}}{2\sqrt{2}\pi}, \tag{3.92}$$

$$F_1 \approx \frac{11\pi\eta^2}{432\sqrt{3\left(3\pi^2C+4\ln\frac{3}{2\pi}\right)}}, \quad F_2 \approx -\frac{8\pi^5\eta^2}{243\sqrt{3\left(3\pi^2C+4\ln\frac{3}{2\pi}\right)}}. \tag{3.93}$$

Thus, the condition (3.90) for small-amplitude orbits approximately is $\tilde{\mathscr{T}} = 99/128\pi^4 (\approx 0.0079)$, consistent with (3.56a).

For large C, numerical evaluation of the integrals in (3.90) is difficult. In this case, the unperturbed closed orbit in Figure 3.7 can be divided into two parts, which approximately are

$$\eta_{\text{upper}} = \frac{3}{2\pi} - \exp\left[-\frac{3}{4}\pi^2\left(C-\theta^2\right)\right], \qquad \eta_{\text{lower}} = -\frac{9}{8}\pi\left(C-\theta^2\right). \tag{3.94}$$

Thus (3.89) gives, using $\eta\,\mathrm{d}\tau = \mathrm{d}\theta$,

$$I_{\text{upper}} + I_{\text{lower}} = 0, \tag{3.95}$$

with

$$I_{\text{upper}} = \int_{\theta_1}^{\theta_2} \frac{20\eta_{\text{upper}}\left(-99+128\pi^4\tilde{\mathscr{T}}+42\pi\eta_{\text{upper}}\right)+81\pi(-35+34\pi\eta_{\text{upper}})\theta^2}{23040(-3+2\pi\eta_{\text{upper}})}\mathrm{d}\theta, \tag{3.96}$$

$$I_{\text{lower}} = \int_{\theta_2}^{\theta_1} \frac{20\eta_{\text{lower}}\left(-99+128\pi^4\tilde{\mathscr{T}}+42\pi\eta_{\text{lower}}\right)+81\pi(-35+34\pi\eta_{\text{lower}})\theta^2}{23040(-3+2\pi\eta_{\text{lower}})}\mathrm{d}\theta. \tag{3.97}$$

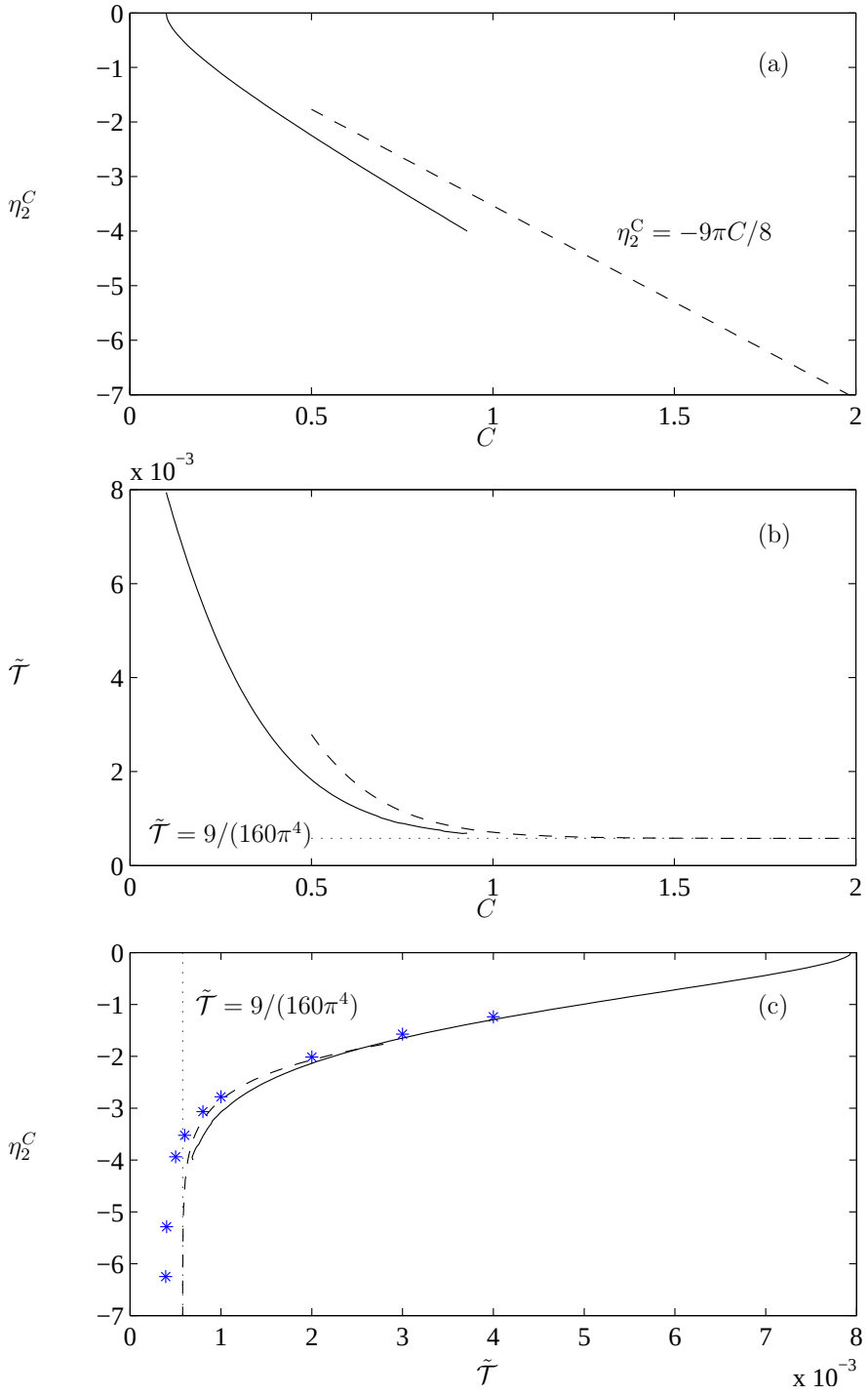

Figure 3.12: Relations between η_2^C, C and $\tilde{\mathcal{T}}$ in (3.90). The solid line is from (3.90) as η_2^C decreases from 0 to -4 and the dashed line is from (3.94) (a) and from (3.95) (b) as C increases from 0.5 to 2. The dotted line is the asymptote (3.100). Eliminating C, the relation between η_2^C and $\tilde{\mathcal{T}}$ is given in (c), in which the stars denote results from the fourth-order system (3.54) with $\hat{\mathscr{L}} = 0.4$.

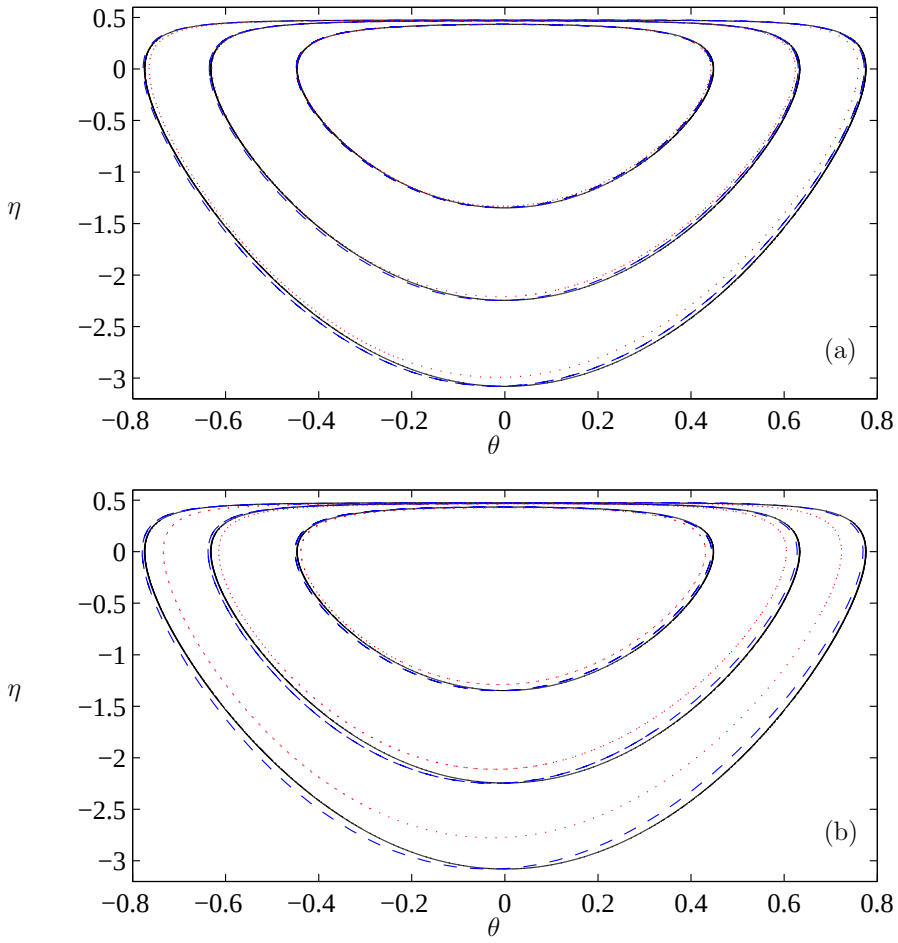

Figure 3.13: Contours from (3.65) (solid) and limit cycles from (3.62) (dashed) and (3.54) (dotted) with $C = 0.3$, 0.5 and 0.7 (increasing outwards) and corresponding respectively to $\tilde{\mathscr{T}} = 0.0038$, 0.0018 and 0.0010, where $\hat{\mathscr{L}} = 0.1$ (a) and 0.4 (b).

For the leading-order approximation, $\theta_{1,2} = \mp\sqrt{C}$, which gives

$$I_{\text{upper}} = \frac{1}{11520\pi^{5/2}}\left(\sqrt{C\pi}\left(432+270\pi+459C\pi^3+1280\pi^5\tilde{\mathscr{T}}\right)-280\sqrt{3}\pi^{3/2}\mathrm{D}_+\left[\frac{1}{2}\sqrt{3C\pi}\right]\right.$$
$$\left.+4\sqrt{3}\exp\left[\frac{3C\pi^2}{4}\right]\left(9-160\pi^4\tilde{\mathscr{T}}\right)\operatorname{erf}\left[\frac{1}{2}\sqrt{3C\pi}\right]\right), \tag{3.98}$$

$$I_{\text{lower}} = \frac{1}{4320\pi^2\sqrt{4+3C\pi^2}}\left(3\pi\sqrt{C\left(4+3C\pi^2\right)}\left(27+18C\pi^2+160\pi^4\tilde{\mathscr{T}}\right)\right.$$
$$\left.+2\sqrt{3}\left(27+54C\pi^2+160\pi^4\tilde{\mathscr{T}}\right)\ln\left[1+\frac{1}{2}\pi\left(3C\pi-\sqrt{3}\sqrt{C\left(4+3C\pi^2\right)}\right)\right]\right), \tag{3.99}$$

where $\mathrm{D}_+(x)$ is the Dawson integral $\exp[-x^2]\int_0^x \exp[t^2]\mathrm{d}t$ and $\operatorname{erf}(x)$ is the error function. For large C, the dominant part of (3.89) gives

$$\tilde{\mathscr{T}} = \frac{9}{160\pi^4}(\approx 0.000577), \tag{3.100}$$

(see Figure 3.12).

As $\eta_{1,2}^C$ increases from zero, we can use (3.90) to numerically evaluate $\tilde{\mathscr{T}}$ for the existence of a limit cycle in the perturbed system (3.62), as seen in Figure 3.12. Because $\tilde{T}$ falls as C increases, we infer that the Hopf bifurcation is supercritical. In Figure 3.13, it is observed that limit cycles predicted from the Mel'nikov analysis agree well with the fourth-order amplitude equations (3.54) and the second-order asymptotics (3.62). Interestingly, the oscillation grows to large amplitude at finite $\tilde{\mathscr{T}}$, a prediction supported by solutions of the fourth-order system (3.54). When $\tilde{\mathscr{T}}$ falls sufficiently below $9/160\pi^4$, the limit cycle of (3.54) is destroyed and the solution diverges; this can be explained by assuming $\hat{T}+405/8\pi^4 \sim O(\hat{\mathscr{L}}^{1/2})$, in which case the term $\tilde{\mathscr{T}}\theta_\tau$ in (3.62) is promoted to leading order, turning the limit cycles in Figure 3.7 into divergent spirals. Our simulations indicates that there exists a critical value of $\hat{\mathscr{L}}$ between 1 and 10, above which the limit cycle diverges after a period doubling cascade but below which no period doubling appears before the limit cycle diverges.

Chapter 4

Highly-collapsed solutions

As described in §2.4, the system (1.26, 1.27) can allow steady and unsteady large-amplitude solutions. In this chapter we study the highly-collapsed configurations for high Reynolds number and focus on the turning point near $T = 0.2$ of Figure 2.4(c). By dividing the collapsible segment of the channel into three parts (see Figure 4.1), we first obtain the leading-order approximation of the large-amplitude solutions by employing the method of matched asymptotic expansions, similar to the work of Jensen (1998). In this approximation the region II solution has its shape determined by an inertia/tension balance (4.24) but viscous dissipation in the constriction (4.41e) still plays a dominant role. Then from the leading-order approximations we deduce a third-order system governing the temporal variations of the approximations. We also analyse the linear stability of the steady solutions of the third-order system.

4.1 Transformation

Here we study (1.26, 1.27) with small $\mathscr{R}$ ($\ll 1$). We scale T and L_2 by $\mathscr{R}$ using

$$T = \frac{\mathscr{T}}{\mathscr{R}}, \quad L_2 = \frac{\mathscr{L}}{\mathscr{R}}, \tag{4.1}$$

where $\mathscr{T}, \mathscr{L} = O(1)$. Thus, the system becomes

$$h_t + q_x = 0, \tag{4.2a}$$

$$\mathscr{R}\left(q_t + \frac{6}{5}\left(\frac{q^2}{h}\right)_x\right) = \mathscr{T} h h_{xxx} + 12\mathscr{R}^2\left(h - \frac{q}{h^2}\right), \tag{4.2b}$$

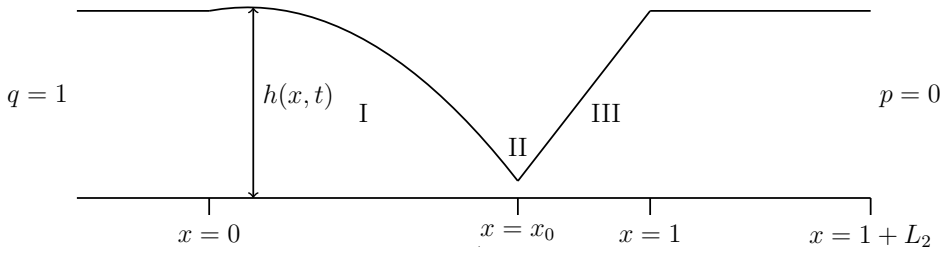

Figure 4.1: Schematic of large-amplitude solution of (1.26, 1.27).

with boundary conditions

$$h=1, \quad q=1, \qquad (x=0), \tag{4.3a}$$

$$h=1, \quad \mathscr{T}h_{xx}=-(12\mathscr{R}(q-1)+q_t)\mathscr{L}, \qquad (x=1). \tag{4.3b}$$

As illustrated in figure 4.1, we divide the interval $[0,1]$ into three parts: (I) $0\le x<x_0$ and $x_0-x=O(1)$, (II) $x-x_0=O(\mathscr{R})$ and (III) $x_0<x\le 1$ and $x-x_0=O(1)$. We assume that h is lowest at $x=x_0(t)$. The overlap regions between I and II and between II and III are $\mathscr{R}\ll x_0-x\ll 1$ and $\mathscr{R}\ll x-x_0\ll 1$, respectively.

In region I, we make expansions as

$$h=h_{10}+O(\mathscr{R}), \quad q=q_{10}+O(\mathscr{R}), \tag{4.4}$$

then the dominant part of (4.2) is

$$h_{10t}+q_{10x}=0, \tag{4.5a}$$

$$h_{10xxx}=0, \tag{4.5b}$$

with boundary conditions

$$h_{10}=1, \quad q_{10}=1, \qquad (x=0). \tag{4.6}$$

In region II, we enlarge h and stretch x using

$$h=\mathscr{R}H(\xi,t), \quad x=x_0+\mathscr{R}\xi, \tag{4.7}$$

where $H = O(1)$ and $\xi = O(1)$, and write

$$q = Q(\xi, t). \tag{4.8}$$

Thus (4.2) is transformed to

$$\mathscr{R}^2 H_t + Q_\xi = 0, \tag{4.9a}$$

$$\mathscr{R}^2 Q_t + \frac{6}{5}\left(\frac{Q^2}{H}\right)_\xi = \mathscr{T} H H_{\xi\xi\xi} + 12\mathscr{R}\left(\mathscr{R}^3 H - \frac{q}{H^2}\right). \tag{4.9b}$$

We expand using

$$H = H_0 + O(\mathscr{R}), \quad Q = Q_0 + O(\mathscr{R}), \tag{4.10}$$

then the dominant part of (4.9) is

$$Q_{0\xi} = 0, \tag{4.11a}$$

$$\frac{6}{5}\left(\frac{Q_0^2}{H_0}\right)_\xi = \mathscr{T} H_0 H_{0\xi\xi\xi}, \tag{4.11b}$$

so $Q_0 = Q_0(t)$. We note that (4.11b) admits solutions satisfying $H_0(\xi, t) = H_0(-\xi, t)$.

In region III, we make expansions as

$$h = h_{30} + O(\mathscr{R}), \quad q = q_{30} + O(\mathscr{R}), \tag{4.12}$$

then the dominant part of (4.2) is

$$h_{30t} + q_{30x} = 0, \tag{4.13a}$$

$$h_{30xxx} = 0, \tag{4.13b}$$

with boundary conditions

$$h_{30} = 1, \quad \mathscr{T} h_{30xx} = -q_{30t}\mathscr{L}, \qquad (x = 1). \tag{4.14}$$

4.2 Leading-order solutions

4.2.1 Region III

We first investigate solution in region III. From $h = \mathscr{R}H$, we have $h_x = H_\xi$. Matching h and h_x in the overlap region between II and III, we have

$$\lim_{x\to x_0^+} h_{30}(x,t) = 0, \tag{4.15}$$

$$\lim_{x\to x_0^+} h_{30x}(x,t) = \lim_{\xi\to+\infty} H_{0\xi}(\xi,t). \tag{4.16}$$

Similarly matching q in the overlap region between II and III, we have

$$\lim_{x\to x_0^+} q_{30}(x,t) = \lim_{\xi\to+\infty} Q_0(\xi,t) \equiv Q_0(t). \tag{4.17}$$

Thus, (4.13b), (4.14) and (4.15) have solution

$$h_{30} = (x-x_0)\left(\frac{1}{1-x_0} + \frac{\mathscr{L}(1-x)Q_{1t}}{2\mathscr{T}}\right), \quad (x_0 < x \le 1) \tag{4.18}$$

where $Q_1(t) = q_{30}(1,t)$, so that (4.16) becomes

$$\lim_{\xi\to+\infty} H_{0\xi}(\xi,t) = \frac{1}{1-x_0} + \frac{\mathscr{L}(1-x_0)Q_{1t}}{2\mathscr{T}} \tag{4.19}$$

Expressed as the outer limit of the solution in region II, (4.18) and (4.19) give

$$H_0 \sim \left(\frac{1}{1-x_0} + \frac{\mathscr{L}(1-x_0)Q_{1t}}{2\mathscr{T}}\right)\xi, \tag{4.20}$$

in the overlap region between II and III.

Integrating (4.13a) from x_0 to 1, using

$$\int_{x_0}^1 h_{30t}\mathrm{d}x = \frac{\partial}{\partial t}\left(\int_{x_0}^1 h_{30}\mathrm{d}x\right) + x_{0t}\lim_{x\to x_0^+} h_{30}(x,t) = \frac{\partial}{\partial t}\left(\int_{x_0}^1 h_{30}\mathrm{d}x\right), \tag{4.21}$$

$$\int_{x_0}^1 q_{30x}\mathrm{d}x = q_{30}(1,t) - \lim_{x\to x_0^+} q_{30}(x,t) = Q_1(t) - Q_0(t), \tag{4.22}$$

we have

$$Q_0 - Q_1 = \left[\frac{1-x_0}{2} + \frac{\mathscr{L}(1-x_0)^3 Q_{1t}}{12\mathscr{T}}\right]_t, \tag{4.23}$$

4.2.2 Region II

Next, we consider the solution in region II. Integrating for ξ once, noting from (4.20) that $H_{0\xi\xi} \to 0$ as $\xi \to \infty$, (4.11b) gives

$$H_{0\xi\xi} = \frac{3Q_0^2}{5\mathscr{T}H_0^2}. \tag{4.24}$$

Due to the symmetry of H_0 about $\xi = 0$, then $H_{0\xi}(0,t) = 0$, and we have

$$H_{0\xi}^2 = \frac{6Q_0^2}{5\mathscr{T}}\left(\frac{1}{H_{00}} - \frac{1}{H_0}\right), \tag{4.25}$$

where $H_{00}(t) = H_0(0,t)$. In the overlap region between II and III, from (4.20), we have

$$\frac{6Q_0^2}{5\mathscr{T}H_{00}} = \left(\frac{1}{1-x_0} + \frac{\mathscr{L}(1-x_0)Q_{1t}}{2\mathscr{T}}\right)^2, \tag{4.26}$$

due to $1/H_0 \to 0$ as $\xi \to \infty$ in the overlap region.

Then writing $H_0 = H_{00}\tilde{H}_0(\tilde{\xi},t)$, $\xi = (5\mathscr{T}H_{00}^3/6Q_0^2)^{1/2}\tilde{\xi}$, we have

$$\tilde{H}_{0\tilde{\xi}}^2 = 1 - \frac{1}{\tilde{H}_0}, \quad \tilde{H}_0(0,t) = 1; \tag{4.27}$$

the implicit solution of (4.27) is

$$\tilde{\xi} = \pm\left(\sqrt{\tilde{H}_0(\tilde{H}_0-1)} + \ln\left(\sqrt{\tilde{H}_0} + \sqrt{\tilde{H}_0-1}\right)\right). \tag{4.28}$$

It follows (for later reference) that

$$\int_{-\infty}^{+\infty} \frac{\mathrm{d}\xi}{H_0^3} = I\sqrt{\frac{5\mathscr{T}}{6Q_0^2H_{00}^3}}, \tag{4.29}$$

where

$$I=\int_{-\infty}^{+\infty}\frac{\mathrm{d}\tilde{\xi}}{\tilde{H}_0^3}=2\int_0^{+\infty}\frac{\mathrm{d}\tilde{\xi}}{\tilde{H}_0^3}=2\int_1^{+\infty}\frac{\tilde{\xi}_{\tilde{H}_0}\mathrm{d}\tilde{H}_0}{\tilde{H}_0^3}=\frac{8}{3}. \tag{4.30}$$

4.2.3 Region I

Finally, we present the solution in region I. In the overlap region between I and II, we have

$$\lim_{x\to x_0^-}h_{10}(x,t)=0, \tag{4.31}$$

$$\lim_{x\to x_0^-}h_{10x}(x,t)=\lim_{\xi\to-\infty}H_{0\xi}=-\lim_{\xi\to+\infty}H_{0\xi}=-\left(\frac{1}{1-x_0}+\frac{\mathscr{L}(1-x_0)Q_{1t}}{2\mathscr{T}}\right). \tag{4.32}$$

Similarly matching q in overlap region between I and II, we have

$$\lim_{x\to x_0^-}q_{10}(x,t)=\lim_{\xi\to-\infty}Q_0(\xi,t)=Q_0(t). \tag{4.33}$$

Thus, from (4.5b), (4.6), (4.31) and (4.32), we have

$$h_{10}=\frac{(x-x_0)\left(2\mathscr{T}\left(-x+x_0+2xx_0-x_0^2\right)+\mathscr{L}x(-1+x_0)^2x_0Q_{1t}\right)}{2\mathscr{T}(-1+x_0)x_0^2}. \tag{4.34}$$

Integrating (4.5a) from 0 to x_0, using

$$\int_0^{x_0}h_{10t}\mathrm{d}x=\frac{\partial}{\partial t}\left(\int_0^{x_0}h_{10}\mathrm{d}x\right)-x_{0t}\lim_{x\to x_0^-}h_{10}(x,t)=\frac{\partial}{\partial t}\left(\int_0^{x_0}h_{10}\mathrm{d}x\right), \tag{4.35}$$

$$\int_0^{x_0}q_{10x}\mathrm{d}x=\lim_{x\to x_0^-}q_{10}(x,t)-q_{10}(0,t)=Q_0(t)-1, \tag{4.36}$$

we have

$$1-Q_0=\left[\frac{(2-x_0)x_0}{6(1-x_0)}+\frac{\mathscr{L}(1-x_0)x_0^2Q_{1t}}{12\mathscr{T}}\right]_t. \tag{4.37}$$

Thus we have two mass conservation conditions (4.23, 4.37) and the matching condition (4.26) for the four unknowns Q_0, Q_1, x_0, H_{00}. One further condition is needed to close the system.

4.3 Energy balance

The energy budget (1.32) for the flow in $0 \le x \le 1+L_2$ can be written as

$$\mathscr{K} + \mathscr{E} = \mathscr{F} + \mathscr{P} - \mathscr{D}, \tag{4.38}$$

where

$$\mathscr{K} = \frac{3}{5}\frac{\partial}{\partial t}\left(\int_0^1 \frac{q^2}{h}\mathrm{d}x + q(1,t)^2 L_2\right), \tag{4.39a}$$

$$\mathscr{F} = \frac{18}{25}(1-q(1,t)^3), \tag{4.39b}$$

$$\mathscr{P} = \frac{6}{5}p(0,t), \tag{4.39c}$$

$$\mathscr{E} = \frac{6}{5}\int_0^1 h_t p\,\mathrm{d}x, \tag{4.39d}$$

$$\mathscr{D} = \frac{72\mathscr{R}}{5}\left(\int_0^1 \frac{q^2}{h^3}\mathrm{d}x + q(1,t)^2 L_2\right) + \frac{3}{25}\int_0^1 \frac{q^2 q_x}{h^2}\mathrm{d}x. \tag{4.39e}$$

with

$$p = 12(L_2+1-x)\mathscr{R} - Th_{xx}, \qquad (0<x<1). \tag{4.40}$$

The dominant contributions to energy balance at order $O(1/\mathscr{R})$ are

$$\mathscr{K} \approx \frac{3\mathscr{L}}{5\mathscr{R}}\left(q(1,t)^2\right)_t \approx \frac{3\mathscr{L}}{5\mathscr{R}}\left(Q_1^2\right)_t, \tag{4.41a}$$

$$\mathscr{F} \approx 0, \tag{4.41b}$$

$$\begin{aligned}\mathscr{P} &\approx -\frac{6\mathscr{T}}{5\mathscr{R}}h_{xx}(0,t) \approx -\frac{6\mathscr{T}}{5\mathscr{R}}h_{10xx}(0,t)\\ &= -\frac{6\mathscr{T}}{5\mathscr{R}}\left(\frac{2(-1+2x_0)}{(-1+x_0)x_0^2} + \frac{\mathscr{L}(-1+x_0)Q_{1t}}{\mathscr{T}x_0}\right),\end{aligned} \tag{4.41c}$$

$$\begin{aligned}\mathscr{E} &\approx \frac{3\mathscr{T}}{5\mathscr{R}}\left(\int_{\mathrm{I+III}} h_x^2\mathrm{d}x\right)_t\\ &= \frac{3\mathscr{T}}{5\mathscr{R}}\left(\frac{4-7x_0+4x_0^2}{3(1-x_0)^2x_0} - \frac{\mathscr{L}(1-2x_0)Q_{1t}}{3\mathscr{T}} + \frac{\mathscr{L}^2(1-x_0)^2Q_{1t}^2}{12\mathscr{T}^2}\right)_t,\end{aligned} \tag{4.41d}$$

$$\mathscr{D} \approx \frac{72\mathscr{R}}{5}\int_{\mathrm{II}}\frac{q^2}{h^3}\mathrm{d}x \approx \frac{72Q_0^2}{5\mathscr{R}}\int_{-\infty}^{+\infty}\frac{\mathrm{d}\xi}{H_0^3} = \frac{192}{5\mathscr{R}}\sqrt{\frac{5\mathscr{T}Q_0^2}{6H_{00}^3}}. \tag{4.41e}$$

Thus, the energy budget gives

$$\left[\mathscr{L}Q_1^2+\mathscr{T}\left(\frac{4-7x_0+4x_0^2}{3(1-x_0)^2x_0}-\frac{\mathscr{L}(1-2x_0)Q_{1t}}{3\mathscr{T}}+\frac{\mathscr{L}^2(1-x_0)^2Q_{1t}^2}{12\mathscr{T}^2}\right)\right]_t$$
$$+2\mathscr{T}\left(\frac{2(1-2x_0)}{(1-x_0)x_0^2}-\frac{\mathscr{L}(1-x_0)Q_{1t}}{\mathscr{T}x_0}\right)+64\sqrt{\frac{5\mathscr{T}Q_0^2}{6H_{00}^3}}=0. \tag{4.42}$$

Equations (4.23), (4.26), (4.37) and (4.42) constitute a system for $Q_1(t)$, $Q_0(t)$, $x_0(t)$ and $H_{00}(t)$. Once the system is solved, (4.18) and (4.34) can be used as asymptotic solutions of (1.26) and (1.27).

4.4 Steady solutions

For the steady case, the system gives

$$Q_1=Q_0=1, \tag{4.43a}$$
$$H_{00}=\frac{6(1-x_0)^2}{5\mathscr{T}}, \tag{4.43b}$$
$$\frac{1-2x_0}{x_0^2}+\frac{100\mathscr{T}}{9(1-x_0)^2}=0 \tag{4.43c}$$

and the asymptotic solutions of (1.26, 1.27) are

$$q=1, \tag{4.44a}$$
$$h=\begin{cases}\dfrac{(x-x_0)(x-x_0-2xx_0+x_0^2)}{(1-x_0)x_0^2}, & 0\le x<x_0,\\ \dfrac{x-x_0}{1-x_0}, & x_0<x\le 1.\end{cases} \tag{4.44b}$$

It suggests that the steady solution with one sharp constriction is only determined asymptotically by $\mathscr{T}$ $(=\mathscr{R}T)$.

From Figure 4.2, we can see good agreement between asymptotic and numerical steady solutions for small $\mathscr{R}$. From (4.43c), we derive that $1/2<x_0<1$ due to $\mathscr{T}>0$, and find that two steady solutions coalesce when

$$\mathscr{T}=\frac{9(5\sqrt{5}-11)}{200}=\mathscr{T}_{\mathrm{SN}}\approx 0.0081. \tag{4.45}$$

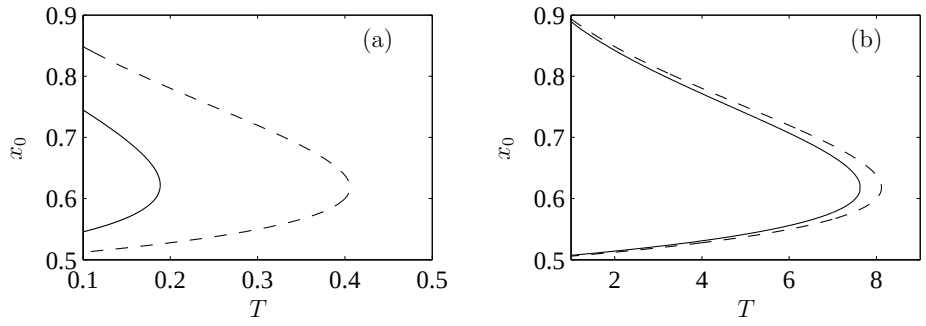

Figure 4.2: Position of collapsed point of highly-collapsed steady solutions of (1.26, 1.27) vs. T for $\mathscr{R} = 0.02$ (a) and 0.001 (b). Solid lines represent numerical results directly from (1.26, 1.27) while dashed lines represent asymptotic results from (4.43c).

In this case, we have

$$x_0 = \frac{\sqrt{5}-1}{2}, \tag{4.46}$$

$$H_{00} = \frac{40(3\sqrt{5}-7)}{3(11-5\sqrt{5})} \approx 21.5738. \tag{4.47}$$

The coalescence suggests a saddle-node bifurcation: two steady solutions (lower-branch and upper-branch) coexist when $\mathscr{T} < \mathscr{T}_{\rm SN}$, and no steady solution exists when $\mathscr{T} > \mathscr{T}_{\rm SN}$.

It is easily shown that h in (4.44b) represents two types of membrane shape: mode 1 (without upstream bulge) and mode 2 (with upstream bulge). We note that the mode 1 solution transforms to the mode 2 solution as x_0 increases through $2/3$ with $\mathscr{T} = 0.0075$, rather than through $(\sqrt{5}-1)/2$ with the saddle-node point $\mathscr{T} = \mathscr{T}_{\rm SN}$.

4.5 Linear stability of steady solutions

In the following, we study the linear stability of steady solutions (4.43) of the dynamical system (4.23), (4.26), (4.37) and (4.42). We add some small time-dependent

perturbation on the steady solution

$$Q_1 = 1 + \varepsilon Q_{11}(t) + \cdots, \tag{4.48a}$$
$$Q_0 = 1 + \varepsilon Q_{01}(t) + \cdots, \tag{4.48b}$$
$$x_0 = x_{00} + \varepsilon x_{01}(t) + \cdots, \tag{4.48c}$$
$$H_{00} = H_{000} + \varepsilon H_{001}(t) + \cdots, \tag{4.48d}$$

where ε is a small quantity. Upon substituting (4.48) into (4.23), (4.26), (4.37) and (4.42), we obtain two systems of equations at $O(1)$ and $O(\varepsilon)$. The system at $O(1)$ is (4.43) as expected and therefore $1/2 < x_{00} < 1$. The system at $O(\varepsilon)$ is

$$0 = 6\,(2Q_{01} + x_{01t}) - 12Q_{11} - \frac{\mathscr{L}(1-x_{00})^3 Q_{11tt}}{\mathscr{T}}, \tag{4.49a}$$
$$0 = 12\mathscr{T}(1-x_{00})^2 Q_{01} + 2\mathscr{T}(2-(2-x_{00})x_{00})x_{01t} + \mathscr{L}(1-x_{00})^3 x_{00}^2 Q_{11tt}, \tag{4.49b}$$
$$0 = 6(1-x_{00})^3(H_{001} - 2H_{000}Q_{01}) + 10H_{000}^2\mathscr{T}x_{01} + 5H_{000}^2\mathscr{L}(1-x_{00})^3 Q_{11t}, \tag{4.49c}$$
$$\begin{aligned} 0 = {} & 48\sqrt{30}\sqrt{\frac{\mathscr{T}}{H_{000}^3}}(1-x_{00})^3 x_{00}^3 H_{001} - H_{000}\left(32\sqrt{30}\sqrt{\frac{\mathscr{T}}{H_{000}^3}}(1-x_{00})^3 x_{00}^3 Q_{01}\right. \\ & - 12\mathscr{T}(1-x_{00})(2-x_{00}(5-4x_{00}))x_{01} - x_{00}(1-2x_{00})\Big(6\mathscr{L}(1-x_{00})^3 x_{00} Q_{11t} \\ & \left. + 2\mathscr{T}(2-(2-x_{00})x_{00})x_{01t} + \mathscr{L}(1-x_{00})^3 x_{00}^2 Q_{11tt}\Big)\right) \end{aligned} \tag{4.49d}$$

Using (4.43b, 4.43c), (4.49) is simplified to

$$\begin{aligned} & 9(-1+2x_{00})\left(-6(-1+x_{00})^2 Q_{11} + (1+2(-2+x_{00})x_{00})x_{01t}\right) \\ & + 50\mathscr{L}(-1+x_{00})x_{00}^2(1+2(-1+x_{00})x_{00})Q_{11tt} = 0, \end{aligned} \tag{4.50a}$$
$$\begin{aligned} & x_{00}\big(300\mathscr{L}(-1+x_{00})x_{00}^2(-3+2x_{00})Q_{11t} + 9(-1+2x_{00})(8+7(-2+x_{00})x_{00})x_{01t} \\ & + 50\mathscr{L}(-1+x_{00})x_{00}^2(2+(-4+x_{00})x_{00})Q_{11tt}\big) \\ & = 108\left((-1+x_{00})^2 x_{00}(-1+2x_{00})Q_{11} + \left(1-2x_{00}+x_{00}^3\right)x_{01}\right), \end{aligned} \tag{4.50b}$$

with

$$H_{001} = \frac{1}{81(1-2x_{00})^2(-1+x_{00})} 40x_{00}^2\big(54(-1+2x_{00})((-1+x_{00})Q_{11}+x_{01}) \\ -300\mathscr{L}(-1+x_{00})x_{00}^2Q_{11t} - 27(-1+x_{00})(-1+2x_{00})x_{01t} - 50\mathscr{L}(-1+x_{00})^2x_{00}^2Q_{11tt}\big), \tag{4.51a}$$

$$Q_{01} = Q_{11} - \frac{x_{01t}}{2} + \frac{25\mathscr{L}(-1+x_{00})x_{00}^2Q_{11tt}}{27-54x_{00}}. \tag{4.51b}$$

Finally, we have a third-order ordinary differential equation governing perturbation $Q_{11}(t)$

$$\begin{aligned} &108(-1+x_{00})^2(-1+2x_{00})\left(-1+x_{00}+x_{00}^2\right)Q_{11} \\ &-27x_{00}(1-2x_{00})^2(-1+x_{00})(2+(-2+x_{00})x_{00})Q_{11t} \\ &+50\mathscr{L}x_{00}^2(-2+x_{00}(5+4x_{00}(2-3x_{00}(3+(-3+x_{00})x_{00}))))Q_{11tt} \\ &+50\mathscr{L}x_{00}^3(-1+x_{00})^2(-1+x_{00}(3+4(-1+x_{00})x_{00}))Q_{11ttt} = 0. \end{aligned} \tag{4.52}$$

We write $Q_{11} = \mathrm{e}^{\sigma t}$, then the eigenvalue σ satisfies the cubic equation

$$\begin{aligned} &108(-1+x_{00})^2(-1+2x_{00})\left(-1+x_{00}+x_{00}^2\right) \\ &-27x_{00}(1-2x_{00})^2(-1+x_{00})(2+(-2+x_{00})x_{00})\sigma \\ &+50\mathscr{L}x_{00}^2(-2+x_{00}(5+4x_{00}(2-3x_{00}(3+(-3+x_{00})x_{00}))))\sigma^2 \\ &+50\mathscr{L}x_{00}^3(-1+x_{00})^2(-1+x_{00}(3+4(-1+x_{00})x_{00}))\sigma^3 = 0. \end{aligned} \tag{4.53}$$

Figure 4.3 shows eigenvalues from (4.53) as x_{00} increases from 0.55 to 0.8 for $\mathscr{L} = 0.1$, 0.06 and 0.03. At $x_{00} = 0.55$, there exist a positive real eigenvalue and a pair of complex conjugate eigenvalues with positive real part. At $x_{00} = 0.8$, there exist a negative and two positive real eigenvalues. For different $\mathscr{L}$ the progression of eigenvalues from $x_{00} = 0.55$ to 0.8 varies. We show three typical cases. When $\mathscr{L} = 0.1$, the positive real eigenvalue increases after decreases as x_{00} increases up to 0.8. As x_{00} increases from 0.55, the pair of complex conjugates eigenvalues split into two positive real eigenvalues before one of them decreases through zero at x_{SN} $(= (\sqrt{5}-1)/2)$. When $\mathscr{L} = 0.06$, first the pair of complex conjugate eigenvalues split into two positive real eigenvalue. The small one decreases through zero at x_{SN}. The large one coalesces with the positive real eigenvalue, then spit into a pair of complex conjugate eigenvalues before they become two positive real eigenvalues again. When $\mathscr{L} = 0.03$, the positive

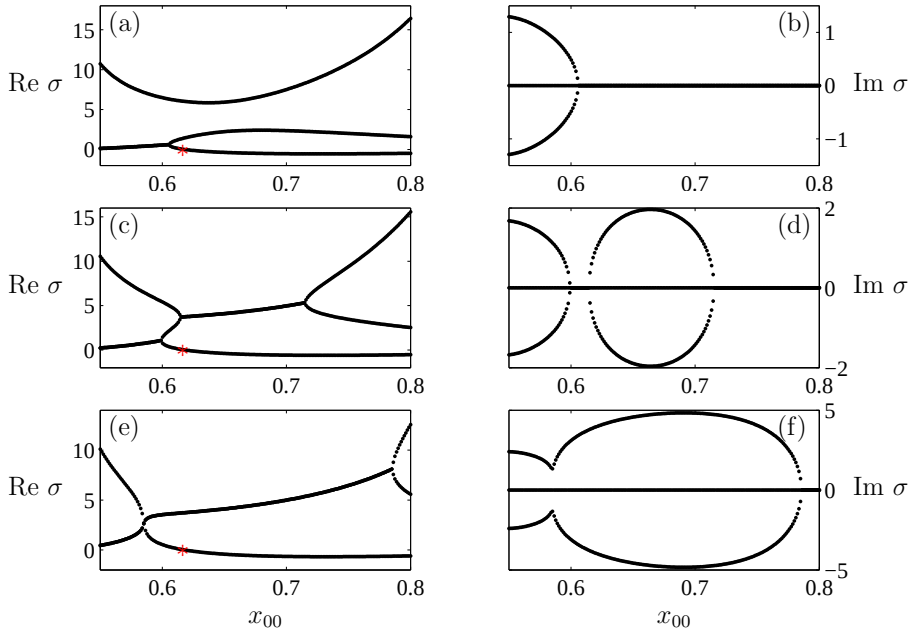

Figure 4.3: The real and imaginary parts of eigenvalues from (4.53) with $\mathscr{L} = 0.1$, 0.06 and 0.03 (from top to bottom). The stars in panel (a), (c) and (e) indicate turning points where $\sigma = 0$.

real eigenvalue decrease through zero at x_{SN}. The pair of complex conjugate eigenvalues have increasing real part before they split into two positive real eigenvalues. Therefore, we conclude that the sharp steady solution (4.44) is unstable.

In Figure 4.4 we can see that the eigenvalues computed from (4.53) successfully capture some low-frequency modes of instabilities directly calculated from (1.26, 1.27) for both steady states. However, our asymptotic analysis for small $\mathscr{R}$ presented here doesn't have capability to capture the Hopf bifurcation near the turning point in Figure 2.4(c), which is maybe because $\mathscr{R}$ used there isn't small enough.

In the limit of $\mathscr{L} \ll 1$ and $\mathscr{L} \gg 1$, we have asymptotic roots of (4.53): for $\mathscr{L} \ll 1$, then there are three roots given by $\sigma = -a/b$ and $\sigma^2 = -b/(\mathscr{L}d) + (a/b - c/d)/2$, where

$$a = 108(x_{00}-1)^2(2x_{00}-1)\left(x_{00}^2 + x_{00} - 1\right), \tag{4.54a}$$

$$b = -27(1-2x_{00})^2(x_{00}-1)x_{00}((x_{00}-2)x_{00}+2) \geq 0, \tag{4.54b}$$

$$c = 50x_{00}^2(x_{00}(4x_{00}(2-3x_{00}((x_{00}-3)x_{00}+3))+5)-2) < 0, \tag{4.54c}$$

$$d = 50(x_{00}-1)^2x_{00}^3(x_{00}(4(x_{00}-1)x_{00}+3)-1) \geq 0; \tag{4.54d}$$

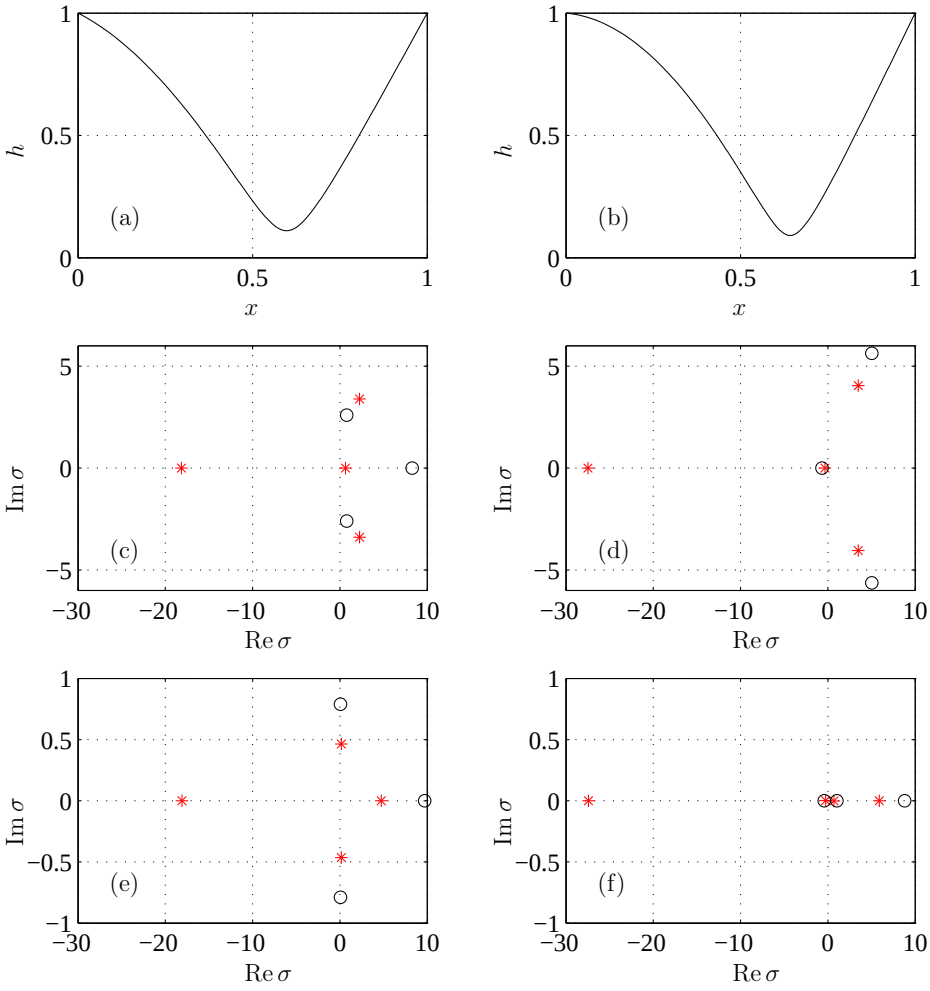

Figure 4.4: Highly collapsed steady solutions of (1.26, 1.27) and their eigenvalues of linear stability analysis (lower-branch in left panel and upper-branch in right panel). Here parameters are $\mathscr{R} = 0.005$, $T = 1.25$ and $L_2 = 5$ (second row) and 50 (third row), that is $\mathscr{T} = 0.00625$ and $\mathscr{L} = 0.025$ (second row) and 0.25 (third row). Stars represent eigenvalues directly computed from (1.26, 1.27) while circles represent three asymptotic eigenvalues from (4.53).

for $\mathscr{L} \gg 1$, the roots are given by $\sigma = -c/d$ and $\sigma^2 = -a/(\mathscr{L}c)$. Due to $a = 0$ at $x_{00} = (\sqrt{5}-1)/2$, we have $-a/b > (<)0$ and $-a/c < (>)0$ when $x_{00} < (>)(\sqrt{5}-1)/2$. Therefore, for $\mathscr{L} \ll 1$, there is one positive eigenvalue and a pair of conjugate complex eigenvalues for the lower-branch steady solution (Figure 4.4(c), $x_{00} < (\sqrt{5}-1)/2$) and there is one negative eigenvalue and a pair of conjugate complex eigenvalues for the upper-branch steady solution (Figure 4.4(d), $x_{00} > (\sqrt{5}-1)/2$); for $\mathscr{L} \gg 1$, there is one positive eigenvalue and a pair of conjugate complex eigenvalues for the lower-branch steady solution (Figure 4.4(e), $x_{00} < (\sqrt{5}-1)/2$) and there are three real eigenvalues (two positive and one negative) for the upper-branch steady solution (Figure 4.4(f), $x_{00} > (\sqrt{5}-1)/2$). Figure 4.4 gives a good validation of the prediction.

4.6 Conclusion

In this chapter we have investigated solutions of (1.26, 1.27) that are severely collapsed over a narrow region near the downstream end of the collapsible segment of the channel. We have split the flow into the three regions shown in Figure 4.1, using $\mathscr{R}$ as a small parameter in constructing matched asymptotic expansions for each region. We have assumed that the width of the collapsed region is $O(\mathscr{R})$ and the minimum channel width h at the most collapsed point is also $O(\mathscr{R})$.

We have found that the leading-order shape of the membrane in region I, from the upstream end to the narrow collapsed region, is parabolic (see (4.34)), and the leading-order shape of the membrane in region III, from the collapsed region to the downstream end, is linear (see (4.18)). Based on these leading-order solutions, we have constructed a system, comprising two mass conservation conditions (4.23, 4.37), one matching condition (4.26) and one energy budget (4.42), to describe the dynamics of the highly-collapsed membrane. By analysing the steady version of the leading-order solutions, we have found a saddle-node bifurcation at some $\mathscr{T} = \mathscr{T}_{\mathrm{SN}}$ for given small $\mathscr{R}$: no steady solutions exist when $\mathscr{T} > \mathscr{T}_{\mathrm{SN}}$; If $\mathscr{T} > \mathscr{T}_{\mathrm{SN}}$ two steady solutions coexist. The asymptotic prediction has been validated by the numerical solutions of (1.26, 1.27), as shown in Figure 4.2.

We also have examined the linear stabilities of the steady solutions and have found that they are unstable in the framework of the asymptotic analysis we used. Although we have not found slamming motion, identified in §2.4 and Stewart *et al.* (2010*a*), in the asymptotic framework, the unstable steady solutions are compatible with the arising

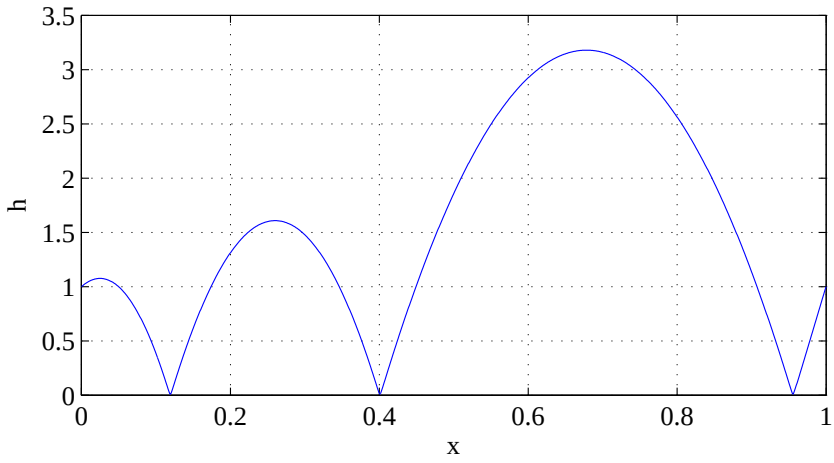

Figure 4.5: Steady solution of (1.26, 1.27) with three sharp constrictions for $\mathscr{R} = 0.001$ and $T = 0.3$.

of slamming motion. In the future work, we can explore the dynamic of the system of (4.23, 4.37, 4.26, 4.42) in detail to check whether it can give some signal of slamming motion.

Here we only consider the solution with one sharp constriction. But the system also has solutions with multiple sharp constrictions (steady solutions with multiple sharp constrictions can be determined by shooting method easily, see Figure 4.5). Our method used in this chapter maybe able to extend to the case of multiple sharp constrictions.

Chapter 5

Conclusion and future work

Overall, the focus of this thesis has been on instabilities of a collapsible-channel flow with the upstream flux fixed, which is a canonical problem in physiological fluid mechanics to understand the origin of self-excited oscillations in the Starling Resistor. Unlike the case of pressure-driven flow (e.g. Jensen & Heil, 2003), we stress the importance of prescribing a flow flux at the upstream end of the channel. That is because mode-2 oscillations in this system have been reported previously in numerical simulations (Luo & Pedley, 1996) but there has been relatively little progress in determining the mechanisms that might lead to the growth of instabilities. The work presented in this thesis has proposed two instability mechanisms (see Chapter 2 and Chapter 3) which are probably related to the self-excited oscillations observed in numerical simulations and experiments. For example, Bertram & Tscherry (2006) reported that increasing the length of the downstream tube reduced the frequency of oscillations but had little effect on the conditions for onset. This is mirrored in our model by oscillations arising along the upper end of the upper branch of the Hopf_2 curve (see (3.12), (3.13)), with frequency of magnitude $q_0^{**}/a\sqrt{L^{**}L_2^{**}}$ and onset Reynolds number (3.12) that is independent of L_2^{**}, suggesting a possible mechanistic connection with their observations.

Although our theoretical predictions have good agreement with some experimental results relating to self-excited oscillations, we can improve our model in future work by including some physical factors neglected in our present work. The first factor that should be added is wall inertia. As demonstrated in numerical simulations of Luo & Pedley (1998), wall inertia has a negligible effect on the self-excited oscillations in blood flow in arteries and veins, or experiments with water as the fluid; but for air flow

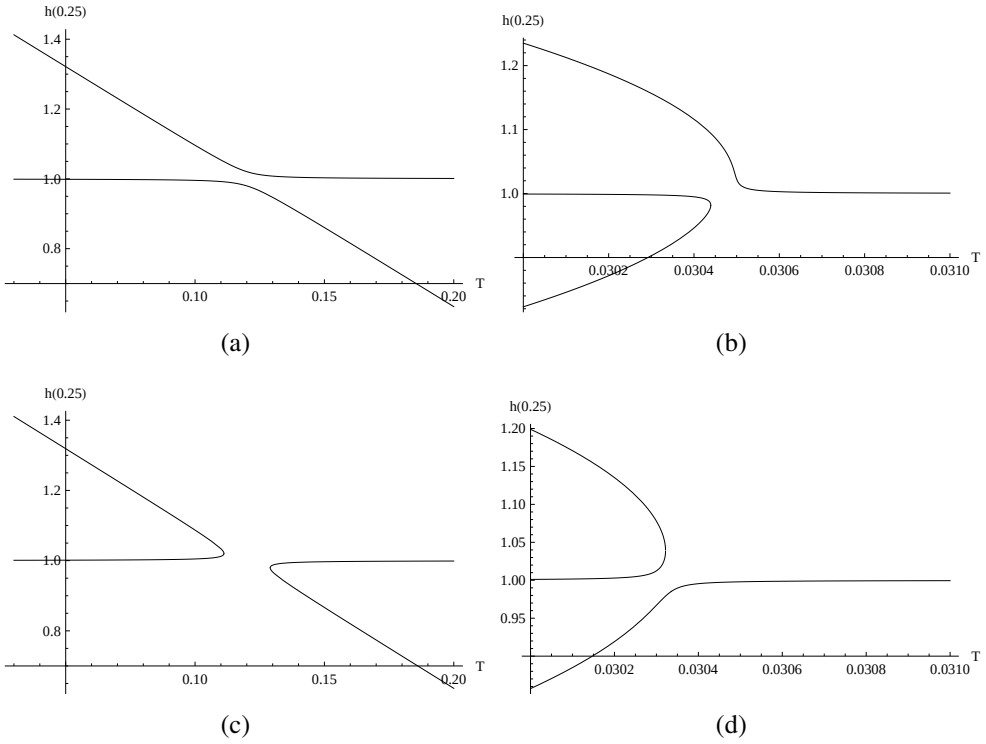

Figure 5.1: Bifurcation diagrams for (a) $b = -0.001$ and (c) $b = 0.001$ relating to TC_1 and (b) $b = -0.001$ and (d) $b = 0.001$ relating to TC_2.

in the lung, or experiments with air as fluid, wall inertia is found to play an important role in destabilizing the system.

In present work we adopt linear external pressure distribution (1.25) imposing on the membrane to guarantee the existence of the uniform steady state of (1.26, 1.27): $h = 1$ and $q = 1$. With a perturbed version of (1.25) as

$$p_{\text{ext}}(x) = 12\mathscr{R}(L_2 + 1 - x) + b, \tag{5.1}$$

we redo weakly nonlinear analysis in §2.3, assuming $b = O(\varepsilon^2)$, and find that the transcritical bifurcations TC_1 and TC_2 shown in Figure 2.4(b) are destroyed (Figure 5.1(a)) or replace by one (Figure 5.1(b), (d)) or two saddle-node bifurcations (Figure 5.1(c)). The effect of other variations of external pressure can be examined in future work.

Although in the present work our focus is on the instabilities of collapsible-channel flow, we also have observed sustaining large-amplitude 'slamming' oscillations repeatedly, which are initially predicted by Stewart *et al.* (2009) in one-dimensional

pressure-driven model then and subsequently confirmed in two-dimensional Navier–Stokes-based simulations. This near-singular behaviour is of particular interest because of its central role in the dynamics of the system, and its potential relevance to the motion of vocal folds, which can repeatedly come into contact during phonation (Thomson *et al.*, 2007). During slamming oscillations the collapsible segment experiences short periods of almost fully constriction near its downstream end. For some parameter settings (such as in the nearly inviscid limit) the constriction can be very sharp, which places great demands on any computational scheme and challenges the assumptions of any long-wave length model. In particular, when the flow is evolving very rapidly, the assumption that the velocity profile is proportional to the local volume flux, as in (1.16), is likely to be insufficient; one possible improvement would be to include additional dependence on the local pressure gradient, as proposed by Bessems *et al.* (2007).

Our one-dimensional model (1.26, 1.27) is independent of the length of the upstream rigid segment L_1, and so are the instability mechanisms we propose. However, the corresponding two-dimensional model given in §1.4 needs L_1 as input. If the upstream rigid segment is longer than the downstream one ($L_1 > L_2$) in the pressure-driven model the sloshing won't take place (Jensen & Heil, 2003). Thus a question arises: will the results we predict still be seen in the case when upstream pressure is fixed but L_1 is large? In the framework of linear stability analysis of one-dimensional model, we can say yes by comparing boundary condition (3.6c) in Stewart *et al.* (2009) with the second part of (2.2a). Further work needs to be done to check whether in general prescribing the upstream flow rate is equivalent to a very large upstream length in a flexible-tube system.

References

AITTOKALLIO, T., GYLLENBERG, M. & POLO, O. 2001 A model of a snorer's upper airway. *Math. Biosci.* **170** (1), 79–90.

AITTOKALLIO, T., VIRKKI, A. & POLO, O. 2009 Understanding sleep-disordered breathing through mathematical modelling. *Sleep Med. Rev.* **13** (5), 333–343.

ALIPOUR, F., BERRY, D. A. & TITZE, I. R. 2000 A finite-element model of vocal-fold vibration. *J. Acoust. Soc. Am.* **108** (6), 3003–3012.

ALIPOUR, F., BRUCKER, C., COOK, D. D., GOMMEL, A., KALTENBACHER, M., MATTHEUS, W., MONGEAU, L., NAUMAN, E., SCHWARZE, R., TOKUDA, I. & ZORNER, S. 2011 Mathematical models and numerical schemes for the simulation of human phonation. *Curr. Bioinformatics* **6** (3), 323–343.

ANDERSON, P, FELS, S & GREEN, S 2013 Implementation and validation of a 1d fluid model for collapsible channels. *ASME J. Biomech. Engng.* **135** (11), 111006.

BERTRAM, C. D. 1986 Unstable equilibrium behaviour in collapsible tubes. *J. Biomech.* **19** (1), 61–69.

BERTRAM, C. D. 2003 Experimental studies of collapsible tubes. In *Flow Past Highly Compliant Boundaries and in Collapsible Tubes* (ed. P. W. Carpenter & T. J. Pedley), pp. 51–65. Kluwer.

BERTRAM, C. D. 2004 Flow phenomena in floppy tubes. *Contemp. Phys.* **45** (1), 45–60.

BERTRAM, C. D. 2008 Flow-induced oscillation of collapsed tubes and airway structures. *Respir. Physiol. Neurobiol.* **163** (1-3), 256–265.

BERTRAM, C. D. & PEDLEY, T. J. 1982 A mathematical model of unsteady collapsible tube behaviour. *J. Biomech.* **15** (1), 39–50.

BERTRAM, C. D., RAYMOND, C. J. & BUTCHER, K. S. A. 1989 Oscillations in a collapsed-tube analog of the brachial artery under a sphygmomanometer cuff. *ASME J. Biomech. Engng.* **111** (3), 185–191.

BERTRAM, C. D., TRUONG, N. K. & HALL, S. D. 2008 PIV measurements of the flow field just downstream of an oscillating collapsible tube. *ASME J. Biomech. Engng.* **130** (6), 061011.

BERTRAM, C. D. & TSCHERRY, J. 2006 The onset of flow-rate limitation and flow-induced oscillations in collapsible tubes. *J. Fluids Struct.* **22** (8), 1029–1045.

BESSEMS, D., RUTTEN, M. & VAN DE VOSSE, F. 2007 A wave propagation model of blood flow in large vessels using an approximate velocity profile function. *J. Fluid Mech.* **580** (1), 145–168.

CAI, Z. X. & LUO, X. Y. 2003 A fluid-beam model for flow in a collapsible channel. *J. Fluids Struct.* **17** (1), 125–146.

CANCELLI, C. & PEDLEY, T. J. 1985 A separated-flow model for collapsible-tube oscillations. *J. Fluid Mech.* **157**, 375–404.

CARPENTER, P. W. & GARRAD, A. D. 1985 The hydrodynamic stability of flow over Kramer-type compliant surfaces. Part 1. Tollmien-Schlichting instabilities. *J. Fluid Mech.* **155**, 465–510.

CARPENTER, P. W. & GARRAD, A. D. 1986 The hydrodynamic stability of flow over Kramer-type compliant surfaces. Part 2. Flow-induced surface instabilities. *J. Fluid Mech.* **170**, 199–232.

CONRAD, W. A. 1969 Pressure-flow relationships in collapsible tubes. *IEEE Biomed. Engng,.* **16** (4), 284–295.

DOARÉ, O. & DE LANGRE, E. 2006 The role of boundary conditions in the instability of one-dimensional systems. *Eur. J. Mech. B Fluids* **25** (6), 948–959.

DOHERTY, M. J., SPENCE, D. P. S., GRAHAM, D., CHEETHAM, B. M. G., SUN, X. Q. & EARIS, J. E. 1998 A vibrating trachea. *Thorax* **53** (3), 230–231.

ELLIOTT, E. A. & DAWSON, S. V. 1977 Test of wave-speed theory of flow limitation in elastic tubes. *J. Appl. Physiol.* **43** (3), 516–522.

FODIL, R., RIBREAU, C., LOUIS, B., LOFASO, F. & ISABEY, D. 1997 Interaction between steady flow and individualised compliant segments: Application to upper airways. *Med. Bio. Eng. Comput.* **35** (6), 638–648.

FORGACS, P. 1967 Crackles and wheezes. *The Lancet* **290**, 203–205.

FORGACS, P., NATHOO, A. R. & RICHARDSON, H. D. 1971 Breath sounds. *Thorax* **26** (3), 288–295.

GAVRIELY, N. 1996 Analysis of breath sounds in bronchial provocation tests. *Am. J. Respir. Crit. Care Med.* **153** (5), 1469–1471.

GAVRIELY, N. & CUGELL, D. W. 1995 *Breath sounds methodology*. CRC Press.

GAVRIELY, N. & JENSEN, O. E. 1993 Theory and measurements of snores. *J. Appl. Physiol.* **74** (6), 2828–2837.

GAVRIELY, N., SHEE, T. R., CUGELL, D. W. & GROTBERG, J. B. 1989 Flutter in flow-limited collapsible tubes: a mechanism for generation of wheezes. *J. Appl. Physiol.* **66** (5), 2251–2261.

GROTBERG, J. B. 1994 Pulmonary flow and transport phenomena. *Annu. Rev. Fluid Mech.* **26**, 529–571.

GROTBERG, J. B. 2001 Respiratory fluid mechanics and transport processes. *Annu. Rev. Biomed. Eng.* **3**, 421–457.

GROTBERG, J. B. 2011 Respiratory fluid mechanics. *Phys. Fluids* **23**, 021301.

GROTBERG, J. B. & GAVRIELY, N. 1989 Flutter in collapsible tubes: a theoretical model of wheezes. *J. Appl. Physiol.* **66** (5), 2262–2273.

GROTBERG, J. B. & JENSEN, O. E. 2004 Biofluid mechanics in flexible tubes. *Annu. Rev. Fluid Mech.* **36**, 121–147.

GUCKENHEIMER, J. & HOLMES, P. 1983 *Nonlinear oscillations, dynamical systems, and bifurcations of vector fields*, *Applied Mathematical Sciences*, vol. 42. Springer.

GUNERATNE, J. C. & PEDLEY, T. J. 2006 High-reynolds-number steady flow in a collapsible channel. *J. Fluid Mech.* **569**, 151–184.

HAZEL, ANDREW L. & HEIL, MATTHIAS 2003 Steady finite-reynolds-number flows in three-dimensional collapsible tubes. *J. Fluid Mech.* **486**, 79–103.

HEIL, MATTHIAS 1995 Large deformations of cylindrical shells conveying viscous flow. PhD thesis, University of Leeds, Leeds.

HEIL, MATTHIAS 1997 Stokes flow in collapsible tubes: computation and experiment. *J. Fluid Mech.* **353**, 285–312.

HEIL, M. 1998 Stokes flow in an elastic tube — a large-displacement fluid-structure interaction problem. *Int. J. Numer. Meth. Fluids* **28** (2), 243–265.

HEIL, M. & BOYLE, J. 2010 Self-excited oscillations in three-dimensional collapsible tubes: simulating their onset and large-amplitude oscillations. *J. Fluid Mech.* **652**, 405–426.

HEIL, M. & HAZEL, A. L. 2006 `oomph-lib` An Object-Oriented Multi-Physics Finite-Element Library. In *Fluid-Structure Interaction* (ed. M. Schäfer & H.-J. Bungartz), pp. 19–49. Springer, `oomph-lib` is available as open-source software at `http://www.oomph-lib.org`.

HEIL, M. & HAZEL, A. L. 2011 Fluid-structure interaction in internal physiological flows. *Annu. Rev. Fluid Mech.* **43**, 141–162.

HEIL, M. & JENSEN, O. E. 2003 Flows in deformable tubes and channels - theoretical models and biological applications. In *Flow Past Highly Compliant Boundaries and in Collapsible Tubes* (ed. P. W. Carpenter & T. J. Pedley), pp. 15–49. Kluwer.

HEIL, M. & WATERS, S. L. 2006 Transverse flows in rapidly oscillating elastic cylindrical shells. *J. Fluid Mech.* **547**, 185–214.

HEIL, M. & WATERS, S. L. 2008 How rapidly oscillating collapsible tubes extract energy from a viscous mean flow. *J. Fluid Mech.* **601**, 199–227.

HOLMES, P. J. 1980 Averaging and chaotic motions in forced oscillations. *SIAM J. Appl. Math.* **38** (1), 65–80.

HUANG, L. X. 1995 Mechanical modeling of palatal snoring. *J. Acoust. Soc. Am.* **97** (6), 3642–3648.

HUANG, L. X. & FFOWCS WILLIAMS, J. E. 1999 Neuromechanical interaction in human snoring and upper airway obstruction. *J. Appl. Physiol.* **86** (6), 1759–1763.

HUANG, L. X., QUINN, S. J., ELLIS, P. D. M. & FFOWCS WILLIAMS, J. E. 1995 Biomechanics of snoring. *Endeavour* **19** (3), 96–100.

HUNTER, E. J., TITZE, I. R. & ALIPOUR, F. 2004 A three-dimensional model of vocal fold abduction/adduction. *J. Acoust. Soc. Am.* **115** (4), 1747–1759.

ISHIZAKA, K. & FLANAGAN, J. L. 1972 Synthesis of voiced sounds from a two-mass model of the vocal cords. *Bell Syst. Tech. J.* **51** (6), 1233–1268.

JENSEN, O E 1990 Instabilities of flow in a collapsed tube. *J. Fluid Mech.* **220**, 623–659.

JENSEN, O. E. 1992 Chaotic oscillations in a simple collapsible-tube model. *ASME J. Biomech. Engng.* **114** (1), 55–59.

JENSEN, O. E. 1998 An asymptotic model of viscous flow limitation in a highly collapsed channel. *ASME J. Biomech. Engng.* **120** (4), 544–546.

JENSEN, O. E. & HEIL, M. 2003 High-frequency self-excited oscillations in a collapsible-channel flow. *J. Fluid Mech.* **481**, 235–268.

KAMM, R. D. & PEDLEY, T. J. 1989 Flow in collapsible tubes: A brief review. *ASME J. Biomech. Engng.* **111** (3), 177–179.

KAMM, ROGER D. & SHAPIRO, ASCHER H. 1979 Unsteady flow in a collapsible tube subjected to external pressure or body forces. *J. Fluid Mech.* **95**, 1–78.

KNIESBURGES, S., THOMSON, S. L., BARNEY, A., TRIEP, M., SIDLOF, P., HORACEK, J., BRUCKER, C. & BECKER, S. 2011 In vitro experimental investigation of voice production. *Curr. Bioinformatics* **6** (3), 305–322.

KU, D. N. 1997 Blood flow in arteries. *Annu. Rev. Fluid Mech.* **29**, 399–434.

KUDENATTI, R. B., BUJURKE, N. M. & PEDLEY, T. J. 2012 Stability of two-dimensional collapsible-channel flow at high reynolds number. *J. Fluid Mech.* **705**, 371–386.

KUMARAN, V. 1995 Stability of the viscous flow of a fluid through a flexible tube. *J. Fluid Mech.* **294**, 259–281.

KUMARAN, V. 1998 Stability of wall modes in a flexible tube. *J. Fluid Mech.* **362**, 1–15.

KUMARAN, V. 2003 Hydrodynamic stability of flow through compliant channels and tubes. In *Flow Past Highly Compliant Boundaries and in Collapsible Tubes*.

LEUPPI, J. D., DIETERLE, T., WILDEISEN, I., MARTINA, B., TAMM, M., KOCH, G., PERRUCHOUD, A. P. & LEIMENSTOLL, B. M. 2006 Can airway obstruction be estimated by lung auscultation in an emergency room setting? *Respir. Med.* **100** (2), 279–285.

LIU, H. F., LUO, X. Y. & CAI, Z. X. 2012 Stability and energy budget of pressure-driven collapsible channel flows. *J. Fluid Mech.* **705**, 348–370.

LIU, H. F., LUO, X. Y., CAI, Z. X. & PEDLEY, T. J. 2009 Sensitivity of unsteady collapsible channel flows to modelling assumptions. *Commun. Numer. Meth. Engng.* **25** (5), 483–504.

LIU, Z. S., LUO, X. Y., LEE, H. P. & LU, C. 2007 Snoring source identification and snoring noise prediction. *J. Biomech.* **40** (4), 861–870.

LUO, X. Y., CAI, Z. X., LI, W. G. & PEDLEY, T. J. 2008 The cascade structure of linear instability in collapsible channel flows. *J. Fluid Mech.* **600**, 45–76.

LUO, X. Y. & PEDLEY, T. J. 1995 A numerical simulation of steady flow in a 2-d collapsible channel. *J. Fluids Struct.* **9** (2), 149 – 174.

LUO, X. Y. & PEDLEY, T. J. 1996 A numerical simulation of unsteady flow in a two-dimensional collapsible channel. *J. Fluid Mech.* **314**, 191–225.

LUO, X. Y. & PEDLEY, T. J. 1998 The effects of wall inertia on flow in a two-dimensional collapsible channel. *J. Fluid Mech.* **363**, 253–280.

LUO, X. Y. & PEDLEY, T. J. 2000 Multiple solutions and flow limitation in collapsible channel flows. *J. Fluid Mech.* **420**, 301–324.

MANDRE, S. & MAHADEVAN, L. 2010 A generalized theory of viscous and inviscid flutter. *Proc. R. Soc. A* **466**, 141–156.

MANUILOVICH, S. V. 2004 Propagation of a tollmien-schlichting wave over the junction between rigid and compliant surfaces. *Fluid Dyn.* **39** (5), 702–717.

MATSUZAKI, Y. & MATSUMOTO, T. 1989 Flow in a two-dimensional collapsible channel with rigid inlet and outlet. *ASME J. Biomech. Engng.* **111** (3), 180–184.

MCCLURKEN, M. E., KECECIOGLU, I., KAMM, R. D. & SHAPIRO, A. H. 1981 Steady, supercritical flow in collapsible tubes. Part 2. Theoretical studies. *J. Fluid Mech.* **109**, 391–415.

MESLIER, N., CHARBONNEAU, G. & RACINEUX, J. L. 1995 Wheezes. *Eur. Respir. J.* **8** (11), 1942–1948.

DE OLIVEIRA ROSA, M., PEREIRA, J. C., GRELLET, M. & ALWAN, A. 2003 A contribution to simulating a three-dimensional larynx model using the finite element method. *J. Acoust. Soc. Am.* **114** (5), 2893–2905.

PASTERKAMP, H., KRAMAN, S. S. & WODICKA, G. R. 1997 Respiratory sounds: Advances beyond the stethoscope. *Am. J. Respir. Crit. Care Med.* **156** (3), 974–987.

PEDLEY, T.J. & LUO, X.Y. 1998 Modelling flow and oscillations in collapsible tubes. *Theor. Comput. Fluid Dyn.* **10**, 277–294.

PEDLEY, T. J. 1977 Pulmonary fluid dynamics. *Annu. Rev. Fluid Mech.* **9**, 229–274.

PEDLEY, T. J. 1980 *The fluid mechanics of large blood vessels*. Cambridge University Press.

PEDLEY, T. J. 1992 Longitudinal tension variation in collapsible channels - a new mechanism for the breakdown of steady flow. *ASME J. Biomech. Engng.* **114** (1), 60–67.

PELORSON, X., HIRSCHBERG, A., VAN HASSEL, R. R., WIJNANDS, A. P. J. & AUREGAN, Y. 1994 Theoretical and experimental study of quasisteady-flow separation within the glottis during phonation. application to a modified two-mass model. *J. Acoust. Soc. Am.* **96**, 3416–3431.

PIHLER-PUZOVIĆ, D. & PEDLEY, T. J. 2013 Stability of high-reynolds-number flow in a collapsible channel. *J. Fluid Mech.* **714**, 536–561.

RAST, M. P. 1994 Simultaneous solution of the navier-stokes and elastic membrane equations by finite-element method. *Int. J. Numer. Meth. Fluids* **19** (12), 1115–1135.

ROGELIO PEREZ-PADILLA, J., SLAWINSKI, E., DIFRANCESCO, L. M., FEIGE, R. R., REMMERS, J. E. & WHITELAW, W. A. 1993 Characteristics of the snoring noise in patients with and without occlusive sleep apnea. *Am. Rev. Respir. Dis.* **147** (3), 635–644.

SERA, T., SATOH, S., HORINOUCHI, H., KOBAYASHI, K. & TANISHITA, K. 2003 Respiratory flow in a realistic tracheostenosis model. *ASME J. Biomech. Engng.* **125** (4), 461–471.

SHAPIRO, A. H. 1977 Steady flow in collapsible tubes. *ASME J. Biomech. Engng.* **99** (3), 126–147.

STEWART, P. S., HEIL, M., WATERS, S. L. & JENSEN, O. E. 2010*a* Sloshing and slamming oscillations in a collapsible channel flow. *J. Fluid Mech.* **662**, 288–319.

STEWART, P. S., WATERS, S. L. & JENSEN, O. E. 2009 Local and global instabilities of flow in a flexible-walled channel. *Eur. J. Mech. B Fluids* **28** (4), 541–557.

STEWART, P. S., WATERS, S. L. & JENSEN, O. E. 2010*b* Local instabilities of flow in a flexible channel: Asymmetric flutter driven by a weak critical layer. *Phys. Fluids* **22**, 031902, cited By (since 1996) 2.

STORY, B. H. & TITZE, I. R. 1995 Voice simulation with a body-cover model of the vocal folds. *J. Acoust. Soc. Am.* **97** (2), 1249–1260.

THOMSON, S. L., MONGEAU, L. & FRANKEL, S. H. 2005 Aerodynamic transfer of energy to the vocal folds. *J. Acoust. Soc. Am.* **118** (3), 1689–1700.

THOMSON, S. L., MONGEAU, L. & FRANKEL, S. H. 2007 Flow over a membrane-covered, fluid-filled cavity. *Comput. Struct.* **85**, 1012–1019.

TITZE, I. R. 1973 The human vocal cords: A mathematical model. Part I. *Phonetica* **28**, 129–170.

TITZE, I. R. 1974 The human vocal cords: A mathematical model. Part II. *Phonetica* **29**, 1–21.

WHITTAKER, R. J., HEIL, M., BOYLE, J., JENSEN, O. E. & WATERS, S. L. 2010*a* The energetics of flow through a rapidly oscillating tube. Part 2. Application to an elliptical tube. *J. Fluid Mech.* **648**, 123–153.

WHITTAKER, R. J., HEIL, M., JENSEN, O. E. & WATERS, S. L. 2010*b* Predicting the onset of high-frequency self-excited oscillations in elastic-walled tubes. *Proc. R. Soc. A* **466**, 3635–3657.

WHITTAKER, R. J., HEIL, M., JENSEN, O. E. & WATERS, S. L. 2010*c* A rational derivation of a tube law from shell theory. *Q. J. Mech. Appl. Math.* **63** (4), 465–496.

WHITTAKER, R. J., HEIL, M. & WATERS, S. L. 2011 The energetics of flow through a rapidly oscillating tube with slowly varying amplitude. *Phil. Trans. R. Soc. A* **369**, 2989–3006.

WHITTAKER, R. J., WATERS, S. L., JENSEN, O. E., BOYLE, J. & HEIL, M. 2010*d* The energetics of flow through a rapidly oscillating tube. Part 1. General theory. *J. Fluid Mech.* **648**, 83–121.

WILSON, K., STOOHS, R. A., MULROONEY, T. F., JOHNSON, L. J., GUILLEMINAULT, C. & HUANG, Z. 1999 The snoring spectrum: acoustic assessment of snoring sound intensity in 1139 individuals undergoing polysomnography. *Chest* **115** (3), 762–770.

XU, F., BILLINGHAM, J. & JENSEN, O. E. 2013 Divergence-driven oscillations in a flexible-channel flow with fixed upstream flux. *J. Fluid Mech.* **723**, 706–733.

XU, F., BILLINGHAM, J. & JENSEN, O. E. 2014 Resonance-driven oscillations in a flexible-channel flow with fixed upstream flux and a long downstream rigid segment. *J . Fluid Mech.* **746**, 368–404.